High-order Accurate Methods for solving Maxwell's equations and their applications

by

Sehun Chun

B. S., Seoul National University, 1999

M. S., Purdue University, 2003

M. S., Brown University, 2006

A dissertation submitted in partial fulfillment of the requirements for the Degree of Doctor of Philosophy in the Division of Applied Mathematics at Brown University

Providence, Rhode Island

May 2008

Abstract

This thesis contains two topics on high-order accurate methods for solving Maxwell's equations. The first topic is the application of high-order accurate methods to the modeling/ designs of photonic crystals. The second topic is the development of thin layer approximations and implementation in discontinuous Galerkin method. Each topic consists of two parts as described below.

The first part, part I of the first topic, demonstrates the behavior and sensitivity of the frozen mode phenomenon in finite structures with anisotropic materials, including both magnetic materials and non-normal incidence. A discontinuous Galerkin method is used for solving Maxwell's equations in the time domain. The existence of the frozen mode phenomena is confirmed and the impact of finiteness and perturbations of periodicity is studied.

In the second part, part II of the second topic, PDE constrained nonlinear optimization techniques are implemented to optimized the design of electromagnetic crystals for the frozen mode phenomenon. We investigate both of gyrotropic photonic crystals and degenerate band edge crystals as well as the more complex case of the oblique incidence. We extend the investigation to the three-dimensional case to identify the first three-dimensional crystal exhibiting frozen mode behavior.

The third part, part I of the second topic, studies high-order accurate thin layer approximations for metal backed coatings in the time-

domain. Isotropic materials and tangentially-oriented anisotropic materials are considered in one and two dimensions. The implementation of these models are discussed in the context of discontinuous Galerkin methods which are particularly well-suited for these approximations. The range of validity, accuracy, and stability of the resulting schemes is discussed through one- and two- dimensional examples.

The last part, part II of the second topic, also studies high-order accurate thin layer approximations, but for transmission layers. The thin layer formulation of 3rd order and 5th order for curvilinear transmission layers are derived. Also, similar to the previous part, computational results on the range of validity, accuracy, and stability is demonstrated on one- and two- dimensional cases.

This thesis is based on the following 4 papers

- S. Chun and J. S. Hesthaven, *Modeling of the frozen mode phenomenon and its Sensitivity using Discontinuous Galerkin methods*, commun. comput. phys., 2, 2007, pp. 611-639

- S. Chun and J. S. Hesthaven, *PDE constrained optimization and design of frozen mode crystals*, commun. comput. phys., 3, 2008, pp. 878-898

- S. Chun and J. S. Hesthaven, *High-order accurate thin layer approximation for time-domain electromagnetics, Part I: General metal backed coatings*, in preparation

- S. Chun, H. Haddar and J. S. Hesthaven, *High-order accurate thin layer approximation for time-domain electromagnetics, Part II: Interface conditions*, in preparation

Curriculum vitae

• **Education**

Applied Mathematics, Brown University, RI
Candidate for Ph.D., May 2008
Travel award for 2007 summer for joint works with INRIA, Rocquencourt, France
Travel award for 2006 on CEA-EDF-INRIA School on the wave equations

Applied Mathematics, Brown University, RI
Master of Science, May 2006

Mathematics, Purdue University, IN
Master of Science, May 2003
Vice President of Purdue Korean Graduate student association, 2002-2003

Mechanical and Aerospace Engineering, Seoul National Univ., Korea
Bachelor of Science, February 1999
Honor scholarship, 1993-1996

• **Publications**

1) S. Chun and J.S. Hesthaven. *Modeling of the frozen mode phenomenon and its sensitivity using Discontinuous Galerkin Methods*, commun. comput. phys., 2(2007). pp. 611-639

2) S. Chun and J.S. Hesthaven. *PDE constrained optimization and Design of Frozen mode crystals*, commun. comput. phys., 3(2008). pp. 878-898

3) S. Chun and J.S. Hesthaven. *High-order accurate thin layer approximation for time-domain electromagnetics, Part I: General metal backed coatings*, in preparation

4) S. Chun, H. Haddar and J.S. Hesthaven. *High-order accurate thin layer approximation for time-domain electromagnetics, Part II: Interface conditions*, in preparation

• **Teaching experience**

Teaching Assistant

- Introduction to Numerical Solutions of PDEs, Brown University, 2007
- Introduction to Differential Geometry, Brown University, 2004
- Linear Algebra, Purdue University, 2001-2003

• **Research experience**

Research Assistant, Brown University, 2004 - present

- Modeling and design of photonic crystal structure to slow-down/freeze the light.
- Nonlinear optimization on Maxwell eigenvalue problem to obtain various singularities in dispersion relation.
- Stochastic sensitivity analysis of the physical parameters on the newly discovered nonlinear featured phenomena.
- Implementation of thin layer approximation to reduce the computational costs for thin magnetic layers.

• **Research skills**

- Research area: Computational electrodynamics, Maxwells equations, Discontinuous Galerkin method, Finite difference method, Computational Stochastic differential equations, Linear/Nonlinear Optimization
- Language: C++ , FORTRAN, MATLAB, SCHEME, LISP

• **Volunteers and other activities**

- The Math Recourse Center (MRC) staff, Department of Mathematics, Brown University, 2004
- Church Van service, Providence Central Church and The First Korean church in Cambridge, 2004 - present

This dissertation by Sehun Chun is accepted in its present form by the Division of Applied Mathematics as satisfying the dissertation requirement for the degree of Doctor of Philosophy.

Date ______________ ____________________________________
Jan S. Hesthaven, Director

Recommended to the Graduate Council

Date ______________ ____________________________________
David Gottlieb, Reader

Date ______________ ____________________________________
Chi-Wang Shu, Reader

Approved by the Graduate Council

Date __________ ____________________________________
Sheila Bonde
Dean of the Graduate School

Acknowledgements

Firstly, I'd like to thank my advisor, Prof. Jan S. Hesthaven, for sticking it out with me all these years and giving of his inspiration and time. I could not have imagined having a better advisor and mentor for my Ph.D.

My thanks also go to Prof. David Gottlieb whose insight and passion he has shown in class got me back into this field of study when I was fogged in. And I thank Prof. Chi-Wang Shu for the advice and perceptiveness to enhance my understanding on discontinuous Galerkin method in my research. Also, I'd like to thank Dr. Houssem Haddar for giving his time, insights and enthusiasm during my stay in Paris. I would be totally left out alone and would feel desperate in the middle of Europe without his help.

Also, I would like to express my appreciation to the supporting staff in the Division of Applied Mathematics of Brown University for providing a friendly environment.

Special thanks to my colleagues in Brown University, especially Akil Narayan, Alan R. Schiemenz, and Andreas Kloeckner, who brightened my graduate school experience with their humor and friendship. Thanks to my family and Won for standing with me through a lot more than they'd bargained for. And thanks to God, who is "my shepherd; I shall not want"

Contents

List of Figures

List of Tables

Chapter 1

Introduction

Maxwell's equations appeared in 1861 paper by James Clerk Maxwell's equations on *Physical Lines of Force*. This set of four equations describes the relations between electric field, magnetic field, electric charge, and electric current to model how an electromagnetic field varies in space and time. Not mentioning their crucial roles in everything from quantum mechanics to relativity theory, they enable us to understand better nature and the link between electricity, magnetism, geometry and time, which is God's blueprint for nature. However, there are some obstacles. Although Maxwell's equations are relatively simple, the solutions even in simple circumstances are not easy to obtain. The phenomena appearing in fundamental circumstances are often solved by inspired physicists and mathematicians including Maxwell himself, but the solution in realistic and complicated circumstances, which can bring innovative steps on human technologies, still remains unsolved.

Photonic crystal, the subject of the first two part of this thesis, is an example of such solutions in complicated circumstances. Photonic crystal has emerged in an attempt to control the flow of light in materials. As optical analogue to the crystal, a periodic arrangement of atoms, it consists of periodic array of media with different dielectric constants. We design and construct photonic crystals to propagate the light anomalously, i.e., to prevent monochromatic waves from propagating in certain directions, to confine them in a certain space, and to significantly decrease the speed of waves or even completely stop them in periodic lattices, which will bring an enormous range of technological developments when these photonic crystals are realized. As is common in recent research of science and engineering, we rely on the numerical solution of Maxwell's equations for photonic crystal and considerable efforts on developing efficient computational methods have been made. The frequency-domain solution from Maxwell eigenproblems has been popular for designing photonic crystals, while the difficulty with nonlinear or time-varying media and the perplexity of studying photonic crystals with partial periodicity lead to a wider attention on the time domain solution. As one effort to improve the time domain solutions, discontinuous Galerkin method for time-domain simulation of photonic crystal is introduced in this thesis as an fast and robust alternative to finite difference method, which has some computational drawbacks, such as less accuracy and less geometrical flexibility. Along with this time domain simulation, new sets of parameters of photonic crystals are obtained by combining this with a nonlinear optimization technique.

Thin layer approximation, or also known as approximate boundary conditions are boundary conditions which model a thin layer which is not resolved in real mesh grid. It was first used for ground wave propagation over the Earth during World War II although it has been know for more than 80 years. In 1940, S.M. Rytov [26] at Institute of Physics at Russia, who sought an improvement of classical boundary condition of perfectly electric conductor (PEC), showed that the tangential components of the electric field can be expressed as the tangential components of the magnetic field using the power series in terms of the thickness of a thin layer. Since then, it has been widely used and further developments are now studied. For example, Absorbing boundary condition (ABC) to eliminate the unnecessary reflected waves is a special type of these approximation. Then, naturally one can say, "what is the objective of thin layer approximation?". In general, we know the exterior field of an object considering the interior field of it. However, we can compute the exterior field using a thin layer approximation at the boundary values of exterior field only. In other words, the problem with two different medium can be converted into a problem with a single medium with a complex boundary conditions. Another important reason comes from the efforts of eliminating geometrical constraints of the thin layer mesh. Computation without small grids inside the thin layer significantly reduces the size of the discrete model and consequently reduces the time of computations, especially when the layer is thin compared to the wavelength of the incident wave. In the latter part of this thesis, high-order thin layer approximations are derived and studied in the context of discontinuous Galerkin method, which is well-suited for the implementation of these approximation.

This dissertation is organized as follows. Maxwell's equations in the time domain are briefly described in chapter 2. In chapter 3, the time domain modeling in one dimensional photonic crystals, which displays phenomena such as dramatic slow down, unidirectional propagation of the wave, and cup-like singularity of transmittance rate, is demonstrated as well as the sensitivity analysis of periodic layers of photonic crystals. In chapter 4, a method of nonlinear optimization for designing photonic crystals is explained with their computational results and their time domain modeling is displayed to confirm it. Chapter 5 and chapter 6 include the development of thin layer approximations, including the derivation of the thin layer formulation, and convergence test for one and two dimensional problems with examples of successful implementations. Chapter 5 investigates the thin layer approximation for a PEC-backed thin layer while chapter 6 discusses transmission layers. We conclude with a few remarks and future works in chapter 7.

Chapter 2

Maxwell's equations and frozen mode crystals

Let's consider the differential time domain Maxwell's equations in a linear medium,

$$
\begin{aligned}
\nabla \times \mathbf{E} &= -\frac{\partial \mathbf{B}}{\partial t} \\
\nabla \times \mathbf{H} &= \frac{\partial \mathbf{D}}{\partial t} + \mathbf{J} \\
\nabla \cdot \mathbf{D} &= \rho \\
\nabla \cdot \mathbf{B} &= 0
\end{aligned}
$$

with the charge distribution ρ, the electric field $\mathbf{E}$, the electric flux density $\mathbf{D}$, and the magnetic field $\mathbf{H}$. Here,

$$
\begin{aligned}
\mathbf{D} &= \hat{\varepsilon}\mathbf{E} \\
\mathbf{B} &= \hat{\mu}\mathbf{H}
\end{aligned}
$$

where, the relativity permittivity tensor $\hat{\varepsilon}$ and permeability tensor $\hat{\mu}$ are in general anisotropic. The above Maxwell's equations are recovered by normalizing to a unit speed of light, or by normalizing the permittivity and permeability of free space to 1. Note that two divergence equations are redundant as they are contained within the curl equations and the initial boundary conditions. For the discontinuous Galerkin (DG) method formulation, the above equations can be recast into the following form

$$\frac{\partial \mathbf{H}}{\partial t} = -\hat{\mu}^{-1}\{(\nabla \times \mathbf{E}) - \sigma^* \mathbf{H}\} \tag{2.1}$$

$$\frac{\partial \mathbf{E}}{\partial t} = \hat{\varepsilon}^{-1}\{(\nabla \times \mathbf{H}) - \sigma \mathbf{E}\} \tag{2.2}$$

where σ and σ^* indicate electric conductivity and magnetic conductivity, respectively. Also, if we let $\vec{n}$ be a unit normal vector of a material boundary, we have the following boundary conditions

$$\vec{n} \times (\mathbf{E}_1 - \mathbf{E}_2) = 0, \quad \vec{n} \times (\mathbf{H}_1 - \mathbf{H}_2) = 0 \tag{2.3}$$

which indicates the tangential components of $\mathbf{E}$, $\mathbf{H}$ are continuous at any boundaries. The above equations also can be rewritten with the following expressions

$$\begin{aligned} \mathbf{E} &= \mathbf{E}^{inc} + \mathbf{E}^{sct} \\ \mathbf{H} &= \mathbf{H}^{inc} + \mathbf{H}^{sct} \end{aligned}$$

where superscript *inc* indicates the incident field which is determined analytically and superscript *sct* indicates the scattered field which is determined computationally. When the incident wave represents a solution to Maxwell's equations in free space, the scattered field formulation from Eqs. (2.1) and (2.2) can be obtained as

$$\begin{aligned} \frac{\partial \mathbf{H}^s}{\partial t} &= -\hat{\mu}^{-1}\{(\nabla \times \mathbf{E}^s) - \sigma^* \mathbf{H}^s - (\hat{\mu} - \hat{\mathbf{I}})\frac{\partial \mathbf{H}^i}{\partial t} - (\sigma^* - \sigma^{*i})\mathbf{H}^i\} \\ \frac{\partial \mathbf{E}^s}{\partial t} &= \hat{\varepsilon}^{-1}\{(\nabla \times \mathbf{H}) + \sigma \mathbf{E} - (\hat{\varepsilon} - \hat{\mathbf{I}})\frac{\partial \mathbf{E}^i}{\partial t} + (\sigma - \sigma^i)\mathbf{E}^i\} \end{aligned}$$

where, $\hat{\mathbf{I}}$ is the identity matrix. For the investigation of photonic crystals displaying a distinctive electromagnetic phenomenon, called as the frozen mode (see chapter 3), two different types of layers are considered. The one array is a gyrotropic photonic crystal consisting of two anisotropic materials with different in-plane misalignments and one magnetic material. Then, we have the following materials constants of $\hat{\varepsilon}$, $\hat{\mu}$.

$$\begin{aligned} \hat{\varepsilon} = \hat{\varepsilon}^r + i\hat{\varepsilon}^i, \quad \hat{\varepsilon}^r &= \begin{bmatrix} \varepsilon_{xx} & \varepsilon^r_{xy} \\ \varepsilon^r_{xy} & \varepsilon_{yy} \end{bmatrix}, \qquad \hat{\varepsilon}^i = \begin{bmatrix} 0 & \varepsilon^i_{xy} \\ -\varepsilon^i_{xy} & 0 \end{bmatrix} \\ \hat{\mu} = \hat{\mu}^r + i\hat{\mu}^i, \quad \hat{\mu}^r &= \begin{bmatrix} \mu_{xx} & \mu^r_{xy} \\ \mu^r_{xy} & \mu_{yy} \end{bmatrix}, \qquad \hat{\mu}^i = \begin{bmatrix} 0 & \mu^i_{xy} \\ -\mu^i_{xy} & 0 \end{bmatrix} \end{aligned}$$

which leads to the explicit Maxwell's equations on the following form

$$\nabla \times \mathbf{E} = -\hat{\mu}^r(z)\frac{\partial \mathbf{H}}{\partial t} - 2\pi\hat{\mu}^i(z)\mathbf{H}, \qquad \nabla \times \mathbf{H} = \hat{\varepsilon}^r(z)\frac{\partial \mathbf{E}}{\partial t} + 2\pi\hat{\varepsilon}^i(z)\mathbf{E}$$

The other type is a nonmagnetic periodic stack with oblique anisotropy dielectric materials with $\varepsilon_{xy} \neq 0$ and air-filled gap between them. Considering three components of elements **E** and **H**, we have six equations, but assuming the following tangential consistency of the wave to eliminate the derivatives along x, y directions,

$$\frac{dE}{dx} = ik_{x,y}E = \left(\frac{k_{x,y}}{\omega}\right) i\omega E = \left(\frac{k_{x,y}}{\omega}\right)\left(-\frac{dE}{dt}\right)$$

we have only four explicit equations such as,

$$\begin{aligned}
n_x\frac{\varepsilon_{xz}}{\varepsilon_{zz}}\frac{\partial E_x}{\partial t} - n_x n_y\frac{1}{\varepsilon_{zz}}\frac{\partial H_x}{\partial t} + (n_x^2\frac{1}{\varepsilon_{zz}} - 1)\frac{\partial H_y}{\partial t} &= \frac{\partial E_x}{\partial z}\\
n_y\frac{\varepsilon_{xz}}{\varepsilon_{zz}}\frac{\partial E_x}{\partial t} + (1 - n_y^2\frac{1}{\varepsilon_{zz}})\frac{\partial H_x}{\partial t} + n_x n_y\frac{1}{\varepsilon_{zz}}\frac{\partial H_y}{\partial t} &= \frac{\partial E_y}{\partial z}\\
n_y^2\frac{\partial E_x}{\partial t} + (\varepsilon_{yy} - n_x^2)\frac{\partial E_y}{\partial t} &= \frac{\partial H_x}{\partial z}\\
(n_y^2 - \varepsilon_{xx} + \frac{\varepsilon_{xz}^2}{\varepsilon_{zz}})\frac{\partial E_x}{\partial t} - n_x n_y\frac{\partial E_y}{\partial t} - n_x\frac{\varepsilon_{xz}}{\varepsilon_{zz}}\frac{\partial H_x}{\partial t} + n_y\frac{\varepsilon_{xz}}{\varepsilon_{zz}}\frac{\partial H_y}{\partial t} &= \frac{\partial H_y}{\partial z}
\end{aligned}$$

where $n_x = ck_x/\omega, \;\; n_y = ck_y/\omega$ and $k_{x,y}$ is the wave vector along $x, \; y$ directions and ω is the frequency of the incident wave.

Chapter 3

Modeling of the frozen mode phenomenon and its sensitivity

In this chapter, we investigate the behavior and sensitivity of the frozen mode phenomenon in finite structures with anisotropic materials, including both magnetic materials and non-normal incidence. The studies are done by using a high-order accurate discontinuous Galerkin method for solving Maxwells equations in the time domain. We confirm the existence of the phenomenon also in the time-domain and study carefully the impact of the finite crystal on the frozen mode. This sets the stage for a thorough study of the robustness of the frozen mode phenomenon, resulting in guidelines for which design parameters are most sensitive and acceptable tolerances.

3.1 Introduction

The use of complex metamaterials for controlling the propagation and manipulation of electromagnetic energy continues to attract significant interest among engineers. Recently, there has been a flurry of activity in the study and development of periodic structures comprising of several different anisotropic materials after it was shown that such structures could support highly unusual electromagnetic phenomena [8, 9, 10] such as a non-reciprocal propagation, very low transmission loss into the crystal and perhaps a most interesting phenomenon known as the frozen mode.

The frozen mode is a distinctive phenomenon related to stationary inflection points of the dispersion relations $\omega(k)$ such as,

$$\frac{\partial \omega}{\partial k} = 0; \qquad \frac{\partial^2 \omega}{\partial k^2} = 0; \qquad \frac{\partial^3 \omega}{\partial k^3} \neq 0 \quad \text{at} \;\; \omega = \omega_0$$

When a monochromatic wave with frequency ω_0 propagates into a periodic array of unit cells with this dispersion relation, the wave shows the following striking features due to the significantly large transmittance rate at inflection points contrary to the negligible transmittance rate at band edges [8],

- dramatic slow-down of the waves
- enormously increased field amplitude
- cup-like singularity of the transmittance rate
- unidirectionality of monochromatic waves

Let us briefly explain these features in the following. Fig. 3.1 shows two different types of dispersion relation for two different layers, but both of them contain the same kind of inflection point ω_0. At each ω_0 in Fig. 3.1, we have two eigenmodes k_0 and k_1 such that $\frac{\partial \omega}{\partial k}|_{k=k_0} = 0$, $\frac{\partial \omega}{\partial k}|_{k=k_1} < 0$ and only the eigenmode at k_1 transfers the energy. Since we have no eigenmode with a positive group velocity, the transmitted wave doesn't transfer the energy in the direction of the propagation. Physically, it means that the incident electromagnetic wave slows down with infinitesimal group velocity within the periodic layers. However, if a wave propagates in the opposite direction, we have $\frac{\partial \omega}{\partial k}|_{k=k_1} > 0$ and the eigenmode k_1 transfers the energy and consequently the abnormal slow-down vanishes. Thus, the crystal behaves differently depending on the vector of propagation, a phenomenon known as *electromagnetic unidirectionality.*

When the frequency of the wave is close to ω_0, a transmitted wave consists of propagation components and evanescent components. The latter decays as the wave proceeds along the propagation direction, but the former remains to propagate. Both components initially increase dramatically, but the magnitude of them remains almost equal with opposite sign. Thus, the field amplitude at the interface of the layer and vacuum remain almost the same, but once the wave precedes into the slab, the evanescent components die out and only the

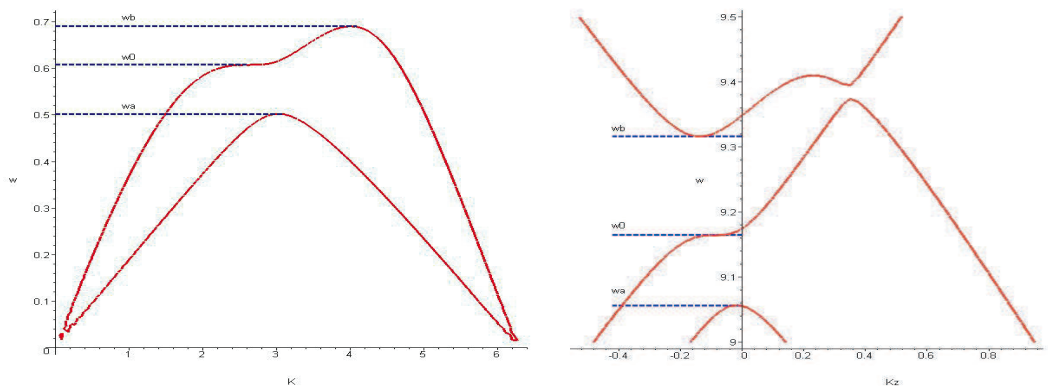

Figure 3.1: Dispersion relations for two different types of layer. gyrotropic photonic crystals (left, $\omega_b = 0.690320778$, $\omega_0 = 0.607676756$, $\omega_a = 0.502044368$) and oblique anisotropic layers (right, $\omega_b = 9.3160209805$, $\omega_0 = 9.164450223$, $\omega_a = 9.0569705995$). ω and k are expressed in units of c/L and $1/L$.

dramatically amplified propagation components remain and contribute to the increase of the field amplitude. This propagation of amplified extended mode also explains the abnormal cup-like singularity of transmittance coefficients depending on the incident wave polarization.

These unique features of the frozen mode have been attractive for numerous practical applications, but the existence of frozen mode itself was theoretically based on at least two impractical assumptions: *infinity* and *periodicity*. Furthermore, all parameters for the above dispersion relations should be exact up to at least $3 \sim 4$ digits with an infinite number of unit cells stacked up along z direction to yield the desired phenomena.

However, in real applications a layer cannot be infinitely long and every unit cell cannot be exactly the same due to practical limitations in the fabrication. These issues could prohibit the realization of frozen mode, although Figotin and Vitebsky suggested in [9] that the phenomena would be robust, since the density of modes of inflection points is abnormally stronger than that of band edges.

Hence, it is natural to study the impact of finiteness of the crystals as well as the sensitivity of the phenomenon to variations in some of the parameters, e.g., material parameters, degree of anisotropy etc, to gain an improved understanding of the practicality of utilizing the frozen mode phenomena.

For this investigation, we use a discontinuous Galerkin method(DG) with a multi-element formulation for the modeling of the frozen mode in the time domain [18, 19]. We have adopted the scattered formulation for Maxwell equation to ease the boundary conditions concerning scattered objects and we put Absorbing boundary condition (ABC) at the end of z direction to prevent unnecessary reflected waves.

The remaining part of this chapter is organized as follows. In section 3.2, we briefly discuss Maxwell's equations in the time domain. In section 3.3, the details of the schemes including discontinuous Galerkin Methods, time stepping, filtering and absorbing boundary condition are described and also several numerical tests with their results are shown. Section 3.4 discusses the modeling of the frozen mode with a large number of unit cells and assess the effect of a finite number of unit cells. In section 3.5, we study the sensitivity of the frozen mode phenomena to variations in critical parameters while concluding remarks are given in section 3.6.

3.2 Formulation

We model two different types of layers. The one array is referred to as a gyrotropic photonic crystal and it consists of two anisotropic materials with different in-plane misalignments ($\mathbf{A_1}, \mathbf{A_2}$) and one strong magnetic material($\mathbf{F}$)(see the left of Fig. 3.2). When it is in a certain special combination, it shows the strong Faraday rotation(circular birefringence) of light polarization in the absence of magnetic field, which results in spectral nonreciprocity($\omega(\vec{k}) \neq \omega(-\vec{k})$) [8, 9, 12, 25, 35].

The other configuration is a nonmagnetic periodic stack with oblique anisotropy dielectric materials with($\varepsilon_{xy} \neq 0$) and air-filled gap between them [12, 22, 35] (see the right of Fig. 3.2). When an incident wave is propagating into the layer at an oblique angle, then the axial spectral asymmetry is obtained, i.e., $\omega(\vec{k}_x, \vec{k}_y, \vec{k}_z) \neq \omega(\vec{k}_x, \vec{k}_y, -\vec{k}_z)$.

In the remaining part of this section, we describe the discrete formulations of Maxwell's equations for these two different layers. For simplicity, we call the former case as the magnetic frozen mode and the latter as the oblique frozen mode.

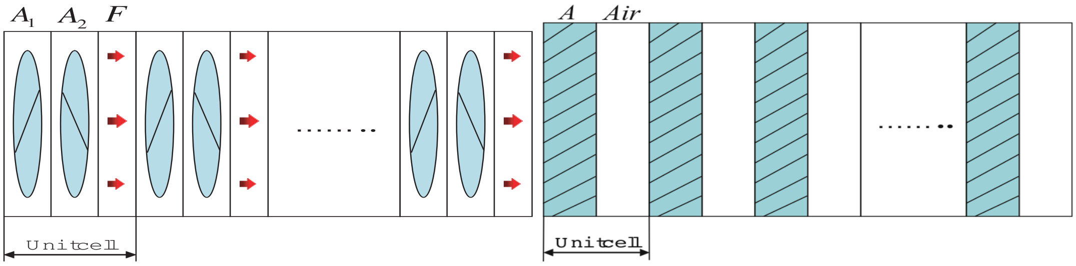

Figure 3.2: Periodic structure of gyrotropic photonic crystals consisting of two different anisotropic materials with one magnetic layer (left) and oblique anisotropic layers consisting of one anisotropic material with vacuum (right). **A**: anisotropic layer, **F**: magnetic layer, **Air**: air-filled gap.

3.2.1 The magnetic frozen mode

We consider the following Maxwell's equations

$$\nabla \times \tilde{\mathbf{E}} = -\frac{d\tilde{\mathbf{B}}}{dt}, \qquad \nabla \times \tilde{\mathbf{H}} = \frac{d\tilde{\mathbf{D}}}{dt}$$

where $\tilde{\mathbf{E}}$ and $\tilde{\mathbf{H}}$ are the electric field and the magnetic field, respectively while $\tilde{\mathbf{D}}$ and $\tilde{\mathbf{B}}$ the displacement field and the induction field. If the direction of the wave propagation z is normal to the layers, these fields are related by linear constitutive relations as follows.

$$\tilde{\mathbf{D}}(z) = \hat{\varepsilon}(z)\tilde{\mathbf{E}}(z), \qquad \tilde{\mathbf{B}}(z) = \hat{\mu}(z)\tilde{\mathbf{H}}(z)$$

where, hat indicates the corresponding quantity is a matrix. These relations yield the following Maxwell's equations in the time domain.

$$\nabla \times \tilde{\mathbf{E}} = -\hat{\mu}^r(z)\frac{\partial \tilde{\mathbf{H}}}{\partial t} - \omega\hat{\mu}^i(z)\tilde{\mathbf{H}}, \qquad \nabla \times \tilde{\mathbf{H}} = \hat{\varepsilon}^r(z)\frac{\partial \tilde{\mathbf{E}}}{\partial t} + \omega\hat{\varepsilon}^i(z)\tilde{\mathbf{E}} \tag{3.1}$$

The superscript r, i denotes the real part and the imaginary part of the components, respectively and ω is the center frequency for which these material parameters are given. To simplify the above equations, we introduce the normalized quantities using

$$z = \frac{\tilde{z}}{\tilde{L}}, \quad t = \frac{\tilde{t}}{\tilde{L}/\tilde{c}_0}$$

where, $\tilde{L}$ is a reference length and $\tilde{c_0} = (\tilde{\varepsilon}_0\tilde{\mu}_0)^{\frac{1}{2}}$ is the dimensional speed of light in vacuum when $\tilde{\varepsilon_0}$ and $\tilde{\mu_0}$ refer to the vacuum permittivity and permeability respectively. Also, $\tilde{\mathbf{E}}$ and $\tilde{\mathbf{H}}$ are normalized as

$$\mathbf{E} = \sqrt{\frac{\tilde{\varepsilon_0}}{\tilde{\mu_0}}}\frac{\tilde{\mathbf{E}}}{\tilde{H}_0}, \qquad \mathbf{H} = \frac{\tilde{\mathbf{H}}}{\tilde{H}_0}$$

where $\tilde{H}_0$ is a dimensional reference magnetic field strength. By substituting these normalized quantities into Eq. (3.1), we obtain the following non-dimensionalized equations

$$\nabla \times \mathbf{E} = -\hat{\mu}^r(z)\frac{\partial \mathbf{H}}{\partial t} - 2\pi\hat{\mu}^i(z)\mathbf{H}, \qquad \nabla \times \mathbf{H} = \hat{\varepsilon}^r(z)\frac{\partial \mathbf{E}}{\partial t} + 2\pi\hat{\varepsilon}^i(z)\mathbf{E} \tag{3.2}$$

which is the most general model for what we shall consider. For the magnetic frozen mode, we consider the following material constant of $\hat{\varepsilon}$, $\hat{\mu}$.

$$\begin{aligned}
\hat{\varepsilon} = \hat{\varepsilon}^r + i\hat{\varepsilon}^i, \quad \hat{\varepsilon}^r &= \begin{bmatrix} \varepsilon_{xx} & \varepsilon^r_{xy} \\ \varepsilon^r_{xy} & \varepsilon_{yy} \end{bmatrix}, \qquad \hat{\varepsilon}^i = \begin{bmatrix} 0 & \varepsilon^i_{xy} \\ -\varepsilon^i_{xy} & 0 \end{bmatrix} \\
\hat{\mu} = \hat{\mu}^r + i\hat{\mu}^i, \quad \hat{\mu}^r &= \begin{bmatrix} \mu_{xx} & \mu^r_{xy} \\ \mu^r_{xy} & \mu_{yy} \end{bmatrix}, \qquad \hat{\mu}^i = \begin{bmatrix} 0 & \mu^i_{xy} \\ -\mu^i_{xy} & 0 \end{bmatrix}
\end{aligned}$$

Then, we obtain the explicit Maxwell's equations for the modeling of the magnetic frozen mode on the form

$$\begin{aligned}
\varepsilon_{xx}\frac{\partial E_x}{\partial t} + \varepsilon^r_{xy}\frac{\partial E_y}{\partial t} &= -\frac{\partial H_y}{\partial z} - 2\pi\varepsilon^i_{xy}E_y \\
\varepsilon^r_{xy}\frac{\partial E_x}{\partial t} + \varepsilon_{yy}\frac{\partial E_y}{\partial t} &= \frac{\partial H_x}{\partial z} + 2\pi\varepsilon^i_{xy}E_x \\
\mu_{xx}\frac{\partial H_x}{\partial t} + \mu^r_{xy}\frac{\partial H_y}{\partial t} &= \frac{\partial E_y}{\partial z} - 2\pi\mu^i_{xy}H_y \\
\mu^r_{xy}\frac{\partial H_x}{\partial t} + \mu_{yy}\frac{\partial H_y}{\partial t} &= -\frac{\partial E_x}{\partial z} + 2\pi\mu^i_{xy}H_x
\end{aligned}$$

Note that ε^i_{xy} and μ^i_{xy} are not loss, but responsible for the Faraday rotation of the electromagnetic waves. Thus, the above equations preserve energy and can be easily shown to be stable in the sense that $\frac{d\mathbf{E}^{\mathbf{\Omega}}}{dt} = 0$ when the energy $\mathbf{E}^{\Omega}$ is defined as $\mathbf{E}^{\mathbf{\Omega}} = \int_{\Omega} \vec{E}^T\hat{\varepsilon}\vec{E} + \vec{H}^T\hat{\mu}\vec{H}$.

When the materials are given as follows [9], we recover the dispersion relation as shown in Fig. 3.1 (left).

$$\text{For } \mathbf{A} \text{ layer} : \hat{\varepsilon} = \begin{bmatrix} 13.61 + 12.40\cos(2\phi) & 12.40\sin(2\phi) \\ 12.40\sin(2\phi) & 13.61 - 12.40\cos(2\phi) \end{bmatrix}, \qquad \hat{\mu} = \begin{bmatrix} 1 & 0 \\ 0 & 1 \end{bmatrix}$$

$$\text{For } \mathbf{F} \text{ layer} : \hat{\varepsilon} = \begin{bmatrix} 5.0 & 0.0 \\ 0.0 & 5.0 \end{bmatrix}, \qquad \hat{\mu} = \begin{bmatrix} 60.0 & i37.0 \\ -i37.0 & 60.0 \end{bmatrix}$$

where, ϕ is the misalignment angle of the two anisotropic layers and we let $\phi_1 = 0$ for the first anisotropic layer and $\phi_2 = \pi/4$ for the second anisotropic layer. Also, we take the thickness of the F layer as 0.0047454 (L) and the frequency of incident wave $\omega = 0.607676756$ (c/L), where L is the thickness of unit cell and c is the speed of light in vacuum.

3.2.2 The oblique frozen mode

The structure of this crystal seems to be much simpler than the gyrotropic photonic crystal, but in order to achieve the axial spectral asymmetry $(\omega(\vec{k}_x, \vec{k}_y, \vec{k}_z) \neq \omega(\vec{k}_x, \vec{k}_y, -\vec{k}_z))$, the following two conditions should be satisfied: the oblique anisotropy should not be in-plane or axial and the Bloch wave $\vec{k}$ has to be oblique to the layers, i.e.

$$1)\ \varepsilon_{xz} \neq 0 \ \text{ and/or } \ \varepsilon_{yz} \neq 0, \quad 2)\ k_x \neq 0 \ \text{ and/or } \ k_y \neq 0$$

Assume that their tangential components k_x, k_y are all the same for the incident, reflected, and transmitted waves and let only k_z be different. In other words, we seek a solution of the following form

$$\mathbf{E}(x, y, z) = e^{i(k_x x + k_y y)} E(z), \qquad \mathbf{H}(x, y, z) = e^{i(k_x x + k_y y)} H(z)$$

When this form of the solution is substituted, we have six equations, but considering only k_z components, the last row of each equation in Eq. (3.1) can be used to complement the other equations. Thus, similar to the magnetic frozen mode, we have only four equations. The explicit equations for the oblique frozen mode modeling are expressed as

$$
\begin{aligned}
n_x \frac{\varepsilon_{xz}}{\varepsilon_{zz}} \frac{\partial E_x}{\partial t} - n_x n_y \frac{1}{\varepsilon_{zz}} \frac{\partial H_x}{\partial t} + (n_x^2 \frac{1}{\varepsilon_{zz}} - 1) \frac{\partial H_y}{\partial t} &= \frac{\partial E_x}{\partial z} \\
n_y \frac{\varepsilon_{xz}}{\varepsilon_{zz}} \frac{\partial E_x}{\partial t} + (1 - n_y^2 \frac{1}{\varepsilon_{zz}}) \frac{\partial H_x}{\partial t} + n_x n_y \frac{1}{\varepsilon_{zz}} \frac{\partial H_y}{\partial t} &= \frac{\partial E_y}{\partial z} \\
n_y^2 \frac{\partial E_x}{\partial t} + (\varepsilon_{yy} - n_x^2) \frac{\partial E_y}{\partial t} &= \frac{\partial H_x}{\partial z} \\
(n_y^2 - \varepsilon_{xx} + \frac{\varepsilon_{xz}^2}{\varepsilon_{zz}}) \frac{\partial E_x}{\partial t} - n_x n_y \frac{\partial E_y}{\partial t} - n_x \frac{\varepsilon_{xz}}{\varepsilon_{zz}} \frac{\partial H_x}{\partial t} + n_y \frac{\varepsilon_{xz}}{\varepsilon_{zz}} \frac{\partial H_y}{\partial t} &= \frac{\partial H_y}{\partial z}
\end{aligned}
$$

where $n_x = ck_x/\omega, \quad n_y = ck_y/\omega$.

With the following materials specified as in [22], we obtain the dispersion relation as shown in Fig. 3.1 (right).

$$
\begin{aligned}
\hat{\varepsilon}_A &= \begin{bmatrix} 4.62\cos\theta^2 + 3.78\sin\theta^2 & 0 & 0.84\cos\theta\sin\theta \\ 0 & 4.62 & 0 \\ 0.84\cos\theta\sin\theta & 0 & 3.78\cos\theta^2 + 4.62\sin\theta^2 \end{bmatrix}_{\theta=\pi/4} \\
\hat{\varepsilon}_B &= \begin{bmatrix} 1 & 0 & 0 \\ 0 & 1 & 0 \\ 0 & 0 & 1 \end{bmatrix}, \quad \hat{\mu}_A = \hat{\mu}_B = I
\end{aligned}
$$

We let the thickness of A layer be the same as that of vacuum. Also, the tangential components of the incident wave vector are $n_x = n_y = -0.493489$ and the frequency of the wave is 9.164450223 (c/L).

3.3 Numerical scheme

Let $\mathbf{q} = [E_x \ E_y \ H_x \ H_y]$. Then, the two equations with different material coefficients are reduced to one general problem on the form

$$
\frac{\partial \mathbf{q}}{\partial t} + \frac{\partial \mathbf{q}}{\partial z} \hat{\mathbf{A}} + \mathbf{q}\hat{\mathbf{B}} = \mathbf{0} \tag{3.3}
$$

For the magnetic frozen mode,

$$
\begin{aligned}
\hat{\mathbf{A}} &= \mathbf{A}\mathbf{Q}^{-1}, \quad \hat{\mathbf{B}} = \mathbf{B}\mathbf{Q}^{-1} \\
\mathbf{Q} &= \begin{bmatrix} \mathbf{Q}_{11} & \mathbf{0} \\ \mathbf{0} & \mathbf{Q}_{22} \end{bmatrix}, \quad \mathbf{Q}_{11} = \begin{bmatrix} \varepsilon_{xx} & \varepsilon^r_{xy} \\ \varepsilon^r_{xy} & \varepsilon_{yy} \end{bmatrix}, \mathbf{Q}_{22} = \begin{bmatrix} \mu_{xx} & \mu^r_{xy} \\ \mu^r_{xy} & \mu_{yy} \end{bmatrix} \\
\mathbf{A} &= \begin{bmatrix} \mathbf{0} & \mathbf{A}_{12} \\ \mathbf{A}_{21} & \mathbf{0} \end{bmatrix}, \quad \mathbf{A}_{12} = \begin{bmatrix} 0 & -1 \\ 1 & 0 \end{bmatrix}, \mathbf{A}_{21} = \begin{bmatrix} 0 & 1 \\ -1 & 0 \end{bmatrix} \\
\mathbf{B} &= \begin{bmatrix} \mathbf{B}_{11} & \mathbf{0} \\ \mathbf{0} & \mathbf{B}_{22} \end{bmatrix}, \quad \mathbf{B}_{11} = \begin{bmatrix} 0 & -\varepsilon^i_{xy} \\ \varepsilon^i_{xy} & 0 \end{bmatrix}, \mathbf{B}_{22} = \begin{bmatrix} 0 & -\mu^i_{xy} \\ \mu^i_{xy} & 0 \end{bmatrix}
\end{aligned}
$$

and for the oblique frozen mode,

$$
\begin{aligned}
\hat{\mathbf{A}} &= \mathbf{Q}^{-1}, \quad \hat{\mathbf{B}} = \mathbf{0} \\
\mathbf{Q} &= \begin{bmatrix} \mathbf{Q}_{11} & \mathbf{Q}_{12} \\ \mathbf{Q}_{21} & \mathbf{Q}_{22} \end{bmatrix} \\
\mathbf{Q}_{11} &= \begin{bmatrix} n_x(\varepsilon_{xz}/\varepsilon_{zz}) & 0 \\ n_y(\varepsilon_{xz}/\varepsilon_{zz}) & 0 \end{bmatrix}, \mathbf{Q}_{12} = \begin{bmatrix} -n_x n_y(1/\varepsilon_{zz}) & n_x^2(1/\varepsilon_{zz}) - 1 \\ 1 - n_y^2(1/\varepsilon_{zz}) & n_x n_y(1/\varepsilon_{zz}) \end{bmatrix} \\
\mathbf{Q}_{21} &= \begin{bmatrix} n_x n_y & \varepsilon_{yy} - n_x^2 \\ n_y^2 - \varepsilon_{xx} + \varepsilon_{xz}^2/\varepsilon_{zz} & -n_x n_y \end{bmatrix}, \mathbf{Q}_{22} = \begin{bmatrix} 0 & 0 \\ -n_y(\varepsilon_{xz}/\varepsilon_{zz}) & n_x(\varepsilon_{xz}/\varepsilon_{zz}) \end{bmatrix}
\end{aligned}
$$

Suppose that the domain Ω can be segmented into K non-overlapping layers. In each elements, we assume that the approximated solution $\mathbf{q}^k_N(z,t)$ can be represented as an N'th order polynomial, i.e.,

$$
\mathbf{q}^k_N(z,t) = \sum_{i=0}^{N} \hat{\mathbf{q}}^k_i \phi_i(z^k) = \sum_{i=0}^{N} \mathbf{q}^k_i(t)\ell^k_i(z^k) \tag{3.4}
$$

where, z^k is in the element $[z^k_-, z^k_+]$ which is linearly mapped satisfying $z^k(-1) = z^k_-$, $z^k(1) = z^k_+$. Also note that ℓ^k_i is Lagrange polynomial based on grid points z^k_i. There are many ways in choosing ϕ_n and segmentation of the domain Ω, but for easy implementation with high accuracy and efficiency, we use Legendre polynomials $P_n(z)$ [31] for $\phi(z)$. Then ϕ and ℓ_i have the following relation

$$
\hat{\mathbf{V}}^T \vec{\ell}^k(z^k) = \vec{\phi}(z^k), \quad \hat{\mathbf{V}} = [V_{ij}] = [P_j(z_i)] \tag{3.5}
$$

where,

$$\vec{\ell}^k = [\ell_0^k\ \ell_1^k \cdots \ell_N^k], \quad \vec{\phi}^k = [\phi_0^k\ \phi_1^k \cdots \phi_N^k]$$

The semi-discrete scheme is derived by requiring that

$$\int_{z_-^k}^{z_+^k} (\frac{\partial \mathbf{q}_N}{\partial t} + \frac{\partial \mathbf{q}_N}{\partial z}\hat{\mathbf{A}} + \mathbf{q}_N \hat{\mathbf{B}})\ell_i^k(z)dz = \mathbf{0}, \qquad 0 \le i \le N$$

Executing two integrations by parts, we have the following form,

$$\int_{z_-^k}^{z_+^k} (\frac{\partial \mathbf{q}_N}{\partial t} + \frac{\partial \mathbf{q}_N}{\partial z}\hat{\mathbf{A}} + \mathbf{q}_N \hat{\mathbf{B}})\ell_i^k(z)dz = \int_{z_-^k}^{z_+^k} \hat{n}[(\mathbf{q}_N\hat{\mathbf{A}})^- - (\mathbf{q}_N\hat{\mathbf{A}})^*]\ell_i^k(z)dz \quad (3.6)$$

where, $\hat{n}$ is an outward normal vector. Here, we use a numerical flux $(\mathbf{q}_N\hat{\mathbf{A}})^*$ such that

$$[\mathbf{q}_N\hat{\mathbf{A}}]^* = (\mathbf{q}_N^-, \mathbf{q}_N^+)\hat{\mathbf{A}}$$

where, $\mathbf{q}^-$ is a local solution and $\mathbf{q}^+$ a solution in the neighboring element. The reason we need a flux in the above equation is that there are two different solutions on the same interface, since $z_+^k = z_-^{k+1}$. Among many possible fluxes, upwind flux [2] or a simpler central flux [19] are often preferred. We shall use the central flux for our semi-discrete scheme as following.

$$(\mathbf{q}_N^-, \mathbf{q}_N^+)\hat{\mathbf{A}} = \frac{1}{2}(\mathbf{q}_N^+ + \mathbf{q}_N^-)\hat{\mathbf{A}} \quad (3.7)$$

Let's define the following mass matrix and stiff matrix($h^k = z_+^k - z_-^k$)

$$\begin{aligned} M_{ij} &= \int_{z_-^k}^{z_+^k} \ell_i^k(z^k)\ell_j^k(z^k)dz^k = \frac{h^k}{2}\int_{-1}^{1} \ell_i(r)\ell_j(r)dr \\ S_{ij} &= \int_{z_-^k}^{z_+^k} \ell_i^k(z^k)\frac{d\ell_j}{dz}dz^k = \int_{-1}^{1} \ell_i(r)\frac{d\ell_j}{dr}dr, \qquad 0 \le i, j \le N \end{aligned}$$

Then, using the Eq. (3.5) we obtain the following relation

$$\mathbf{M} = (\mathbf{V}^{-1})^T\mathbf{V}^{-1}, \quad \mathbf{S} = (\mathbf{V}^T)^{-1}\mathbf{W}\mathbf{V}^{-1}, \quad W_{ij} = \int_{-1}^{1} \phi_i(r)\phi_j^{'}(r)dr$$

With the definition of the above matrix and the central flux, Eq. (3.7), we have the following local semi-discrete scheme.

$$\begin{aligned}\frac{h^k}{2}\hat{\mathbf{M}}\frac{d\mathbf{q}_N}{dt} + \hat{\mathbf{S}}\mathbf{q}_N\hat{\mathbf{A}} + \frac{h^k}{2}\hat{\mathbf{M}}\mathbf{q}_N\hat{\mathbf{B}} \\ = \frac{e_0}{2}[(-\mathbf{q}_N^- + \mathbf{q}_N^+)\hat{\mathbf{A}}]_{z_-^k} + \frac{e_N}{2}[(\mathbf{q}_N^- - \mathbf{q}_N^+)\hat{\mathbf{A}}]_{z_+^k}\end{aligned} \tag{3.8}$$

where e_i is a N+1 long zero vector with 1 only for its i'th component and $[\ ]_a$ refers to the evaluation of $[\ ]$ at $x = a$. We see that the inverse of $\hat{\mathbf{M}}$ exists and can be easily computed because it is only a local matrix, thus by multiplying $\hat{\mathbf{M}}^{-1}$, we finally obtain our semi-discrete scheme

$$\begin{aligned}\frac{d\mathbf{q}_N}{dt} + \frac{2}{h^k}(\hat{\mathbf{M}}^{-1}\hat{\mathbf{S}})\mathbf{q}_N\hat{\mathbf{A}} + \mathbf{q}_N\hat{\mathbf{B}} \\ = \frac{e_0}{h^k}[\hat{\mathbf{M}}^{-1}(-\mathbf{q}_N^- + \mathbf{q}_N^+)\hat{\mathbf{A}}]_{z_-^k} + \frac{e_N}{h^k}[\hat{\mathbf{M}}^{-1}(\mathbf{q}_N^- - \mathbf{q}_N^+)\hat{\mathbf{A}}]_{z_+^k}\end{aligned}$$

which reads in the scattered field formulation,

$$\begin{aligned}\frac{d\mathbf{q}_N^{scat}}{dt} = -\frac{2}{h^k}((\hat{\mathbf{M}}^{-1}\hat{\mathbf{S}})\mathbf{q}_N^{scat}\hat{\mathbf{A}} - \mathbf{q}_N^{scat}\hat{\mathbf{B}} + (\hat{\mathbf{Q}}^{-1} - \mathbf{I})\frac{d\mathbf{q}_N^{inc}}{dt} - \mathbf{q}_N^{inc}\hat{\mathbf{B}} \\ + \frac{e_0}{h^k}[\hat{\mathbf{M}}^{-1}(-(\mathbf{q}_N^{scat})^- + (\mathbf{q}_N^{scat})^+)\hat{\mathbf{A}}]_{z_-^k} + \frac{e_N}{h^k}[\hat{\mathbf{M}}^{-1}(\mathbf{q}_N^{scat})^- - (\mathbf{q}_N^{scat})^+)\hat{\mathbf{A}}]_{z_+^k}\end{aligned} \tag{3.9}$$

where, $\mathbf{q}^{inc}$ represents the incident field and $\mathbf{q}^{scat}$ the scattered field. Note that for the scattered field formulation, only the scattered field is computed in the problem space and the incident field is specified analytically throughout the problem space.

The consistency of this scheme can be easily proved from general polynomial approximation theorem. Furthermore, stability can be shown using energy methods as discussed in detail in [16].

3.3.1 Time stepping

For the time marching, we can use the classical 4th order Runge-Kutta scheme. However, for explicit time-integration schemes the stable time step will scale as

$$\Delta t \propto \frac{h}{N^2}$$

with N being the order of approximation and h being the length of the smallest interval. In the particular applications being considered the very thin magnetic F layers will prove explicit time-integration prohibitive.

To overcome the long time integration due to a excessively small time step, we use a Diagonally Implicit-Runge-Kutta(DIRK) 3rd order method [3]. The L-stability of this DIRK 3rd order enables us to choose Δt independent of the size of the elements to the extend of acceptable accuracy. Considering the linearity of the equations, we can rewrite Eq. (3.9) as following by introducing matrices $\hat{\mathbf{T}}^s$,$\hat{\mathbf{T}}^i$,

$$\frac{d\mathbf{q}_N^{scat}}{dt} = \hat{\mathbf{T}}^s \mathbf{q}_N^{scat}(t) + \hat{\mathbf{T}}^i \mathbf{q}_N^{inc}(t)$$

Then, applying the DIRK 3rd order yields

$$\begin{aligned}
(I - \gamma\Delta t\hat{\mathbf{T}}^s)\mathbf{Y}_1^{scat} &= \mathbf{q}_N^{scat}(t) + \Delta t\ [\gamma\hat{\mathbf{T}}^i\mathbf{q}_N^{inc}(t + c_1\Delta t)] \\
(I - \gamma\Delta t\hat{\mathbf{T}}^s)\mathbf{Y}_2^{scat} &= \mathbf{q}_N^{scat}(t) + \Delta t\ [a_{21}(\hat{\mathbf{T}}^s Y_1 + \hat{\mathbf{T}}^i\mathbf{q}_N^{inc}(t + c_1\Delta t)) + \gamma\hat{\mathbf{T}}^i\mathbf{q}_N^{inc}(t + c_2\Delta t)] \\
(I - \gamma\Delta t\hat{\mathbf{T}}^s)\mathbf{Y}_3^{scat} &= \mathbf{q}_N^{scat}(t) + \Delta t\ [a_{31}(\hat{\mathbf{T}}^s Y_1 + \hat{\mathbf{T}}^i\mathbf{q}_N^{inc}(t + c_1\Delta t)) \\
&\quad + a_{32}(\hat{\mathbf{T}}^s\mathbf{Y}_2 + \hat{\mathbf{T}}^i\mathbf{q}_N^{inc}(t + c_2\Delta t)) + \gamma\hat{\mathbf{T}}^i\mathbf{q}_N^{inc}(t + c_3\Delta t)]
\end{aligned}$$

$$\begin{aligned}
\mathbf{q}_N^{scat} &= \mathbf{q}_N^{scat} + \Delta t\ [b_1(\hat{\mathbf{T}}^s\mathbf{Y}_1 + \hat{\mathbf{T}}^i\mathbf{q}_N^{inc}(t + c_1\Delta t)) \\
&\quad + b_2(\hat{\mathbf{T}}^s\mathbf{Y}_2 + \hat{\mathbf{T}}^i\mathbf{q}_N^{inc}(t + c_2\Delta t)) + b_3(\hat{\mathbf{T}}^s\mathbf{Y}_3 + \hat{\mathbf{T}}^i\mathbf{q}_N^{inc}(t + c_3\Delta t))]
\end{aligned}$$

The Butcher tableau for the considered DIRK scheme is given as

c_1	γ	0	0	0.4358665215	0.4358665215	0	0
c_2	a_{21}	γ	0	0.7179332608	0.2820667392	0.4358665215	0
c_3	a_{31}	a_{32}	γ	1	1.208496649	-0.644363171	0.4358665215
	b_1	b_2	b_3		1.208496649	-0.644363171	0.4358665215

For the 3rd order DIRK method, the most critical issue is to invert $(I - \gamma\Delta t\hat{\mathbf{T}}^s)$ efficiently. However, for the one dimensional DG method, $(I - \gamma\Delta t\hat{\mathbf{T}}^s)$ is very sparse and well distributed along the diagonal elements. Therefore, it is easily solved by simple LU decomposition without deteriorating the speed or accuracy of the scheme.

3.3.2 Filtering

Usually DG schemes using central flux with sufficient resolutions are accurate and stable for linear problems. However, due to the vastly separate scales in this problem with very small domains or some domains with high material coefficients, we observe that the use of a weak exponential filter can be beneficial at moderate resolution points to improve the stability. The detailed discussion on this filtering of spectral method is shown earlier by Hesthaven and Kirby [17]. Here, we briefly present the formulation of a weak exponential filter used in our scheme.

Let $\mathcal{F}_N$ be the filter operator for the polynomial of order N. Then, it can be written as

$$\mathcal{F}_N q^k(x,t) = \sum_{i=0}^{N} \sigma_E(\frac{i}{N})\hat{q}_i^k(t)P_i(x)$$

where,

$$\sigma_E(\eta) \quad = \quad \exp(-\alpha\eta^p), \quad \alpha = -\ln(\varepsilon_M), \quad \varepsilon_M = \text{machine precision}, \quad p \geq 16$$

Now we define the following matrix.

$$\begin{aligned} \mathbf{V}_{ij} &= P_j(x_i), \qquad 0 \leq i,j \leq N \\ \mathbf{F} = [\mathcal{F}_{ii}] &= [\sigma_E(\frac{i}{N})], \qquad 0 \leq i \leq N \end{aligned}$$

where, x_i is the Legendre Gauss Lobatto quadrature point. Then, by substitution, we obtain

$$\mathcal{F}_N \mathbf{q}_N^k = \mathbf{VF}\ \hat{\mathbf{q}}_N^k = \mathbf{VFV}^{-1}\ \mathbf{q}_N^k$$

where, $\mathbf{q}_N^k = [q_0^k, \cdots, q_N^k]^T$, $\hat{\mathbf{q}}_N^k = [\hat{q}_0^k, \cdots, \hat{q}_N^k]^T$.

3.3.3 Absorbing boundary conditions

To attenuate the scattering waves at outer boundaries, we use an absorbing boundary condition(ABC) at each ends of whole domain to suppress reflections of the waves to an acceptable level. This permits the solution to remain valid even for long time intervals [32]. The ABC is to introduce a simple sponge layer with loss in both the magnetic and electromagnetic tensors such as,

$$\nabla \times \mathbf{H}(r) = -i\frac{\omega}{c}\hat{\varepsilon}(z)\begin{bmatrix} s_z & 0 \\ 0 & s_z \end{bmatrix}\mathbf{E}(r)$$

Substituting $s_z = 1 + \frac{c\sigma_z}{i\omega}\hat{\varepsilon}^{-1}(z)$, we have

$$\nabla \times \mathbf{H}(r) = -i\frac{\omega}{c}\hat{\varepsilon}(z)\mathbf{E}(r) + \sigma_z\mathbf{E}(r)$$

where, $\sigma_z(z) = (\frac{z}{d})^m\sigma_{max}, \quad m = 2, 3, 4, \quad \sigma_{max} = \frac{1}{\Delta t}$.

3.3.4 Numerical tests

To verify the convergence and the accuracy of the scheme, we now discuss a couple of numerical convergence tests. The first test concerns the convergence to an analytically known solution and the second one the convergence of transmission/reflection coefficients for simple isotropic materials.

3.3.4.1 Convergence test: isotropic/anisotropic materials

This first test can be found in the paper [1]. Here we extend it to a slightly more general case including anisotropic materials. Let's consider the following Maxwell's equations

$$\begin{aligned} \begin{bmatrix} \varepsilon_{xx} & \varepsilon_{xy} \\ \varepsilon_{xy} & \varepsilon_{yy} \end{bmatrix}\frac{\partial}{\partial t}\begin{bmatrix} E_x \\ E_y \end{bmatrix} &= \begin{bmatrix} 0 & -1 \\ 1 & 0 \end{bmatrix}\frac{\partial}{\partial z}\begin{bmatrix} H_x \\ H_y \end{bmatrix} \\ \frac{\partial}{\partial t}\begin{bmatrix} H_x \\ H_y \end{bmatrix} &= -\begin{bmatrix} 0 & -1 \\ 1 & 0 \end{bmatrix}\frac{\partial}{\partial z}\begin{bmatrix} E_x \\ E_y \end{bmatrix} \end{aligned} \tag{3.10}$$

and a one-dimensional electromagnetic resonator with perfectly conducting walls located at $z^{(1)} = -1$ and $z^{(2)} = 1$. The interior of the resonator is filled with two dielectric media with the material interface at z=0. We impose the following boundary conditions at $z = \pm 1$ and $z = 0$

$$\text{i)}\;\; \mathbf{E} = 0 \quad \text{or} \quad \frac{\partial \mathbf{H}}{\partial z} = 0, \qquad \text{at} \quad z = \pm 1$$

and

$$\text{ii)}\;\; \mathbf{E}^{(1)} = \mathbf{E}^{(2)}, \qquad \mathbf{H}^{(1)} = \mathbf{H}^{(2)}, \qquad \text{at} \quad z = \pm 0$$

The solution of Maxwell's equations (Eq. (3.10)) satisfying the above boundary conditions can be expressed as

$$\begin{aligned}
E_x &= [A^{(k)}e^{in^{(k)}\omega z} - B^{(k)}e^{-in^{(k)}\omega z}] \\
E_y &= [A^{(k)}e^{in^{(k)}\omega z} - B^{(k)}e^{-in^{(k)}\omega z}] \\
H_x &= n^{(k)}[A^{(k)}e^{in^{(k)}\omega z} + B^{(k)}e^{-in^{(k)}\omega z}] \\
H_y &= -n^{(k)}[A^{(k)}e^{in^{(k)}\omega z} + B^{(k)}e^{-in^{(k)}\omega z}]
\end{aligned}$$

where,

$$\begin{aligned}
A^{(1)} &= \frac{n^{(2)}\cos(n^{(2)}\omega)}{n^{(1)}\cos(n^{(1)}\omega)}, \qquad A^{(2)} = e^{-i\omega(n^{(1)}+n^{(2)})} \\
B^{(1)} &= A^{(1)}e^{-i2n^{(1)}\omega}, \qquad B^{(2)} = A^{(2)}e^{i2n^{(2)}\omega} \\
n^{(k)} &= \sqrt{\varepsilon_{xx}^{(k)} + \varepsilon_{xy}^{(k)}} = \sqrt{\varepsilon_{yy}^{(k)} + \varepsilon_{xy}^{(k)}}, \qquad \text{where } \varepsilon_{xx}^{(k)} = \varepsilon_{yy}^{(k)} \text{ is required.}
\end{aligned}$$

Here $n^{(k)} = \sqrt{\varepsilon^{(k)}}$ is the index of refraction in k^{th} material and ω is the solution of the equation

$$-n^{(2)}\tan(n^{(1)}\omega) = n^{(1)}\tan(n^{(2)}\omega)$$

and we consider the following two cases.

$$\begin{aligned}
\text{Case 1} \; &: \; \varepsilon_{xx} = \varepsilon_{yy} = 1.0, \quad \varepsilon_{xy} = 0, \qquad -1 \le z \le 0 \\
&\quad\; \varepsilon_{xx} = \varepsilon_{yy} = 2.25, \quad \varepsilon_{xy} = 0, \qquad 0 \le z \le 1 \\
\text{Case 2} \; &: \; \varepsilon_{xx} = \varepsilon_{yy} = 1.0, \quad \varepsilon_{xy} = 0, \qquad -1 \le z \le 0 \\
&\quad\; \varepsilon_{xx} = \varepsilon_{yy} = 4.0, \quad \varepsilon_{xy} = 1.5, \qquad 0 \le z \le 1
\end{aligned}$$

Using a very small time step, we show the spectral convergence as in the right in Fig. 3.3. Also, with $\Delta t = \text{CFL} * (2/N)$, $\text{CFL} < 1$, we can see the third order temporal convergence of the scheme in the following two tables

1. N is the number of grid points

	N=8	N=16	N=32	N=64	N=128
L_2Error	2.1088e-002	2.8870e-003	3.7544e-004	4.7073e-005	5.9164e-006
Ratio	-	7.3045	7.6896	7.9757	7.9564
Order	-	2.8688	2.9429	2.9956	2.9921

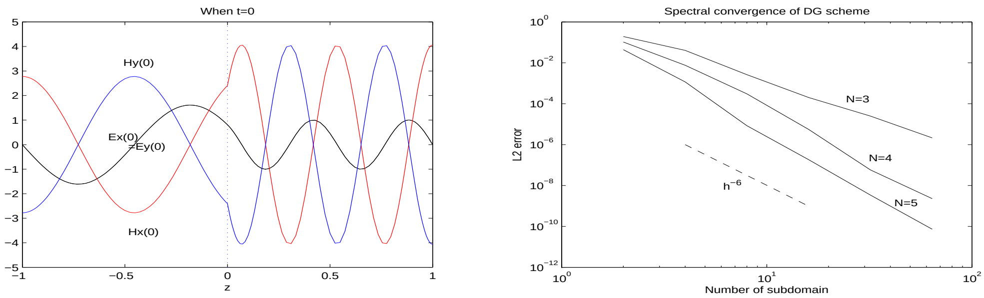

Figure 3.3: The solution E_x, E_y, H_x, H_y of the numerical test 1 at t=0 for case 2 (left) and its spectral convergence (right)

2. N is the number of grid points

	N=8	N=16	N=32	N=64	N=128
L_2Error	3.9821e-001	4.3088e-003	6.3444e-004	7.8858e-005	1.0164e-005
Ratio	-	92.4178	6.7915	8.0453	7.7586
Order	-	6.5301	2.7637	3.0082	2.9558

3.3.4.2 Transmission test

Given the seminal importance of correct transmission and reflection behavior at material interfaces, it is important to confirm this behaviour correctly. Moreover, it is of significance in DG schemes, since the behavior of electromagnetic waves on the interfaces is mainly dealt through the flux terms in DG schemes. In other words, if the transmission rate or the reflection rate does not converge to the known value, it is highly likely to reflect an improper use of the flux and violation of necessary boundary conditions ($n_1 \cdot \varepsilon_1 E_1 = n_2 \cdot \varepsilon_2 E_2, \quad n \times H_1 = n \times H_2$) on the interfaces. Let's consider the following Maxwell's equations

$$
\begin{aligned}
\begin{bmatrix} n^2 & 0 \\ 0 & n^2 \end{bmatrix} \frac{\partial}{\partial t} \begin{bmatrix} E_x \\ E_y \end{bmatrix} &= \begin{bmatrix} 0 & -1 \\ 1 & 0 \end{bmatrix} \frac{\partial}{\partial z} \begin{bmatrix} H_x \\ H_y \end{bmatrix} \\
\frac{\partial}{\partial t} \begin{bmatrix} H_x \\ H_y \end{bmatrix} &= - \begin{bmatrix} 0 & -1 \\ 1 & 0 \end{bmatrix} \frac{\partial}{\partial z} \begin{bmatrix} E_x \\ E_y \end{bmatrix}
\end{aligned}
$$

The following results confirm the convergence of transmission/reflection rates

1. When $n_1 = 1.0, n_2 = 1.5$

	N=6	N=12
Exact value(T/R)	0.96 / 0.04	0.96 / 0.04
By computation(T/R)	0.9593 / 0.0398	0.9599 / 0.04

2. When $n_1 = 1.5, n_2 = 1.0$

	N=6	N=12
Exact value(T/R)	0.8889 / 0.1111	0.8889 / 0.1111
By computation(T/R)	0.8908 / 0.1092	0.8888 / 0.1112

3.4 Modeling of the frozen mode

In the following, we discuss a number of computational studies to confirm the predicted behavior and the appearance of the frozen mode. We focus on a direct validation of the theory as well as an attempt to understand the limitations of the phenomenon in crystals of finite extent.

3.4.1 Modeling with a large number of unit cells

In this section, we model two different types of the frozen modes with as large number of unit cells as possible to observe distinctive features of the phenomena. 200 unit cells for gyrotropic photonic crystals and 100 unit cells for oblique anisotropic layers are used in each modelings. This can be viewed an an attempt to directly validate the theories as laid out in [8, 9, 10].

3.4.1.1 The magnetic frozen mode

The infinite gyrotropic material is modeled with 200 unit cells of the type as shown in Fig. 3.2. As soon as the electromagnetic plane wave enters the slab, the wave gets amplified, it slows down and the field amplitude($|\Psi|^2 = |E_x^2 + E_y^2 + H_x^2 + H_y^2|^2$) increases dramatically inside the slab as shown in Figs. 3.4-3.5. If we consider the maximum peak of the field amplitude as the forefront of the energy density, the average group velocity of the wave, which approximately coincides with the velocity of energy density transfer [5], is around 0.0015c and the average signal velocity, which is defined from the position of half-maximum intensity of the wave

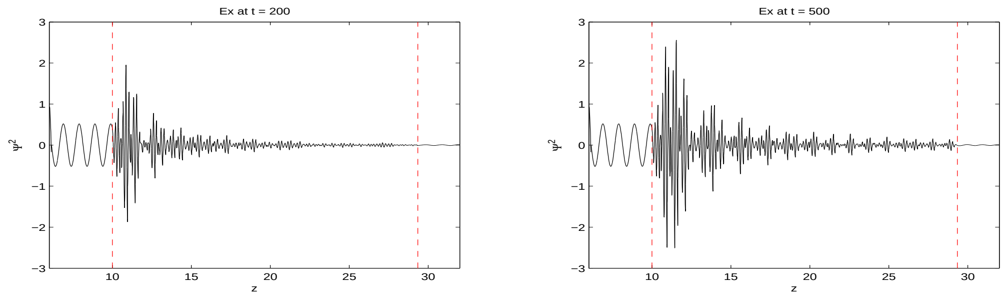

Figure 3.4: Electric field at the frozen mode frequency. Ncell: Number of unit cell = 200, N: Number of grid points per each cell = 8. Δt=0.02. T = 200 (left), T = 500 (right). The incident field is E$\|$x polarized. The dotted lines indicate the outer boundaries of the crystal.

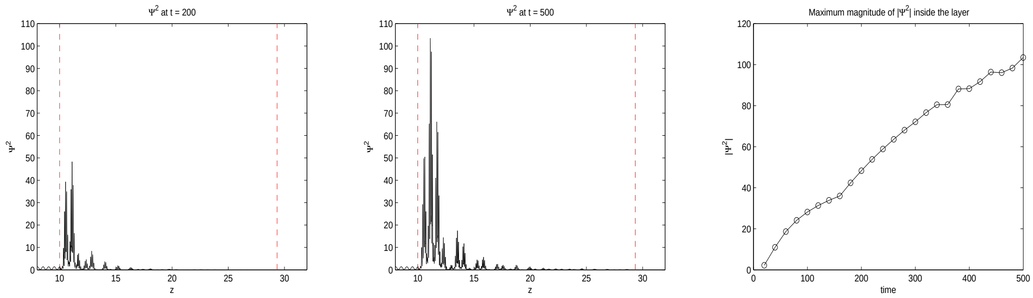

Figure 3.5: Field amplitude($|\psi|^2$) at the frozen mode frequency. Ncell = 200, N= 8. T = 200 (left), T = 500 (center). The rightmost graph shows that the maximum magnitude of field amplitude increases linearly with time. The incident field is E$\|$x polarized. The dotted lines indicate the outer boundaries of the crystal.

[5], is around 0.01c, with c being the speed of light in vacuum. Also, from the right of Fig. 3.5, we observe that the maximum height of field amplitude increases almost linearly and is proportional to the amount of the transmitted wave into the layer. This is in accordance with the predictions [8, 9, 10].

Generally, the energy density flux can be expressed as $< S > = < u > \cdot v$, where $< u >$ is the energy density and v is the group velocity. While the energy density flux remains approximately constant, the energy density inside the slab grows enormously in proportion to the amount of the transmitted wave. The group velocity is inversely proportional to the energy density, so the wave gets slowed down accordingly (Fig. 3.6).

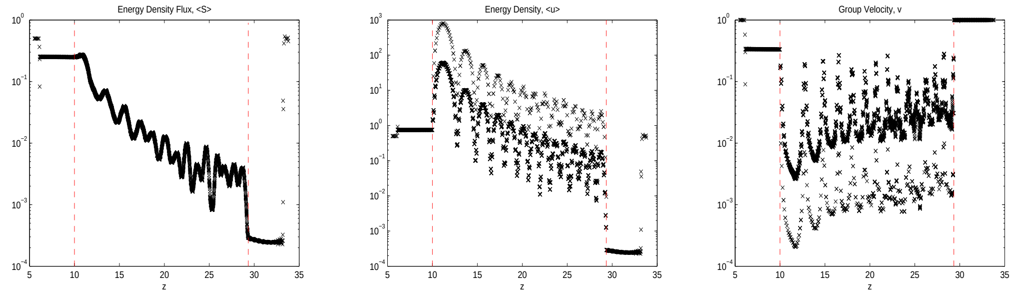

Figure 3.6: Energy density flux (left), Energy density (center), group velocity (right) at the frozen mode frequency in the gyrotropic photonic crystals when T=500.0. Energy density is different between magnetic material and anisotropic material, so this is why we see two separate lines of groups in energy density and group velocity. The incident wave is with constant amplitude and E∥x polarized. The dotted line indicates the outer boundaries of the crystal.

Also note that energy density flux is almost the same for these two materials, but the energy density in the magnetic material is much higher than that in anisotropic material. Consequently, the group velocity of the wave is much slower in the magnetic materials. This is why we see two lines in group velocity and energy density in Fig. 3.6.

If an electromagnetic wave at the frozen mode frequency propagates in the opposite direction, we clearly see that abnormality of the frozen mode has disappeared (left in Fig. 3.7). The electromagnetic wave reaches the other end with normal speed and there is no amplification of the field amplitude. Similarly, if the thickness ratio of **F** or the frequency of the incident wave is changed a little bit, none of the distinctive features of the frozen mode is observed, as also illustrated in Fig. 3.7.

3.4.1.2 The oblique frozen mode

We repeat the computational experiment for the purely dielectric case using 100 unit cells of the type shown in Fig. 3.2. We display the electromagnetic wave in Fig. 3.8 and the field amplitude in Fig. 3.9 inside the oblique anisotropic layers along the z direction.

The features of the oblique frozen mode are similar to those of the magnetic

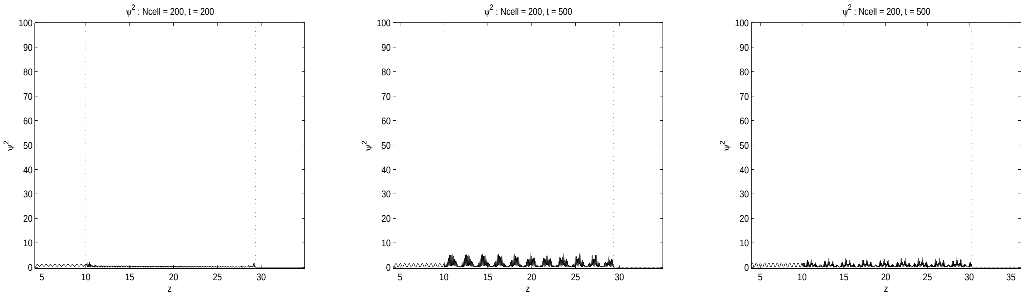

Figure 3.7: Field amplitude for the backward direction (left), $\frac{1}{3}$ larger ρ_0 (center) and 5% larger frequency (right). Other configurations are the same as in the modeling of the frozen mode.

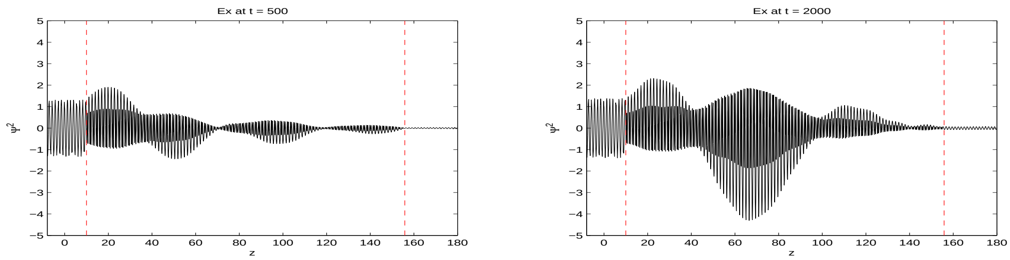

Figure 3.8: Electric field along x direction of the oblique frozen mode at T=500 (left), T=2000 (right bottom). N: Number of grid points per each cell = 16. Δt=0.02, Number of cell=100. TM polarization. The dotted lines indicate the outer boundaries of the layer.

frozen mode, although the shape of the wave and value of the field amplitude are quite different. At T=500.0, the highest amplification of the field amplitude is around 5.9 which is much smaller than that of the magnetic frozen mode where it was exceeding 90. The average group velocity inside the layer is approximately 0.03c, which is significantly faster than the magnetic case (0.0015c). Different from the magnetic frozen mode, the average signal velocity is 0.03c, which is the same as the average group velocity for the oblique frozen mode.

The energy density flux is similar to that of the magnetic froze mode. However, since the larger energy density flux leaves the layer, the energy density is much smaller, e.g., the energy density flux out of the last cell of gyrotropic photonic crystal is around 10^{-3}, but that of oblique anisotropic layer is around 10^{-2}, 10

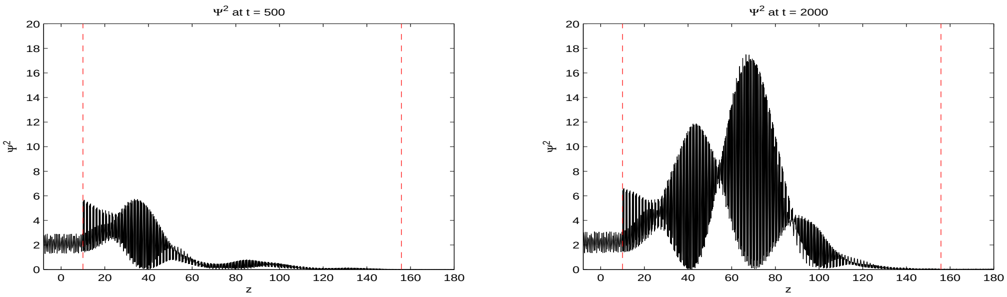

Figure 3.9: Field amplitude $|\Psi|^2$ of the oblique frozen mode at T=500 (left), T=2000 (right). N=16, Number of cell=100. TM polarization. The dotted lines indicate the outer boundaries of the slab.

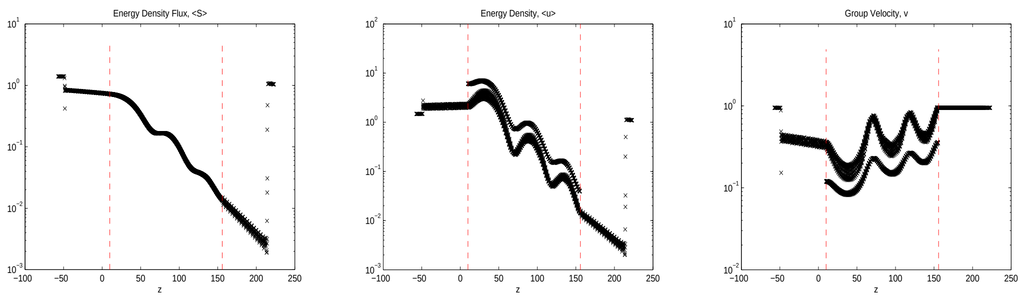

Figure 3.10: Energy density flux (left), Energy density (center), group velocity (right) at the frozen mode frequency in the oblique crystal. T=2000.0. The energy density is higher in anisotropic material than in vacuum. T=500.0. TM polarization. The dotted lines indicate the outer boundaries of the layer .

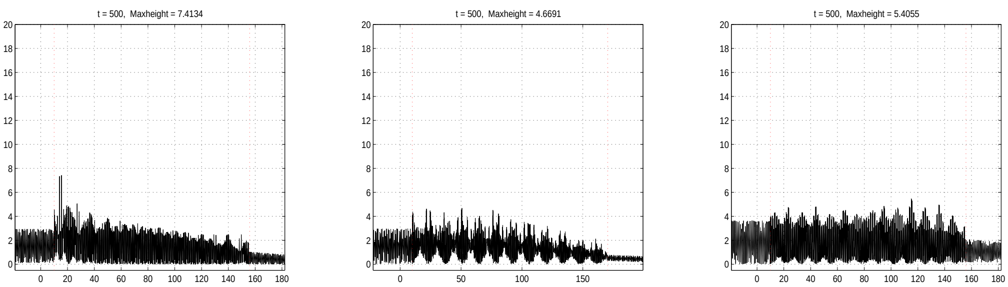

Figure 3.11: Field amplitude $|\Psi|^2$ at T=500 when the direction of the wave is backward (left), the frequency is 10% larger (middle) than the center frequency, and the angle of incidence is 10% larger (right). N=16. TM polarization. The dotted lines indicate the outer boundaries of the layer

times larger. Thus, the group velocity of the wave is much faster than that of the wave in the gyrotropic photonic crystals. Similar to the magnetic crystal, changes in direction of propagation or frequency dramatically alter the behavior of the frozen mode as illustrated in Fig. 3.11.

3.4.2 Modeling with small number of unit cells

The existence of the frozen mode is theoretically based on the assumption that the layer is semi-infinite, but less is known about the phenomena for crystals with a finite small number of unit cells. In this section, we first determine the smallest number of unit cells required for the frozen mode, then study how the finiteness of layer changes the features of the frozen mode.

3.4.2.1 Compressibility condition

If we take a careful look at the phenomena, we note that the phenomena can be characterized by the compressibility of the electromagnetic waves. In other words, the energy density flux ($\mathbf{e}_f$) should satisfy the following compressibility condition for the occurrence of the frozen mode.

$$\int_S \mathbf{e}_f \cdot n ds = \int_V \nabla \mathbf{e}_f dV > 0$$

If the above integral is zero, no energy density stacks up inside the layer as what enters the crystal also leaves it. However, if the integral is positive, the amount of the influx wave is larger than that of outflow wave and consequently energy stacks up inside the layer and gets compressed, reflecting a slow-down of the wave and sharp increase of the field amplitude. This compressibility condition is thus a measure of the energy density flux for the frozen mode. If a layer is finite, the compressibility condition holds only for a finite time T_c, but it is significantly longer than time T_0 when a wave propagates and reaches the same distance in the similar material without showing the frozen mode.

In a one-dimensional finite case, we have only two fluxes, inflow and outflow in z direction. Thus, the compressibility condition can be simply expressed as

$$e_f|_{z_{in}} - e_f|_{z_{out}} > 0, \qquad \text{while} \;\; t < T_c, \qquad T_c \gg T_0$$

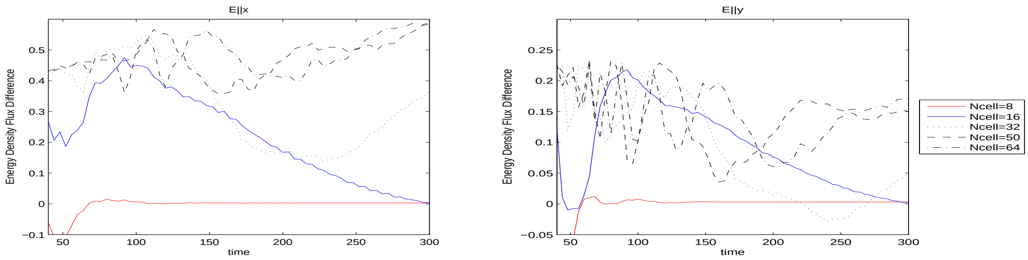

Figure 3.12: The magnetic frozen mode for $E||x$ polarization (left), $E||y$ polarization (right): EDFD vs. number of cells (Ncell). Ncell=8 (solid low flat line), Ncell=16 (decreasing solid line), Ncell=32 (dotted line), Ncell=50 (dashed line), Ncell=64 (dotted-dashed lines). T=300.0.

If we refer to the left quantity as *Energy Density Flux difference(EDFD)*, it is clear that as this EDFD gets larger, this reflects more distinctive features of the frozen mode inside the layer.

3.4.2.2 How many cells are needed for the phenomena?

Fig. 3.12 shows EDFD of the magnetic frozen mode for various numbers of unit cells. With 8 unit cells, we hardly see any significant values of EDFD, reflecting an inability to sustain the frozen mode. However, with only 16 unit cells, the EDFD reaches around 0.5 and linearly decreases to zero up to T=300.0. For 32, 50, or 64 unit cells, we observe a relatively high EDFD, although all eventually approaches to zero after a long time integration. Thus, it appears that approximately 16 unit cells are sufficient for the magnetic frozen mode. The field amplitude, energy density flux, and group velocity with 16 unit cells at T=150 are shown in Fig. 3.13 where we recognize the characteristics of the phenomena, although the intensity is rather small.

In Fig. 3.14, we show EDFDs for various numbers of unit cells in the oblique anisotropic layers. We notice that at least 32 cells are required for a distinctive frozen mode, i.e., twice as many as the number of the magnetic frozen mode. Also, the field amplitude, energy density flux, and group velocity with 32 unit cells at T=150 are shown in Fig. 3.15.

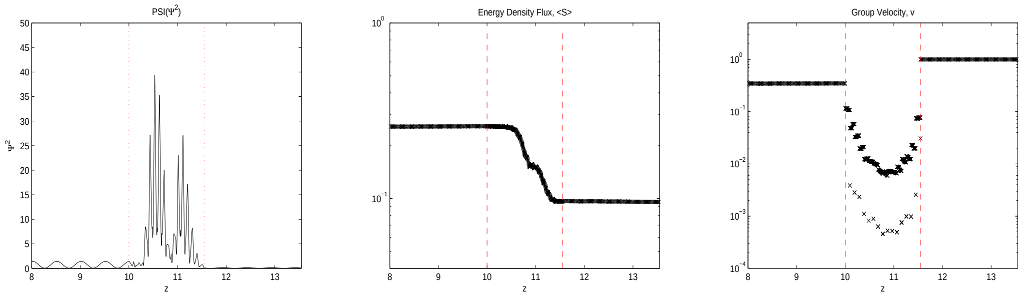

Figure 3.13: The magnetic frozen mode with 16 unit cells: Field amplitude $|\Psi|^2$ (left), energy density flux (center), and group velocity (right) at T=150. The incident wave is E$\|$x polarized.

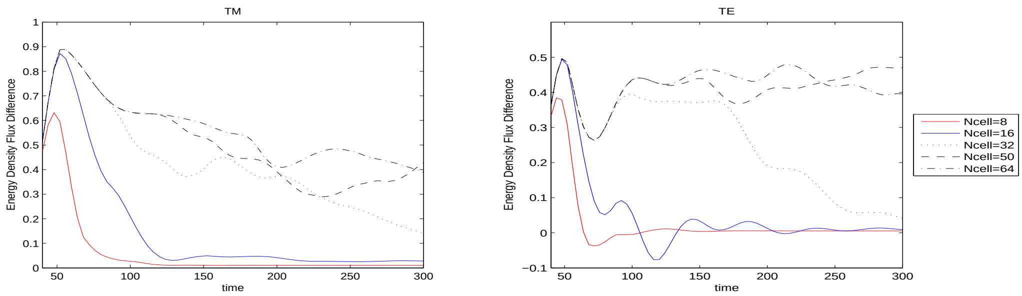

Figure 3.14: The oblique frozen mode for each polarizations at T=300.0. TM polarization (left), TE polarization (right): Ncell=8 (lowest solid line), Ncell=16 (second lowest solid line), Ncell=32 (dotted line), Ncell=50 (dashed line), Ncell=64 (dotted-dashed lines).

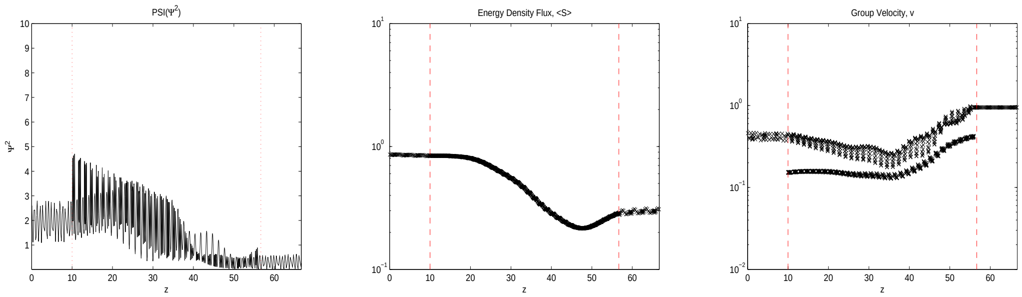

Figure 3.15: The oblique frozen mode with 32 unit cells: Field amplitude $|\Psi|^2$ (left), Energy density (center), and group velocity (right) at T=150. The incident wave is TM polarized.

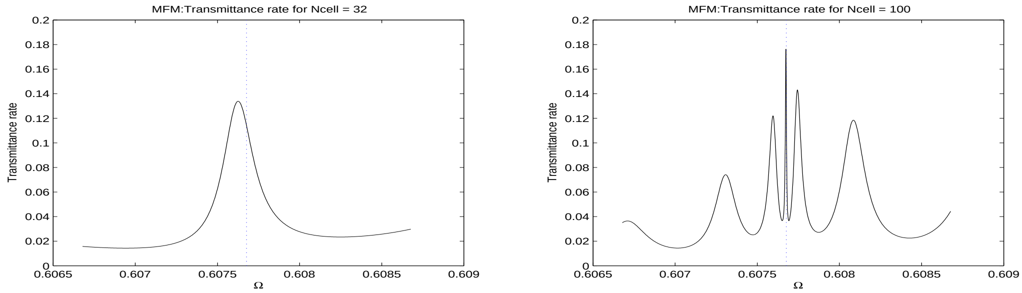

Figure 3.16: Predicted transmittance rate for a finite number of cells = 32 (left), 100 (right). The dotted line denotes the frozen mode frequency. The difference between the frozen mode frequency and the peak is 5×10^{-5} for 32 unit cells, 1×2^{-6} for 100 unit cells.

3.4.2.3 Transmittance rate

Even with a small number of unit cells, we observe that there are still amplifications of the field amplitude and slow-down of waves. What happens, however, with the transmittance rate?

In the paper [9], it is shown that the transmittance rate displays its cup-like singularity at the frozen mode frequency ω_0 when the layer is infinite. On the other hand, when the layer consists of finite number of unit cells, the singularity shifts a little bit from ω_0, but as the number of unit cells increases, the singularity approaches to ω_0 as shown in Fig. 3.16.

Fig. 3.17 shows the computed values of the transmittance rate in the time domain for two different polarization $E||x$ and $E||y$ of the magnetic crystal with 16 unit cells. As predicted, there are shifts of the peak of the transmittance rate curve by the difference of 0.0912 and 0.0304 for $E||x$, $E||y$ respectively. However, we also observe highly oscillatory transmittance rates for both polarizations due to the finiteness of the slab and recognize them as the Fabry-Pérot peaks.

For the oblique frozen mode with 32 unit cells, there are also shifts of the peak by 0.0458, 0.0367 for TM and TE polarization, as illustrated in Fig. 3.18, but no Fabry-Pérot peaks are observed.

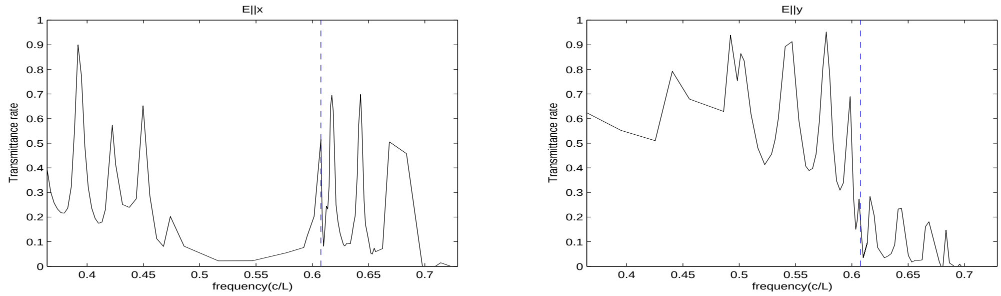

Figure 3.17: Computed values of the transmittance rate for the magnetic frozen mode with 16 unit cells for each polarization E‖x (left), E‖y (right). The lowest peak for E‖x is at 0.6988 with 0.0912 difference and the highest peak for E‖y is at 0.5773 with 0.0304 difference.

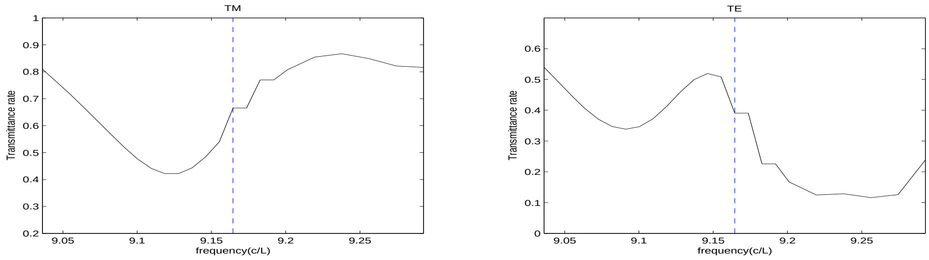

Figure 3.18: Computed values of transmittance rate for the oblique frozen mode with 32 unit cells for each polarization TM (left), TE (right). The lowest peak of TM polarization is at 9.1186 with 0.0458 difference and the highest peak of TE polarization is at 9.1278 with 0.0367 difference.

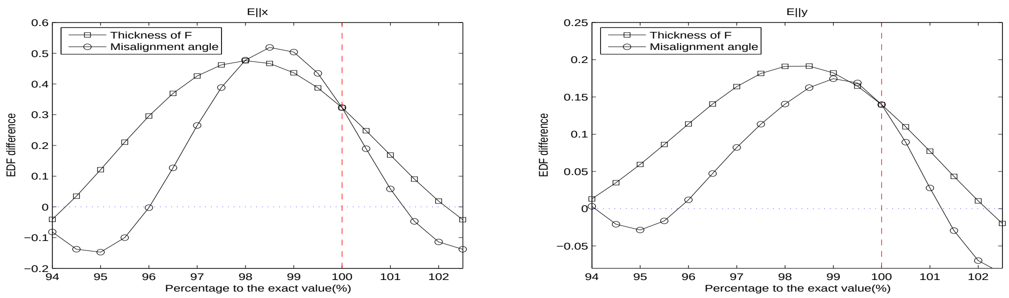

Figure 3.19: EDFD of the magnetic frozen mode for the thickness of **F** layer (square) and the misalignment of **A** layer (circle). The vertical line is the percentage value of parameters for the frozen mode. E‖x (left), E‖ y (right). T=150.0.

3.5 Sensitivity of frozen mode

As we have seen in the previous section, the frozen mode phenomenon, predicted under ideal and impractical assumptions, appears to also exist under more realistic conditions such as finite length crystals. However, the results also emphasize that changes in the various parameters such as frequency or layer length could destroy the phenomenon. In fact, the material properties of layers (thickness of each layer, misalignment angle for anisotropic layer, material constants) and characteristics of wave propagation(incident angle, frequency) should be exact up to 3∼4 digits to generate a stationary inflection point obtained by analytic methods. However, even with current state-of-the-art technology, it seems to be very hard to meet such standards. Thus, it is very likely one faces some errors in the fabrication of the crystal layers and in propagating an electromagnetic wave with the exact frequency.

In this section, we study how such errors in the parameters of the layers or illuminating wave will impact the frozen mode with the goal of providing guidelines on how much error is allowable without destroying the frozen mode. For this purpose, we perform two different tests: One is to observe EDFD for the same amount of errors in each parameters and the other is to observe the independently randomized errors on each parameters within a certain range. The former represents a systematic error while the latter reflects randomized errors during fabrication or operation. The thickness of the magnetic layer **F** and the misalignment of the anisotropic **A** layers are considered in the magnetic frozen mode, while the thickness of the anisotropic **A** layer and the incident angle of the wave are used for the oblique frozen mode.(see Fig. 3.2)

3.5.1 Correlated uncertainty

In Fig. 3.19, we show EDFD for variations in the thickness of **F** layer or different misalignment angle of **A** layer for each polarization E$\|$x(left) and E$\|$y(right). We observe that the maximum of EDFD is shifted from 100 % to a value around 98% $\sim$ 99% of the frozen mode frequency due to the finiteness of the layer. If we set 25% of the maximum of EDFD as the limit of EDFD for the frozen mode, then an allowable error is [95.5, 101.0] for the thickness of the **F** layer and [96.5, 100.5] for the misalignment angle. This analysis indicates that the misalignment

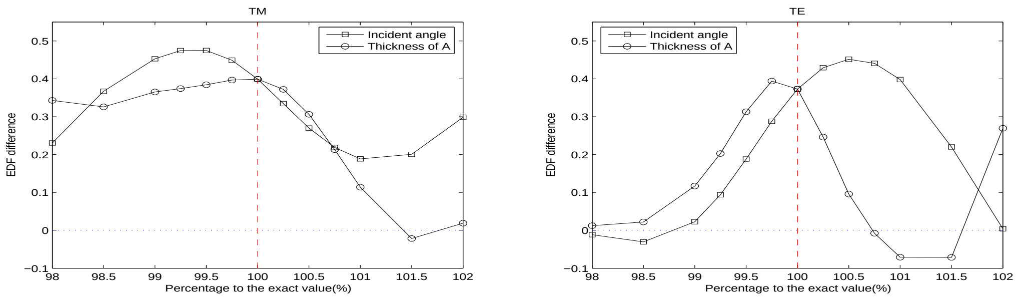

Figure 3.20: EDFD of the oblique frozen mode for the incident angle of the wave(square) and the thickness of **A** layer(circle) at T=150.0. The horizontal line is the percentage value of parameters for the frozen mode and the dotted vertical line is the exact frozen frequency. TM (left), TE (right).

angle of **A** layer is a little more sensitive than the thickness of **F** layer.

For the oblique frozen mode, EDFD for TE polarization is similar to that of the magnetic frozen mode, but EDFD for TM seems to be unexpected as shown in Fig. 3.20. As mentioned in the previous section, the energy density in the oblique anisotropic layer is not sufficiently large since the energy density flux leaving out of the slab remains significant even at the frozen mode frequency. For TE polarization, as the frequency of the incident wave approaches to the frozen mode frequency, the transmittance rate increases and the energy density flux leaving out of the layer decreases. Consequently, EDFD increases as we see on the right of Fig. 3.20. On the other hand, for TM polarization, as we approach to the frozen mode, the energy flux leaving out of the layer decreases, but the transmittance rate also decreases. Thus, EDFD doesn't drop sharply even though it is not in the frozen mode. However, it is still true that energy flux density leaving out of the layer is the smallest at the frozen mode frequency for both polarizations. For this reason, let's only consider TE polarization for the analysis.

Similar to the magnetic frozen mode, there are shifts of the maximum of the EDFD and the allowable error with the same cutoff as for the magnetic frozen mode is [99.0, 100.5] for the incident angle of the wave and [99.5, 101.5] for the thickness of **A** layer, which is significantly smaller than that of the magnetic frozen mode which appears as a much more robust phenomenon.

3.5.2 Uncorrelated uncertainty

In this section, we assume that each parameter in the crystal can vary independently and has own i.i.d. random variable within a given uncertainty associated, which implies we shall study the expectation and what amount of uncertainty will be sufficient to destroy the frozen mode.

First, we let the parameter be the incident angle of the wave. We have one input(incident angle) and one output(EDFD). Using Gauss quadrature, we obtain the expectation as follows:

$$\bar{\mathbf{E}}(n) = \int \mathrm{EDFD}(n, z)\rho(z)dz = \sum_{k=1}^{M} \mathrm{EDFD}(n, z_k)\omega_k$$

assuming that the random variables are uniformly distributed. Here, z_k is the Legendre-Gauss-Lobatto point and ω_k the weight. But, for other parameters, we need different ways of estimation. Let the number of cells for the magnetic frozen mode and the oblique frozen mode be 16 and 32, respectively. Then, we have 32 input parameters for the thickness of **A** layer for the oblique frozen mode and 16 input parameters for the thickness of **F** layer and the misalignment of **A** layer for the magnetic frozen mode. Several numerical methods can be applied to these problems, such as Monte Carlo Method and Stochastic Galerkin Method, but we use Stochastic collocation method which combines the accuracy of the Stochastic Galerkin Method and easy implementation of Monte Carlo Method [34]. We use Stroud's cubature points of degree 2 as collocation points which provide high efficiency with minimal (Ncell+1) number of nodal point sets [27]. The brief procedure takes the following steps:

1. Generate i.i.d. random variables according to Stroud-2 method

   $$Y_k^{2r-1} = \sqrt{\frac{2}{3}}\cos\frac{2rk\pi}{N+1}, \qquad Y_k^{2r} = \sqrt{\frac{2}{3}}\sin\frac{2rk\pi}{N+1}, \qquad r = 1, 2, \cdots, [N/2]$$

   where, [N/2] is the greatest integer not exceeding N/2, and if N is odd $Y_k^N = (-1)^k/\sqrt{3}$

2. Solve for each $k = 0, \cdots, \mathrm{Ncell}$ with $\{Y_k^1, \cdots, Y_k^{\mathrm{Ncell}}\}$ and obtain each EDFD

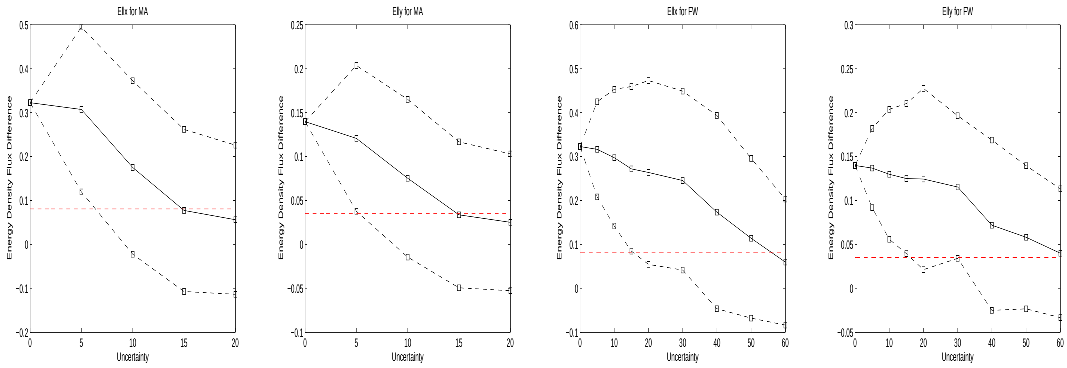

Figure 3.21: The magnetic frozen mode: Expectation for uncorrelated uncertainties of misalignment angle of **A** layer(MA), E$\|$x (1st)/E$\|$y (2nd) and thickness of **F** layer(FW), E$\|$x (3rd)/E$\|$y (4th). The above dotted line is $E(x)$+δ and the below one is $E(x)$-δ. $E(x)$:expectation, δ: is one standard deviation. The horizontal dashed line is a cutoff amount of EDFD for the frozen mode.

3. Post-process the result to evaluate the expectation

$$\mathbf{E} = \frac{1}{\mathrm{Ncell}+1}\sum_{k=0}^{\mathrm{Ncell}} \mathrm{EDFD}(k)$$

For the magnetic frozen mode, Fig. 3.21 shows that if we allow one standard deviation of uncertainty, then approximately 5 % uncertainty in the misalignment angle of **A** layers and as much as 15 % uncertainty of thickness of **F** layer are allowable without the EDFD being reduced below 25 % maximum value. These numbers are 2 $\sim$ 5 times larger than those for the correlated uncertainty, reflecting significant robustness of the magnetic crystal to randomized small uncertainties.

Similarly, for the oblique frozen mode, as shown in Fig. 3.22, the thickness of the **A** layer can vary with about 2% and the incident angle up to 5% to maintain the frozen mode characteristics within one standard deviation. Although these numbers are considerably smaller than those for the magnetic crystal, the numbers are still 2 $\sim$ 10 times larger than those found in the correlated case.

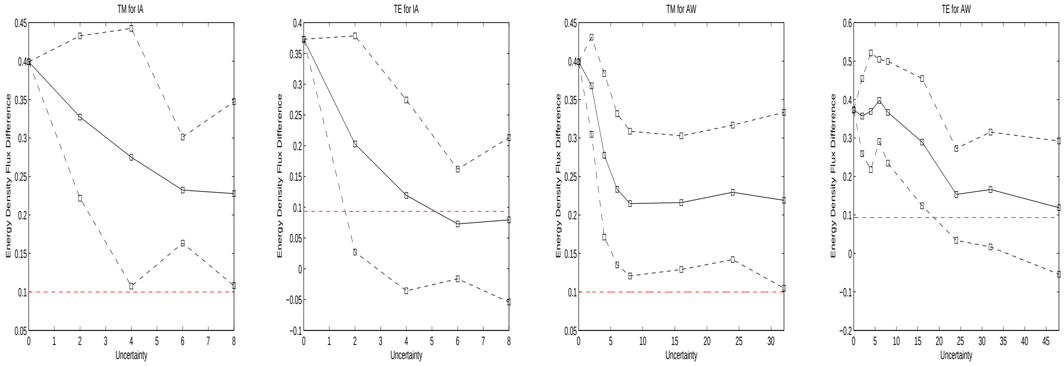

Figure 3.22: The oblique frozen mode: Expectation for uncorrelated uncertainties of the incident angle of the wave (IA), TM (1st)/TE (2nd) and the thickness of **A** layer (AW), TM (3rd)/TE (4th). The above dotted line is $E(x)+\delta$ and the below one is $E(x)$-δ. $E(x)$:expectation, δ:standard deviation. The horizontal dashed line is a cutoff amount of EDFD for the frozen mode.

3.6 Concluding remarks

In this chapter, we addressed a number of central questions regarding the recently proposed periodic structures, utilizing anisotropic materials [8, 9, 10] and expected to display a number of highly unusual and interesting phenomena such as very low propagation velocity, very high localized field intensity and also perfect transmission into crystals comprising of high-index materials.

Our first task has been to develope an accurate and efficient means, by which to model these new crystals in the time-domain with the aim of confirming the predicted behavior and further understanding the nature and limits of the theoretical predictions. We developed and validated a discontinuous Galerkin method for this purpose. As we have seen before, we are able to qualitatively and quantitatively confirm all essential predictions and further show that many of these effects can be reproduced in crystals with even moderate length.

As predicted by the theory, the finiteness of the crystal implies a slight shift in the frozen mode frequency. Furthermore, we have compared the behavior of crystals with magnetic layers as well as purely dielectric crystals with the incident wave entering at an oblique angle. While the behaviors of the two crystals are qualitatively comparable, the details are very different and the magnetic material leads to much stronger effects. Indeed, the computational results show that the amplification of the oblique frozen mode is more than 20 times lower than that of the magnetic frozen mode and the velocity of energy transfer of the oblique frozen mode is also approximately 20 times faster than that of the magnetic frozen mode. Hence, the purely dielectric crystal has to be longer to achieve similar effects. Unfortunately, even the very thin magnetic layers are problematic from a production perspective as magnetic materials with sufficient Faraday rotation and low enough loss is difficult to manufacture in the right frequency regime (microwaves).

By studying the sensitivity of the frozen mode phenomenon, we have been able to establish bounds for how large uncertainties can be without impacting the essential behavior of the crystals. These studies also confirm that the magnetic crystals are considerably more stable to variations in the crystal parameters as compared to the oblique crystal. Surprisingly, we find in both cases that systematic variations are considerably worse than uncorrelated variations in the parameters, confirming that the frozen mode phenomenon is a robust phenomenon with excellent chances of being verified experimentally, provided appropriate materials can be identified.

Chapter 4

Optimization and design of frozen mode crystals

In this chapter, we explore the use of PDE constrained nonlinear optimization techniques to optimize and design electromagnetic crystals which exhibit frozen mode behavior. This is characterized by the association with Van Hove singularities in the dispersion relation, e.g., stationary reflection points and degenerate band edge points. Hence, the optimization process modifies the dispersion relation by adjusting the geometries and material parameters. The resulting algorithm is found to be capable of recovering all known crystal configurations as well as many new configurations, some of which display dramatically improved properties over previously used configuration. We investigate both gyrotropic photonic crystals and degenerate band edge crystals as well as the more complex case of the oblique incidence where we extend the investigation to the three-dimensional case to identify the first three-dimensional crystal exhibiting frozen mode behavior.

4.1 Introduction

Controlling the flow of electromagnetic waves in materials has been the frontier of our technologies in the last decade. Along with prohibiting wave propagation or localizing wave in certain areas, decreasing the speed of waves with a significant rate has grabbed broad attentions. Recent studies of periodic structures of several different anisotripic materials show that when a monochromatic wave with a certain frequency propagates in such structures, it shows abnormal electromagnetic phenomena such as dramatic slow-down of the wave, the significant increase of field amplitude and singularities of the trasmittance rate, which are classified as the frozen mode. These unique features of the frozen mode are attractive for numerous practical applications and recent studies [6] have confirmed the robustness of these phonomena. In the beginning, the frozen mode was regarded as a distinctive phenomenon only related to stationary inflection points of the dispersion relations $\omega(k)$ such as,

$$\frac{\partial \omega}{\partial k} = 0; \qquad \frac{\partial^2 \omega}{\partial k^2} = 0; \qquad \frac{\partial^3 \omega}{\partial k^3} \neq 0 \quad \text{at} \;\; \omega = \omega_0$$

However, it is worth mentioning that these properties of the dispersion relation are special cases of what are known as Van Hove singularities [20] as points where the first derivative of the dispersion relation $\omega(k)$ vanishes, i.e.,

$$\frac{\partial \omega}{\partial k} = 0, \qquad \text{at} \;\; \omega = \omega_0$$

This nomenclature is related to density of state (DOS), since it is well-known that DOS is inversely proportional to $\partial\omega/\partial k$ [21].

However, all previous studies have focused on the analysis of crystal configurations found by a trial-and-error technique which tends to limit the number of parameters one can freely vary. This limits the flexibility in the design of such crystals and leaves an open question of whether it is generally possible to achieve the sought-after properties in the dispersion relation, e.g., when given some specific materials, one can modify the geometric properties of the crystal as needed.

To address this problem in a more systematic way, we consider the implementatioin of a PDE constrained optimization approach where we use the dispersion relation, given by the transfer matrix method or by solving the Maxwell eigenproblem, in combination with the algorithm of Method of Moving Asymptote (MMA) [28, 29, 30, 36, 37] to recreate and to optimize known configurations as well as to design entire crystal arrangements.

In this study, we consider the optimization and the design of three different types of crystals all of which exhibit the frozen mode phenomena. The first one is a gyrotropic photonic crystal consisting of two misaligned anisotropic layers and one magnetic layer. Its dispersion relation has a stationary inflection point ω_0 on the 2nd band. The second class of crystals consists of two misaligned anisotropic layers and vacuum between them. Its dispersion relation has a degenerate band edge ω_d in the first band. The final structure consists of only one anisotropic layer with $\varepsilon_{xz} \neq 0$ and vacuum between them. However, the frozen mode phenomenon only emerges when the incident wave propagates into this layer at an oblique angle. This latter case is quite different from the previous two cases. The dispersion relation where a stationary inflection point ω_0 lies was originally computed by a one-dimensional transfer matrix method with the assumption of tangential consistency of wave vector. To verify the existence of a stationary inflection point in general three dimensional setting which was previously unascertained, we first solve the general Maxwell eigenproblem to get the dispersion relation with initial parameter sets and apply the optimization techniques to seek a stationary inflection point in the dispersion relation of three dimension.

The remaining part of this chapter is organized as follows. In section. 4.2, we briefly recall the physical model, Maxwell's equations and how one recovers the dispersion relation from these equations. This sets the stage for section. 4.2 where we explain the implementation of the optimization method based on Method of Moving Asymptote (MMA). In sections 4.3 and 4.4, we display the methods and results of optimizing the magnetic frozen mode and degenerate band edge for previously known designs as well as new configurations, respectively. Section 4.5 is devoted to the design of crystals for the oblique case and its modeling in the time domain. We conclude with a few remarks and future works in section. 4.6.

4.2 Physical model

We consider Maxwell's equations

$$\nabla \times \tilde{\mathbf{E}} = -\frac{d\tilde{\mathbf{B}}}{dt}, \qquad \nabla \times \tilde{\mathbf{H}} = \frac{d\tilde{\mathbf{D}}}{dt}$$

where $\tilde{\mathbf{E}}$ and $\tilde{\mathbf{H}}$ is the electric field and magnetic field, respectively, $\tilde{\mathbf{D}}$ and $\tilde{\mathbf{B}}$ the displacement field and the induction field. These fields are related by linear constitutive relations as follows.

$$\tilde{\mathbf{D}}(z) = \hat{\varepsilon}(z)\tilde{\mathbf{E}}(z), \qquad \tilde{\mathbf{B}}(z) = \hat{\mu}(z)\tilde{\mathbf{H}}(z)$$

where we have assumed that $(\hat{\varepsilon}, \hat{\mu})$ are homogeneous in the (x, y)-plane. If we consider harmonic solutions with frequency ω, we recover the Maxwell's equations in the frequency domain.

$$\nabla \times \tilde{\mathbf{E}} = i\omega\hat{\mu}(z)\tilde{\mathbf{H}} \;\; , \;\; \nabla \times \tilde{\mathbf{H}} = -i\omega\hat{\varepsilon}(z)\tilde{\mathbf{E}} \tag{4.1}$$

To simplify the above equations, we introduce the normalized quantities using

$$z = \frac{\tilde{z}}{\tilde{L}}, \quad t = \frac{\tilde{t}}{\tilde{L}/\tilde{c_0}}$$

where, $\tilde{L}$ is a reference length and $\tilde{c_0} = (\tilde{\varepsilon}_0\tilde{\mu}_0)^{-\frac{1}{2}}$ is the dimensional speed of light in vacuum. Also, $\tilde{\mathbf{E}}$ and $\tilde{\mathbf{H}}$ are normalized as

$$\mathbf{E} = \sqrt{\frac{\tilde{\varepsilon_0}}{\tilde{\mu_0}}}\frac{\tilde{\mathbf{E}}}{\tilde{H}_0}, \qquad \mathbf{H} = \frac{\tilde{\mathbf{H}}}{\tilde{H}_0}$$

where $\tilde{H}_0$ is a dimensional reference magnetic field strength. By substituting these normalized quantities into Eq. (4.1), we obtain the following non-dimensionalized equations

$$\nabla \times \mathbf{E} = i\omega\hat{\mu}(z)\mathbf{H} \;\; , \;\; \nabla \times \mathbf{H} = -i\omega\hat{\varepsilon}(z)\mathbf{E}$$

where $(\hat{\varepsilon}, \hat{\mu})$ now represent the relative permittivity and permeability, respectively.

Let's assume the solution is periodic with the following form

$$\begin{bmatrix} \vec{E}(\vec{x}) \\ \vec{H}(\vec{x}) \end{bmatrix} = \begin{bmatrix} \vec{E}_k \\ \vec{H}_k \end{bmatrix} \exp(i\vec{k}\cdot\vec{x}) \;\; , \qquad \vec{k} = \text{wave vector}$$

Then, we recover the modal equation

$$(\nabla + i\vec{k}) \times \mathbf{E}_k = i\omega\hat{\mu}(z)\mathbf{H}_k \;\; , \qquad (\nabla + i\vec{k}) \times \mathbf{H}_k = -i\omega\hat{\varepsilon}(z)\mathbf{E}_k$$

which simplifies as

$$(\nabla + i\vec{k}) \times \frac{1}{\hat{\mu}(z)}(\nabla + i\vec{k}) \times \mathbf{E}_k = \omega^2\hat{\varepsilon}(z)\mathbf{E}_k$$

For a given value of the wave vector $\vec{k}$, the above problem is recognized as an eigenvalue problem for $(\omega^2, \mathbf{E}_k)$, from which we recover the dispersion relation $(\vec{k}, \omega(\vec{k}))$.

Hence, when optimizing the crystals, we must ensure that all considered solutions satisfy the above eigenvalue problem which emerges as the constraints in the optimization process.

The goal of the optimization is to identify one type of Van Hove singularities [20] in the dispersion relation, leading to a very strong divergence of the density of states(DOS) near the corresponding frequency. There are several types of singularities, but we are specially interested in finding singularities where the first and second derivative are both zero, i.e.

$$\frac{\partial \omega}{\partial k} = 0, \quad \frac{\partial^2 \omega}{\partial k^2} = 0, \qquad \text{at } \ \omega = \omega_0$$

We state this equivalently as the following minimization problem.

$$\begin{aligned} \text{minimize} \qquad & \lambda \left| \frac{d\omega}{dk}(\vec{x}) \right| + \left| \frac{d^2\omega}{dk^2}(\vec{x}) \right|, \qquad \text{at } \ \vec{k} = \vec{k}_0 \\ & x_j^{min} \le x_j \le x_j^{max}, \qquad 1 \le j \le n, \quad \text{n} \ = \ \text{number of variables} \end{aligned} \tag{4.2}$$

where $\vec{x}$ is a n-variable vector and $|\cdot|$ means the absolute value of the scalar $\frac{d\omega}{dk}$, $\frac{d^2\omega}{dk^2}$. Also, note that λ is a weight constant which is dependent on the type of singularities. The objective function $\frac{d\omega}{dk}(\vec{x})$ and $\frac{d^2\omega}{dk^2}(\vec{x})$ can be obtained directly from the dispersion relation with optimization variable $\vec{x}$ by solving the eigenvalue problem discussed above. Once the dispersion relation is obtained, the derivatives of the objective functions can be computed easily. For example, the fourth order approximation of its first and second derivatives are computed by difference approximations such as,

$$\begin{aligned} \frac{d}{dx_j}\left\{\frac{d\omega}{dk}(\vec{x})\right\} &= \frac{1}{12\Delta x_j^p}\left\{-\frac{d\omega_{j+2}^p}{dk} + 8\frac{d\omega_{j+1}^p}{dk} - 8\frac{d\omega_{j-1}^p}{dk} + \frac{d\omega_{j-2}^p}{dk}\right\} \\ \frac{d^2}{dx_j^2}\left\{\frac{d\omega}{dk}(\vec{x})\right\} &= \frac{1}{12(\Delta x_j^p)^2}\left\{-\frac{d\omega_{j+2}^p}{dk} + 16\frac{d\omega_{j+1}^p}{dk} - 30\frac{d\omega_j^p}{dk} + 16\frac{d\omega_{j-1}^p}{dk} - \frac{d\omega_{j-2}^p}{dk}\right\} \\ & \text{where } \ \frac{d\omega_j^p}{dk} = \frac{d\omega}{dk}(\vec{x}_j + p\Delta\vec{x}_j), \quad 1 \le j \le n \end{aligned}$$

In fact, this fourth order approximation is preferred in the computation of the derivatives to increase the accuracy and to make the fast convergence. Furthermore, it is required to obtain an initial guess $\vec{k}_0$ or at least a group of possible candidates of $\vec{k}_0$s. Identifying suitable $\vec{k}_0$ is one of most critical and significant factors of convergence of the optimization solution. We have identified that the following approach is working well.

1. Divide the dispersion relation into several sections such that each section contains only one wave vector with $|\frac{d\omega^p}{dk}(\vec{x})| < \varepsilon \ll 1$.

2. For each section, find one wave vector $\vec{k}_0$ such that

$$D_{12}(\vec{k}_0) = \min_p \left| \sum_{\ell=p-2}^{p+2} \frac{d\omega^p}{dk}(\vec{k}_\ell) \right| , \qquad p \in \text{section } I \tag{4.3}$$

   Note that the function inside the bars is a way of indicating the amount of the first and the second derivative at the same time

3. Optimize the objective function at $\vec{k}_0$.

Since the objective function is generally not convex, we use the algorithm of Method of Moving Asymptote (MMA). The application of MMA to find singularity points of dispersion relation can be stated briefly as follows. First, Eq. (2.2) can be changed into the following equivalent problem.

$$\begin{aligned}
\text{minimize} \qquad & f_0(x) = z + \sum_{i=1}^{4} c_i y_i \qquad\qquad (4.4)\\
\text{subject to} \qquad & f_1(x) = \lambda \frac{d\omega}{dk}(\vec{x}) - y_1 \leq 0, \quad f_2(x) = \frac{d^2\omega}{dk^2}(\vec{x}) - y_2 \leq 0 \\
& f_3(x) = -\lambda \frac{d\omega}{dk}(\vec{x}) - y_3 \leq 0, \quad f_4(x) = -\frac{d^2\omega}{dk^2}(\vec{x}) - y_4 \leq 0 \\
& z \geq 0, \quad y_i \geq 0, \quad 1 \leq i \leq 4, \\
& x_j^{min} \leq x_j \leq x_j^{max}, \qquad 1 \leq j \leq n
\end{aligned}$$

where, $y_1, \cdots, y_n$ and z are artificial optimization variables. Note that z is zero and y_i is given as the maximum of each constraint function at the optimized solution $\vec{x}$. Now, we have the non-linear optimization problem with several constraints. For these $f_i(\vec{x})$s, let's define $g_i(x)$ in the following way,

$$\begin{aligned}
g_i(x) &= r_i + \sum_{j=1}^{n}(\frac{p_{ij}}{U_j - x_j} + \frac{q_{ij}}{x_j - L_j}) \qquad (4.5)\\
p_{ij} &= \max\{0, (U_j - x_j)^2 \frac{\partial f_i}{\partial x_j}\}, \quad q_{ij} = \max\{0, -(x_j - L_j)^2 \frac{\partial f_i}{\partial x_j}\}\\
r_i &= f_i(x) - \sum_{j=1}^{n}(\frac{p_{ij}}{U_j - x_j} + \frac{q_{ij}}{x_j - L_j}), \quad 1 \le i \le 4, \quad 1 \le j \le n
\end{aligned}$$

The parameters L_j and U_j (known as *moving asymptotes*) are chosen as $L_j < x_j < U_j$ and play a critical role in the convergence of the optimization scheme. In fact, L_j and U_j are adjusted for each iteration according to the convergence of the solution. Note that the second derivatives of g_i are given as

$$\frac{\partial^2 g_i}{\partial x_j x_\ell} = \delta_{j\ell}\left(\frac{2p_{ij}}{(U_j - x_j)^3} + \frac{2q_{ij}}{(x_j - L_j)^3}\right), \quad 1 \le j, \ell \le n$$

Since $p_{ij} \ge 0,\ q_{ij} \ge 0$, g_i is a convex function. In fact, as long as L_j and U_j are finite, g_i is strictly convex in all variables except for $\frac{\partial g_i}{\partial x_j}(x) = 0,\ 1 \le j \le n$. With g_is as shown in the Eq. (4.5), we have the following subproblem.

$$\begin{aligned}
P : \text{minimize} \quad & \sum_{j=1}^{n}\left(\frac{p_{ij}}{U_j - x_j} + \frac{q_{ij}}{x_j - L_j}\right) + r_0 \qquad (4.6)\\
\text{subject to} \quad & \left(\frac{p_{ij}}{U_j - x_j} + \frac{q_{ij}}{x_j - L_j}\right) + r_i \le f_i, \quad 1 \le i \le 4\\
& x_j^{min} \le x_j \le x_j^{max}, \qquad 1 \le j \le n
\end{aligned}$$

Then, the Lagrangian function corresponding to this problem is given by

$$W(x, y) = \vec{r}_0 - \vec{y}^T \vec{r} + \sum_{j=1}^{n}\left(\frac{p_{0j} + \vec{y}^T \vec{p}_j}{U_j - x_j(\vec{y})} + \frac{q_{0j} + \vec{y}^T \vec{q}_j}{x_j(\vec{y}) - L_j}\right)$$

In fact, $W(x, y)$ is differentiable, smooth and concave. Finally, the Lagrangian dual problem with this Lagrangian function is

$$\begin{aligned}
D : \text{maximize} \quad & W(x, y) = \vec{r}_0 - \vec{y}^T \vec{r} + \sum_{j=1}^{n}\left(\frac{p_{0j} + \vec{y}^T \vec{p}_j}{U_j - x_j(\vec{y})} + \frac{q_{0j} + \vec{y}^T \vec{q}_j}{x_j(\vec{y}) - L_j}\right) \quad (4.7)\\
\text{subject to} \quad & y \ge 0
\end{aligned}$$

This yields a nice convex optimization problem and it can be solved by a primal-dual Newton method. The details for this primal-dual method are given in [29]

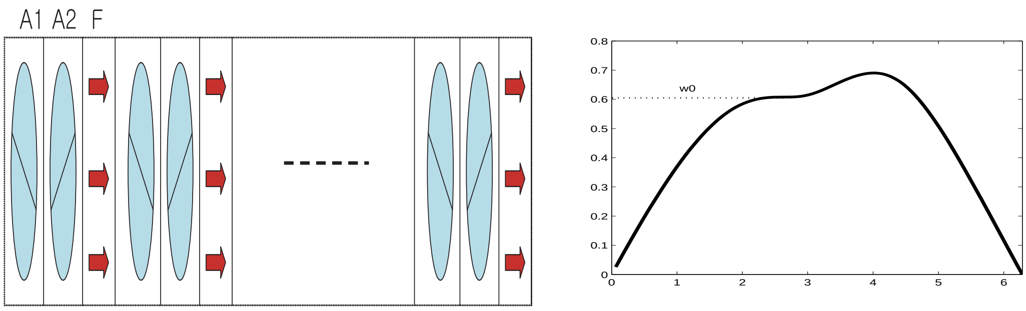

Figure 4.1: Periodic structure of gyrotropic photonic crystals consisting of two different anisotropic materials (A1,A2) with one magnetic layer (F) (left) and its dispersion relation (right).

4.3 Optimization and design of magnetic crystals

The frozen mode in the gyrotropic crystal occurs when a monochromatic wave with frequency ω_0 propagates into a periodic array consisting of two misaligned anisotropic layers and one magnetic layer (Fig. 4.1). In the dispersion relation, this ω_0 is a stationary inflection point with the following properties

$$\frac{\partial \omega}{\partial k} = 0, \quad \frac{\partial^2 \omega}{\partial k^2} = 0, \quad \frac{\partial^3 \omega}{\partial k^3} \neq 0, \qquad \text{at} \quad \omega = \omega_0 \tag{4.8}$$

As shown in [9], one set of parameters resulting in an inflection point at ω_0 is

$$\text{For } \mathbf{A} \text{ layer} : \hat{\varepsilon} = \begin{bmatrix} 13.61 + 12.40\cos(2\phi) & 12.40\sin(2\phi) \\ 12.40\sin(2\phi) & 13.61 - 12.40\cos(2\phi) \end{bmatrix}, \quad \hat{\mu} = \hat{\mathbf{I}}$$

$$\text{For } \mathbf{F} \text{ layer} : \hat{\varepsilon} = \begin{bmatrix} 5.0 & 0.0 \\ 0.0 & 5.0 \end{bmatrix}, \quad \hat{\mu} = \begin{bmatrix} 60.0 & i37.0 \\ -i37.0 & 60.0 \end{bmatrix}$$

$$\phi_1 = 0, \quad \phi_2 = -\pi/4, \ \mathrm{L_F} = 0.0047454, \quad \mathrm{L_A} = 0.5(1.0 - \mathrm{L_F})$$

$$k_0 = 2.6329, \qquad \omega_0 = 0.607676756(c/L)$$

where ϕ_1 and ϕ_2 are the misalignment angle of the first and second anisotropic layer, respectively. Also, L_F is the thickness of **F** layer and L_{A1}, L_{A2} are thickness of the first and second anisotropic layer, respectively.

The first task is to recover this set of parameters by the aforementioned optimization technique and, subsequently, seek sets of parameters if possible. Since the periodicity is along z direction only, the dispersion relation of the magnetic frozen mode can be obtained by the transfer matrix method rather than solving the full Maxwell eigenvalue problem.

The transfer matrix method is a way of finding the dispersion relation from Bloch solutions of Maxwell's equations in planar structures. The transfer matrix ($T_L(\omega)$) can be obtained with bases of tangential components of electrical and magnetic fields. Then, it is used for Bloch solutions of the Maxwell's equations in a periodic media such as

$$q_k(z+L) = e^{ikL} q_k(z), \qquad q_k = [E_x \ E_y \ H_x \ H_y]_k^T$$

Also, using the property of transfer matrix $T_L(\omega)q_k(z) = q_k(z+L)$, we get the following charicteristic equation.

$$(T_L(\omega) - e^{ikL})q_k(L) = 0 \implies \det(T_L(\omega) - e^{ikL}) = 0$$

which yields the dispersion relation between ω and the wave vector k. The transfer matrix of an anisotropic layer with misalignment angle ϕ (T_A) and a magnetic layer (T_F) are given as

$$T_A(\phi, L_A) = W(\phi, L_A)W^{-1}(\phi, 0), \qquad T_F(L_F) = W(L_F)W^{-1}(0)$$

$$W(\phi, L_A) = \begin{bmatrix} (\cos\phi)e^{in_1 a} & (\cos\phi)e^{-in_1 a} & -(\sin\phi)e^{in_2 a} & -(\sin\phi)e^{-in_2 a} \\ (\sin\phi)e^{in_1 a} & (\sin\phi)e^{-in_1 a} & (\cos\phi)e^{in_2 a} & (\cos\phi)e^{-in_2 a} \\ -\eta_1(\sin\phi)e^{in_1 a} & \eta_1(\sin\phi)e^{-in_1 a} & -\eta_2(\cos\phi)e^{in_2 a} & \eta_2(\cos\phi)e^{-in_2 a} \\ \eta_1(\cos\phi)e^{in_1 a} & -\eta_1(\cos\phi)e^{-in_1 a} & -\eta_2(\sin\phi)e^{in_2 a} & \eta_2(\sin\phi)e^{-in_2 a} \end{bmatrix}$$

$$W(L_F) = \begin{bmatrix} e^{in_1 f} & e^{-in_1 f} & -ie^{in_2 f} & -ie^{-in_2 f} \\ -ie^{in_1 f} & -ie^{-in_1 f} & e^{in_2 f} & e^{-in_2 f} \\ i\eta_1 e^{in_1 f} & -i\eta e^{-in_1 f} & -\eta_2 e^{in_2 f} & \eta_2 e^{-in_2 f} \\ \eta_1 e^{in_1 f} & -\eta e^{-in_1 f} & -i\eta_2 e^{in_2 f} & i\eta_2 e^{-in_2 f} \end{bmatrix}$$

where, $a = \frac{\omega}{c}L_A$ and $f = \frac{\omega}{c}L_F$. Then, the transfer matrix of three-cell layer is

$$T_L(\phi 1, \phi 2, L_{A1}, L_{A2}, L_F) = T_F(L_F)T_A(\phi_2, L_{A2})T_A(\phi_1, L_{A1})$$

and the dispersion relation of this layer is obtained by solving

$$\det(T_L - \xi\mathbf{I}) = 0, \quad \xi = e^{ikL}, \quad L = L_{A1} + L_{A2} + L_F \ .$$

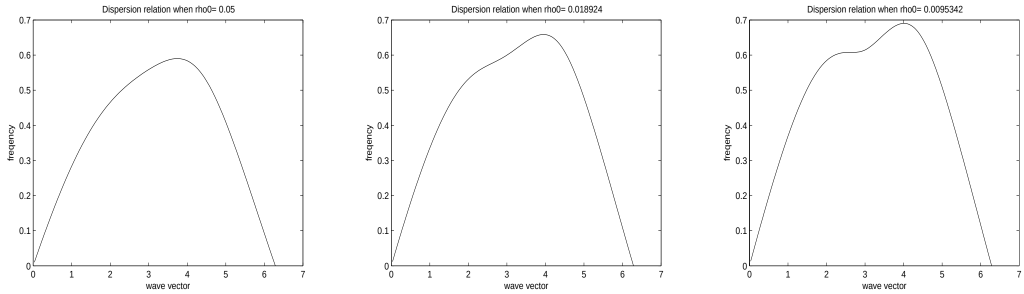

Figure 4.2: Scenes from optimization process with one variable L_F (left to right). Let $\rho_0 = L_A/L_F$. ρ_0=0.05(left), 0.0.018924 (center), 0.0.0095342 (right) after 6 iterations, $\frac{d\omega}{dx}$= 3.97e-13, $\frac{d^2\omega}{dx^2}$= 0.007907 with $\lambda = 10000$.

The left hand side is a fourth order polynomial and we can compute the roots of it by simple root-finding method.

As for choosing wave vector k_0 corresponding to ω_0, we first find the wave vector k_b corresponding to a band edge ω_b(the highest peak such that $\frac{d\omega}{dk}|_{\omega=\omega_b} = 0$) and seek k less than k_b where the minimum of D_{12} occurs as discussed in Eq. (4.3). However, this may still miss the true candidates of wave vector k_0 for optimized solution ω_0. To address this issue, we change the initial values if the converged solution in the sense of $\|x - x_{\text{old}}\| < \varepsilon_0$ does not satisfy

$$\frac{d\omega}{dk} < \varepsilon_1, \quad \frac{d^2\omega}{dk^2} < \varepsilon_2 \qquad\qquad \text{for sufficiently small } \varepsilon_1,\ \varepsilon_2$$

In general, we shall allow the thickness of the magnetic layer (L_F), the thickness of the first anisotropic layer (L_{A1}) and material constants of the anisotropic layer(ε_A, δ_A) to vary during the optimization, although this could be extended as needed. In Fig. 4.2, we show the sequence of convergence of the dispersion relation for a stationary inflection point using optimization with just one variable L_F.

We note that the optimized solution for L_F is accurate up to 5.0e-06 with the analytically derived L_F [9] and the difference is negligible in the sense of sensitivity. Other optimized solutions with different number of variables(n) are shown in Table 4.1. We observe that the thickness of **F** layer is approximately the same for all sets, but the thickness of **A** layer varies depending on the misalignment angle or the material constants. The absolute values of the first and second derivative

		Set1	Set2	Set3	Set4
Input	n	1	2	2	4
	variables	$L_F(L_{A1} = L_{A2})$	L_F, L_{A1}	L_F, L_{A1}	$L_F, L_{A1}, \varepsilon_A, \delta_A$
	ϕ_2	$-\pi/4$	$-\pi/4$	$-\pi/3$	$-\pi/4$
Solution	L_F	0.00474	0.00480	0.00490	0.00470
	L_{A1}	0.49763	0.44555	0.22056	0.45001
	ε_A	5.1	5.1	5.1	5.0
	δ_A	1.1	1.1	1.1	1.18189
	ω_0	0.60769	0.60950	0.67177	0.62171
	k_0	2.63894	2.63894	2.70177	2.63894
	$\frac{d\omega}{dk}\|_{\omega=\omega_0}$	3.9666e-13	2.41590e-16	6.5758e-16	1.80310e-12
	$\frac{d^2\omega}{dk^2}\|_{\omega=\omega_0}$	0.007907	0.00898	0.00917	0.00191
	TR rate	0.3388	0.4081	0.7786	0.3109

Table 4.1: Optimized solutions with different number of variables (n) or different initial values for magnetic frozen mode. ϕ_2=misalignment angle of second anisotropic layer(we let $\phi_1 = 0$). L_F= thickness of magnetic layer, L_{A1}=thickness of the first anisotropic layer. TR (Transmittance) rate = I_T/I_I, $I \equiv \frac{1}{\mu_0} < E \times B >$, $<>$ = time average over a cycle. ε_A and δ_A are used in the permittivity of anisotropic layer as follows.

$$\hat{\varepsilon} = \begin{bmatrix} \varepsilon_A + \delta_A \cos(2\phi) & \delta_A \sin(2\phi) \\ \delta_A \sin(2\phi) & \varepsilon_A - \delta_A \cos(2\phi) \end{bmatrix}.$$

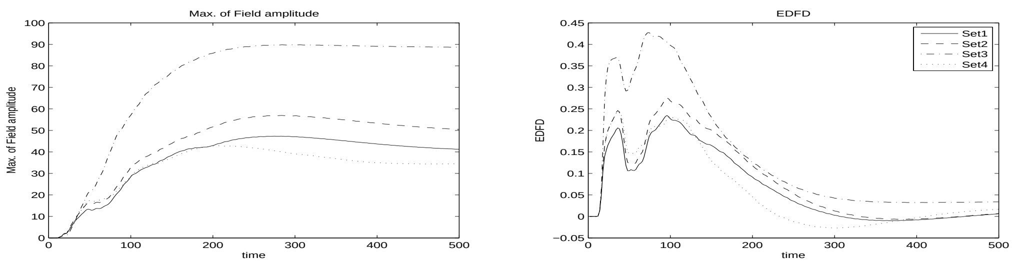

Figure 4.3: Maximum of the field amplitude(left) and the Energy Density flux difference(e_f of the first cell - e_f of the last cell, e_f=energy density flux) (right) for set 1 (solid line), set 2 (dashed line), set 3 (dot-dashed line) and set 4 (dotted line) of Table 4.1. Number of cell = 16. E$\|$x polarization.

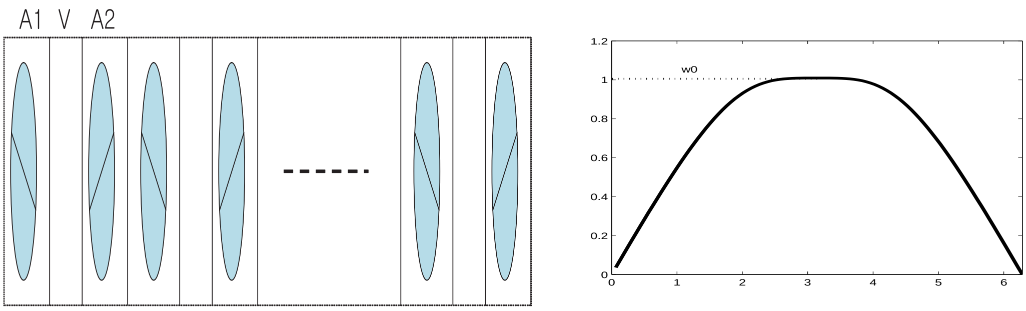

Figure 4.4: Periodic crystal structure allowing a degenerate band edge. The crystal consists of two misaligned anisotropic layers (A1,A2) with vacuum (V) between them (left) and its dispersion relation (right)

at each ω_0 are sufficiently close to zero, so all sets show every characteristics of the frozen mode.

However, the closer to zero the first derivative is, the slower the group velocity (velocity of energy transfer) of the wave is. Also, the intensity of the field amplitude inside the layer and the amount of energy density stacked inside the layer indicated by energy density flux difference (EDFD) [6] are closely related to the transmittance rate. If a larger amount of energy enters into layer, the growth of the field amplitude gets higher and energy density inside the layer gets stronger (Fig. 4.3).

4.4 Optimization and design of degenerate band edge crystals

Different from the stationary inflection points in the gyrotropic crystals, the third derivative of the dispersion relation also needs to be zero in the degenerate band edge crystals, i.e.

$$\frac{\partial \omega}{\partial k} = 0, \quad \frac{\partial^2 \omega}{\partial k^2} = 0, \quad \frac{\partial^3 \omega}{\partial k^3} = 0 \qquad \text{at} \;\; \omega = \omega_0$$

According to the paper [11], the following set of parameters generates a degenerate band edge point at $k_0 = \pi$.

$$\text{For } \mathbf{A} \text{ layer} : \hat{\varepsilon} = \begin{bmatrix} 13.61 + 12.40\cos(2\phi) & 12.40\sin(2\phi) \\ 12.40\sin(2\phi) & 13.61 - 12.40\cos(2\phi) \end{bmatrix}, \quad \hat{\mu} = \mathbf{I}$$

$$\phi_1 = 0, \quad \phi_2 = \pi/4, \ \mathrm{L_V} = 0.45891, \quad \mathrm{L_A} = 0.5(1.0 - \mathrm{L_V}), \quad L = 2L_A + L_V$$

$$k_0 = \pi, \qquad \omega_0 = 1.0094052895(c/L)$$

where L_A and L_V are the thickness of anisotropic layer and vacuum, respectively. One of main advantages of this configuration is the absence of magnetic component which is both complicated and difficult to manufacture with a sufficiently low loss. As shown in Fig. 4.4, the dispersion relation is indeed flat at the degenerate band edge point which increases the speed of convergence when minimizing

$$J = \lambda \left|\frac{d\omega}{dk}\right| + \left|\frac{d^2\omega}{dk^2}\right| \qquad \text{at} \ \ k_0 = \pi$$

Similar to the previous magnetic case, the one-dimensional nature of the problem enables the use of the transfer matrix method, which is expressed as follows.

$$T_L(\phi 1, \phi 2, L_{A1}, L_{A2}, L_V) = T_A(\phi_2, L_{A2}) T_V(L_V) T_A(\phi_1, L_{A1})$$

where

$$T_V(L_V) \quad = \quad W(L_V)W^{-1}(0), \quad W(L_V) = \begin{bmatrix} e^{iv} & e^{-iv} & -e^{ivf} & -e^{-iv} \\ e^{iv} & e^{-iv} & e^{iv} & e^{-iv} \\ -e^{iv} & e^{-iv} & -e^{iv} & e^{-iv} \\ e^{iv} & -e^{-iv} & -e^{iv} & e^{-iv} \end{bmatrix}$$

and $v = \frac{\omega}{c} L_V$. The structure of the periodic array shown in Fig. 4.4 always displays a degenerate band edge at $k_0 = \pi$ independent of input parameters, so we don't need to find another candidates sets of k_0. As for the parameters of optimization, similar to magnetic frozen mode, we consider the thickness of the vacuum layer (L_V), the thickness of the first anisotropic layer (L_{A1}) and the material constants of the anisotropic layer (ε_A, δ_A).

Fig. 4.5 shows the sequence of convergence of the dispersion relation for a degenerate band edge point for optimization using one variable L_V to recover the known solution, confirming the robustness of the method and the computed solution.

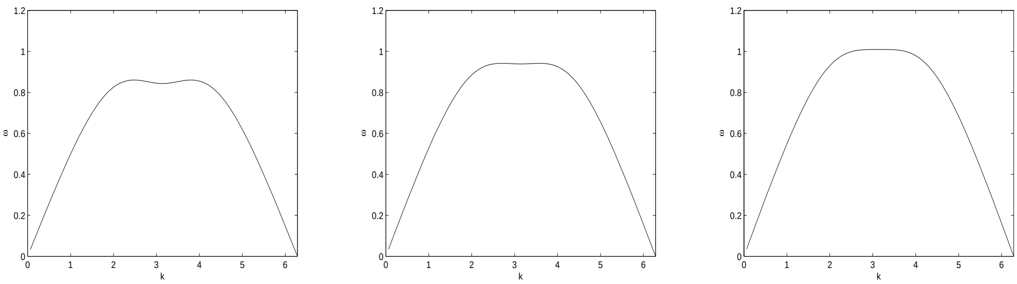

Figure 4.5: Scenes from optimization process with one variable L_V(left to right). L_V=0.3029 (left), 0.3994 (center), 0.4589 (right) after 6 iterations, $\frac{d\omega}{dx}$= 2.6258e-015, $\frac{d^2\omega}{dx^2}$= 1.3466e-013 with λ = 100.

In Table 4.2, we show other solutions found by using different parameters(n) for optimizations. We observe that the thickness of vacuum is approximately the same for all sets, but the thickness of anisotropic layer varies. The first derivative and the second derivative of all sets are less than 1.0e-10, which is sufficiently small to make the phenomena distinctive in the time domain.

However, one big difference is that the transmittance rate of set 4 is significantly larger than those for the other sets in some contrast to the widely held belief that total reflectance or negligible amount of transmittance rate at degenerate band edge is inevitable.

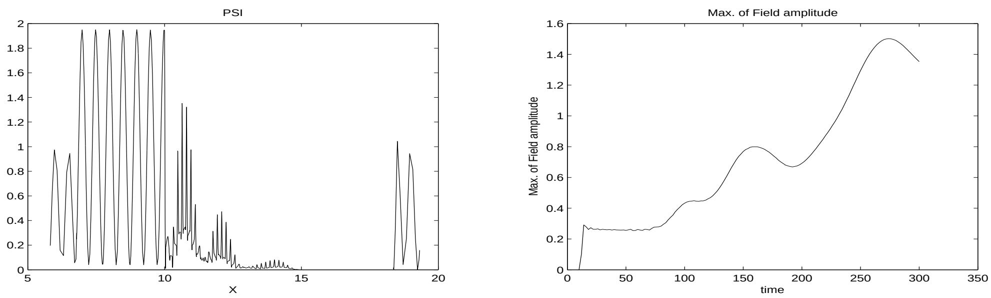

Figure 4.6: Field amplitude(left) and Maximum of field amplitude (right) of Degenerate band edge with set 1 of Table 4.2. Number of unit cell=32. Number of grid points per each domain=12. One unit cell = A1+V+A2 as shown in Fig. 4.4. E$\|$x polarization.

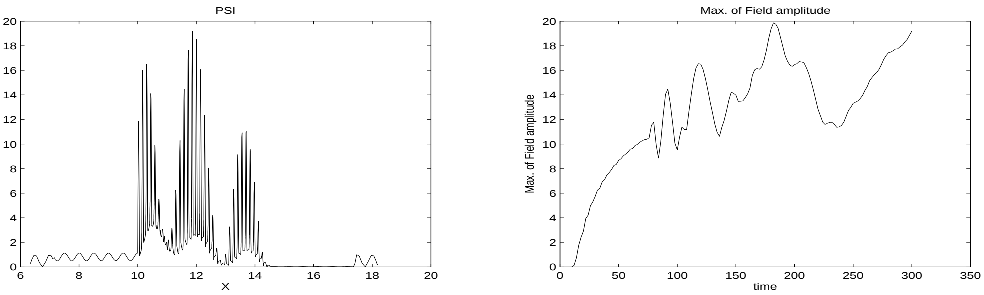

Figure 4.7: Field amplitude(left) and maximum of field amplitude (right) of degenerate band edge with parameter set 4 of Table 4.2. Number of unit cell=32. Number of grid points per each domain=12. One unit cell = A1+V+A2 as shown in Fig. 4.4, E$\|$x polarization.

		Set1	Set2	Set3	Set4
Input	n	1	2	2	4
	variables	$L_V(L_{A1} = L_{A2})$	L_V, L_{A1}	L_V, L_{A1}	$L_V, L_{A1}, \varepsilon_A, \delta_A$
	ϕ_2	$\pi/4$	$\pi/4$	$\pi/3$	$\pi/4$
Solution	L_V	0.45890	0.46000	0.45005	0.45005
	L_{A1}	0.27055	0.29190	0.43633	0.45050
	ε_A	5.1	5.1	5.1	7.0
	δ_A	1.1	1.1	1.1	3.92
	ω_0	1.00940	1.01331	1.11726	0.88645
	k_0	π	π	π	π
	$\frac{d\omega}{dk}\|_{\omega=\omega_0}$	2.9175e-16	2.9063e-16	0*	4.3189e-15
	$\frac{d^2\omega}{dk^2}\|_{\omega=\omega_0}$	6.0364e-14	1.3414e-13	1.5102e-013	3.8326e-10
	TR rate	0.0064	0.0070	0.0440	0.3474

Table 4.2: Optimized solutions with different number of variables(n) or different initial values for degenerate band edge. ϕ_2=misalignment angle of second anisotropic layer(we let $\phi_1 = 0$). L_V= thickness of vacuum, L_{A1}=thickness of the first anisotropic layer. TR (Transmittance) rate = I_T/I_I, $I \equiv \frac{1}{\mu_0} < E \times B >$, $<>$= time average over one cycle. * = the value is less than machine accuracy. ε_A and δ_A are used in the permittivity of anisotropic layer as follows.

$$\hat{\varepsilon} = \begin{bmatrix} \varepsilon_A + \delta_A \cos(2\phi) & \delta_A \sin(2\phi) \\ \delta_A \sin(2\phi) & \varepsilon_A - \delta_A \cos(2\phi) \end{bmatrix}$$

When it was believed so, as one of way to increase the transmittance rate, Figotin and Vitebsky suggested to use Fabry-Pérot peak cavity resonance in the paper [11]. In other words, instead of sending a monochromatic wave with the exact degenerate band edge frequency ω_0, we send a monochromatic wave with ω_1 which is slightly different from ω_0 but with a transmittance rate which is significantly higher because of the finiteness of the slab.

One of optimized solutions shows a transmittance rate of 0.3474 approximately, which is more than 50 times larger than those of the other sets. This result seems to be encouraging, since we don't need to blur the distinctive features of the frozen mode by using ω_1 different from ω_0. Figs. 4.6 and 4.7 show the field amplitude at T=300.0 and the increase of the maximum field amplitude with set 1 and set 4 of Table 4.2. These figures clearly display the significance of large transmittance rate at the degenerate band edge.

4.5 Optimization and design of oblique frozen mode crystals

As proposed by Figotin and Vitebsky [10, 22], stationary inflection points can be also generated without magnetic layers and with structures even simpler as the degenerate band gap structures. To achieve this goal, one needs to break the symmetry and consider incident waves at oblique angles. When an oblique incident waves propagates into a periodic layer consisting of one anisotropic layer with $\varepsilon_{xz} \neq 0$ (ε_{xz} = xz component of permittivity tensor $\hat{\varepsilon}$) and vacuum, we can observe similar, but weaker frozen mode inside the layer as compared to the gyrotropic crystal.

However, the crystal parameters in [10, 22] were computed by one dimensional transfer matrix method based on the following tangential consistency of the wave to eliminate the derivatives along x, y directions, i.e.,

$$\frac{d\hat{E}}{dx} = ik_{x,y}\hat{E} = \left(\frac{k_{x,y}}{\omega}\right) i\omega\hat{E} = \left(\frac{k_{x,y}}{\omega}\right)\left(-\frac{d\hat{E}}{dt}\right)$$

where $k_{x,y}$ is the component of the wave vector $\vec{k}$ along x, y direction and ω is the frequency of the incident plane wave. The frozen mode was shown to

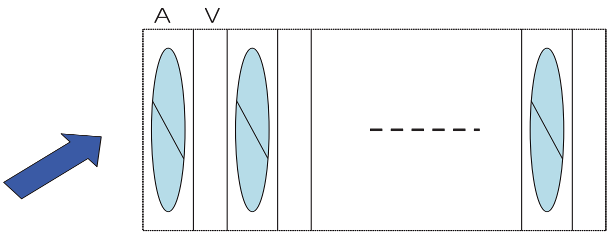

Figure 4.8: Array of crystals displaying the oblique frozen mode. The periodic structure consists of one anisotropic layer (A) with $\varepsilon_{xz} \neq 0$ and vacuum (V) between them. The incident waves need to propagate into the layer at an oblique angle.

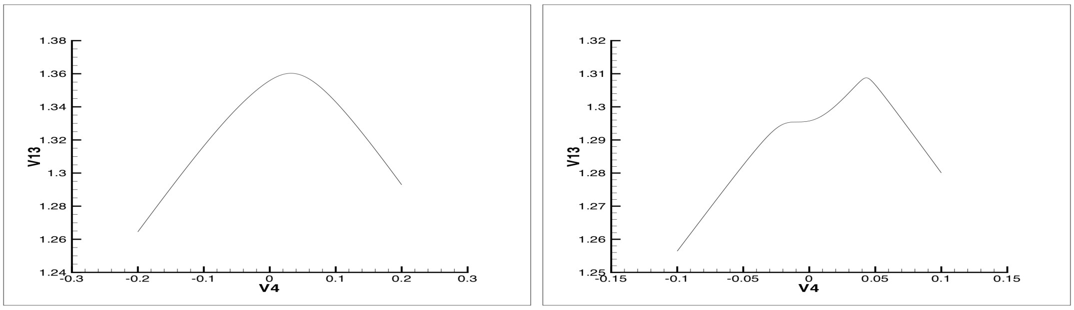

Figure 4.9: Dispersion relation for the three-dimensional Maxwell eigenvalue problem with material parameters from paper [22] (left), and with the optimized solution for the 8th band(right). A stationary inflection point ω_0 is observed in the dispersion relation only with the optimized solution

exist by Chun and Hesthaven [6], after applying the above consistency into the Maxwell's equations. However, the existence of the oblique frozen mode in real three dimension remains in question since the above condition is artificial. To model this general case where the transfer matrix method is not applicable, we must solve the full Maxwell eigenvalue problems for the dispersion relation.

The solution of this more complicated problem can be computed with a freely available frequency-domain solver [23]. In addition to choosing a wave vector $\vec{k}_0$ for the stationary inflection point ω_0, we need to choose a band containing ω_0. For example, ω_0 exists on the second band and the first band for the magnetic frozen mode and degenerate band edge respectively, but for the oblique frozen mode, no such information is known in advance. To identify the band where ω_0

exist, we search whole bands for a wave vector $\vec{k}_0$ such as

$$D_{12}(\vec{k}_0) = \min_p \left| \sum_{j=p-2}^{p+2} \frac{d\omega}{dk}(\vec{k}_j) \right| < \delta, \qquad \delta = \text{small number}$$

To increase the speed of the search process, we choose several bands in advance which seem to have $\vec{k}_0$ satisfying the above inequality. As for parameters for optimization, we use the oblique angle of incident wave ($k_x = k_y$), the thickness of vacuum (L_V) and material constants of anisotropic layer ($\varepsilon_{11}, \varepsilon_{33}$) with which material constant matrix is given as

$$\hat{\varepsilon}_A = \begin{bmatrix} \varepsilon_{11}\cos\theta^2 + \varepsilon_{33}\sin\theta^2 & 0 & (\varepsilon_{11} - \varepsilon_{33})\cos\theta\sin\theta \\ 0 & \varepsilon_{22} & 0 \\ (\varepsilon_{11} - \varepsilon_{33})\cos\theta\sin\theta & 0 & \varepsilon_{33}\cos\theta^2 + \varepsilon_{11}\sin\theta^2 \end{bmatrix}$$

Among several stationary inflection points found by optimization, one of them with the lowest frequency ω_0 is given as follows (also see Fig. 4.9):

$$\begin{aligned} &\theta = \pi/4 \\ &\varepsilon_{11} = \varepsilon_{22} = 4.66812966, \quad \varepsilon_{33} = 3.9656, \quad L_V = 0.5711535 \\ &\vec{k} = (-0.4800309, -0.4800309, -0.008982), \quad \omega_0 = 1.295439\ (c/L) \\ &\left.\frac{d\omega}{dk}\right|_{\omega=\omega_0} = 0.00048279, \qquad \left.\frac{d^2\omega}{dk^2}\right|_{\omega=\omega_0} = 0.004393 \end{aligned}$$

The dispersion relation resulting from the new parameters clearly show the correct properties for the three-dimensional crystal.

4.5.1 Time-domain modeling of the 3D crystal

To observe the phenomena in three dimension, the new set of optimized parameters is solved in a time-domain wave propagation model with periodic boundary condition along x, y direction [32]. The periodic boundaries are x and y sides and absorbing boundary condition (ABC) is added at the end of z-direction to truncate unnecessary reflection of the outgoing waves (Fig. 4.10). Let only ε_{xz} be non-zero off-diagonal element for permittivity tensor $\hat{\varepsilon}$,

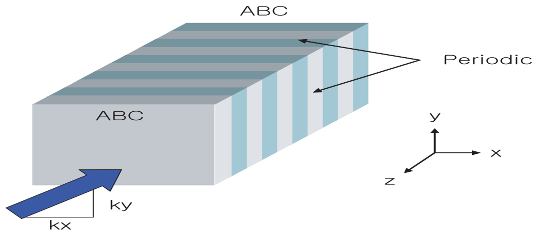

Figure 4.10: Wave propagation problem with periodic boundary condition along x and y direction with ABC at the end of z direction. The incident wave propagates into the layer with an oblique angle

$$\begin{bmatrix} \frac{\partial \tilde{E}_z}{\partial y} - \frac{\partial \tilde{E}_y}{\partial z} \\ \frac{\partial \tilde{E}_x}{\partial z} - \frac{\partial \tilde{E}_z}{\partial x} \\ \frac{\partial \tilde{E}_y}{\partial x} - \frac{\partial \tilde{E}_x}{\partial y} \end{bmatrix} = -\frac{\partial}{\partial t} \begin{bmatrix} \tilde{H}_x \\ \tilde{H}_y \\ \tilde{H}_z \end{bmatrix}, \qquad \begin{bmatrix} \frac{\partial \tilde{H}_z}{\partial y} - \frac{\partial \tilde{H}_y}{\partial z} \\ \frac{\partial \tilde{H}_x}{\partial z} - \frac{\partial \tilde{H}_z}{\partial x} \\ \frac{\partial \tilde{H}_y}{\partial x} - \frac{\partial \tilde{H}_x}{\partial y} \end{bmatrix} = \begin{bmatrix} \varepsilon_{xx} & 0 & \varepsilon_{xz} \\ 0 & \varepsilon_{yy} & 0 \\ \varepsilon_{xz} & 0 & \varepsilon_{zz} \end{bmatrix} \frac{\partial}{\partial t} \begin{bmatrix} \tilde{E}_x \\ \tilde{E}_y \\ \tilde{E}_z \end{bmatrix}$$

Assuming periodicity along x, y direction, we can express $\tilde{E}$ and $\tilde{H}$ as two dimensional Fourier series as follows.

$$\begin{aligned} \tilde{E}(x,y,z,t) &= \sum_{m_y=-N_y/2}^{N_y/2} \sum_{m_x=-N_x/2}^{N_x/2} E(m_x,m_y,z,t) e^{im_x \frac{2\pi}{L_x} x} e^{im_y \frac{2\pi}{L_y} y} \\ \tilde{H}(x,y,z,t) &= \sum_{m_y=-N_y/2}^{N_y/2} \sum_{m_x=-N_x/2}^{N_x/2} H(m_x,m_y,z,t) e^{im_x \frac{2\pi}{L_x} x} e^{im_y \frac{2\pi}{L_y} y} \end{aligned}$$

where N_x, N_y are number of points along x, y direction and L_x, L_y are length of domain along x and y direction, respectively. Note that L_x and L_y depend on the angle of incidence of plane wave. By substituting these expansions into the above Maxwell's equations after implementing ABC, we have

$$\begin{aligned} \begin{bmatrix} (im_y)E_z - \frac{\partial E_y}{\partial z} \\ \frac{\partial E_x}{\partial z} - (im_x)E_z \\ (im_x)E_y - (im_y)E_x \end{bmatrix} &= i\omega \begin{bmatrix} s_z & 0 & 0 \\ 0 & s_z & 0 \\ 0 & 0 & 1/s_z \end{bmatrix} \begin{bmatrix} H_x \\ H_y \\ H_z \end{bmatrix} \\ \begin{bmatrix} (im_y)H_z - \frac{\partial H_y}{\partial z} \\ \frac{\partial H_x}{\partial z} - (im_x)H_z \\ (im_x)H_y - (im_y)H_x \end{bmatrix} &= -i\omega \begin{bmatrix} \varepsilon_{xx} & 0 & \varepsilon_{xz} \\ 0 & \varepsilon_{yy} & 0 \\ \varepsilon_{xz} & 0 & \varepsilon_{zz} \end{bmatrix} \begin{bmatrix} s_z & 0 & 0 \\ 0 & s_z & 0 \\ 0 & 0 & 1/s_z \end{bmatrix} \begin{bmatrix} E_x \\ E_y \\ E_z \end{bmatrix} \end{aligned}$$

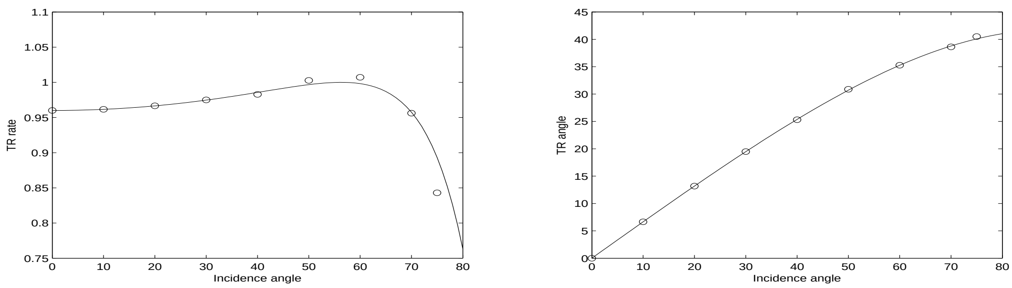

Figure 4.11: Results of testing the code for 3D time domain modeling with periodicity along x,y direction. Transmittance rate vs. incidence angle (left), transmittance angle vs. incidence angle (right). Solid line indicates the exact value and circles indicate computed values.

where ω is the frequency of the incident plane wave and by substituting PML parameter s_z such as $s_z = 1+\sigma_z/(i\omega)$, we have the following Maxwell's equations in the time domain($\forall\ m_x \leq |N_x/2|,\ \forall\ m_y \leq |N_y/2|,\ D_\varepsilon = \varepsilon_{xx}\varepsilon_{zz} - \varepsilon_{xz}^2$)

$$
\begin{aligned}
\frac{\partial H_x}{\partial t} &= \frac{\partial E_y}{\partial z} - (im_y)E_z - \sigma_z H_x \\
\frac{\partial H_y}{\partial t} &= -\frac{\partial E_x}{\partial z} + (im_x)E_z - \sigma_z H_y \\
\frac{\partial B_z}{\partial t} &= -(im_x)E_y + (im_y)E_x \\
\frac{\partial H_z}{\partial t} &= \frac{\partial B_z}{\partial t} + \sigma_z B_z \\
D_\varepsilon \frac{\partial E_x}{\partial t} &= -\varepsilon_{zz}\{\frac{\partial H_y}{\partial z} - (im_y)H_z\} + \varepsilon_{xz}\{(im_y)H_x - (im_x)H_y\} - \sigma_z E_x \\
\varepsilon_{yy}\frac{\partial E_y}{\partial t} &= \frac{\partial H_x}{\partial z} - (im_x)H_z - \sigma_z E_y \\
D_\varepsilon \frac{\partial D_z}{\partial t} &= \varepsilon_{xz}\{\frac{\partial H_y}{\partial z} - (im_y)H_z\} - \varepsilon_{xx}\{(im_y)H_x - (im_x)H_y\} \\
\frac{\partial E_z}{\partial t} &= \frac{\partial D_z}{dt} + \sigma_z D_z
\end{aligned}
$$

A Discontinuous Galerkin Method is used for differentiation along z-direction as in the paper [18, 19]. As for time marching, we implement implicit scheme for the linear derivatives along z direction and explicit scheme for the remainder [4, 24]. To validate the code, the transmittance rate and transmittance angle are computed when a plane incident wave propagating from vacuum to a dielectric

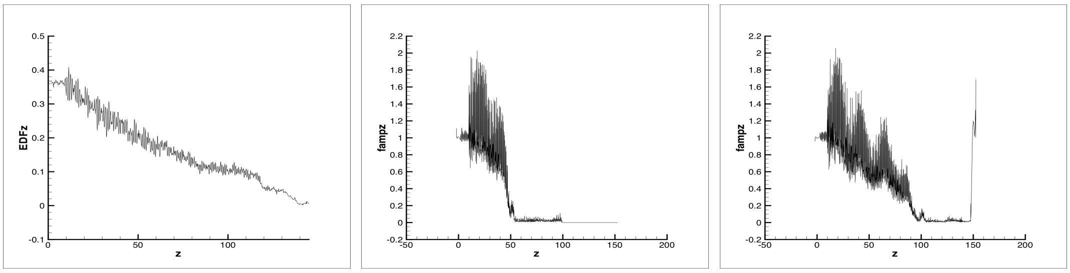

Figure 4.12: Energy density flux (left) and the field amplitude with optimized parameters at T=100 (center) and at T=200 (right), $N_x = N_y = 6, \quad N_z = 12$, $N_x,\ N_y,\ N_z$=number of grid points along x, y, z. Number of unit cell=100.

material with various oblique angles. As shown in Fig. 4.11, it demonstrates the excellent performance of the scheme

In Fig. 4.12, we show the energy density flux $\left[\frac{1}{\mu_0}(\mathbf{E} \times \mathbf{B})\right]$ and the field amplitude $[|\mathbf{E}|^2 + |\mathbf{H}|^2]$ with the optimized parameter values and observe several features of the frozen mode. In behalf of analysis, let's define energy density flux difference(EDFD) as shown in [6]

$$\text{EDFD} = \int_S \mathbf{e}_f \cdot nds = \int_V \nabla \mathbf{e}_f dV, \qquad \mathbf{e}_f = \text{energy density flux}$$

Note that this EDFD indicates the amount of energy density stacked inside the layer per unit time. Then, we observe that there are significant amounts of EDFD along the z direction between the first cell and the last cell(see the right figure of Fig. 4.13). This leads to an increased field amplitude, compressed energy density and the slow-down of waves. However, each of these phenomena are weaker than that of magnetic frozen mode as expected [6]. The maximum of the field amplitude is increasing very slowly and the average velocity of the energy transfer is approximately $0.4c$.

Fig. 4.13 compares EDFD for all directions for the crystals based on the original values with the optimized values. With the optimized values, we observe EDFD along x, y direction are almost zero, but EDFD along the z direction remains significantly large even after a long time. With original values, EDFD along the x, y direction remains nontrivial, which seems to explain why no frozen mode is observed with the original configuration.

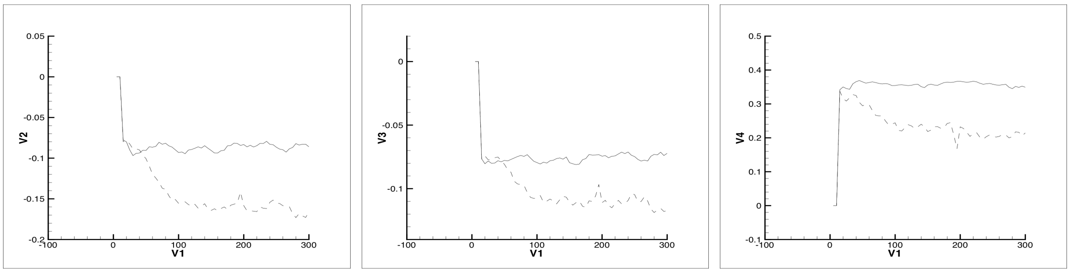

Figure 4.13: Energy Flux Density Difference (EDFD) between the first cell and the last cell along x (left), y (center), z (right) direction. Solid line is with optimized parameters, dashed line is with original values. $N_x = N_y = 6, \quad N_z = 12$, Number of unit cell=64

4.6 Conclusion

In this chapter, we have explored the use of PDE constrained optimization along with design and optimization of photonic crystals exhibiting frozen mode behavior. This phenomenon is related to the existence of Van Hove singularities in the dispersion relation. We have demonstrated the ability to recover known solutions as well as computed several new sets of parameters by optimizing the geometry and/or the materials of the crystals. For both of the magnetic frozen mode and degenerate band edge, each sets of parameters obtained by optimization with different number of variables show the generally similar phenomena, but some features are different. Above all, the transmittance rate varies significantly, which is a crucial element for energy density and field amplitude inside the layer. In particular one set for the degenerate band edge displays a transmittance rate around 0.3475, which is more than 50 times larger than those of the others.

For the case with the frozen mode requiring an oblique illumination, we succeed in finding a stationary inflection point in three dimensions with parameters' sets derived by nonlinear optimization. The existence of the frozen mode in three dimension is shown for the first time, but the phenomena themselves are not as distinctive as the previous two instances. One of the reason can be the intrinsic property of the oblique array which makes wave vector k_0 too close to zero.

The current computational design tool allows one to specify materials and/or geometries, then seek to design crystals with the sought-after properties, if they exist. The computations shown here illustrate, however, that the Van Hove singularities are found broadly in the dispersion relations, indicating that many configurations often exist. Future works may include finding stationary inflection points or degenerate band edge points showing strong frozen mode in two or three dimensional structures. We also believe that using a more complex geometry, but employing simpler materials, can be a candidate for exploring similar behavior.

Chapter 5

Thin layer approximations for time-domain electromagnetics. Part I: General metal backed coatings

In this chapter, we present a family of high-order accurate thin layer approximations for time-domain electromagnetics. The thin layer approximations are valid for metal backed coatings of general anisotropic materials on smooth curvilinear backgrounds and both dielectric and magnetic materials can be considered. The implementation of these models is non-trivial and we discuss this in the context of discontinuous Galerkin methods which are particularly well suited for these approximations. The range of validity, accuracy, and stability of the resulting schemes is demonstrated through one- and two-dimensional examples.

What remains is structured as follows. In section 5.1 we sketch the derivation of the general family of effective boundary conditions for thin coatings that we consider. This sets the stage for section 5.2 where we briefly introduce the discontinuous Galerkin methods for time-domain electromagnetics and discuss how the effective boundary conditions fit very well within this formulation. In section 5.3, we consider the performance of the effective boundary conditions for several one-dimensional test cases to illustrate the behavior and convergence order of the thin coating models. This is extended in section 5.4 to general two-dimensional

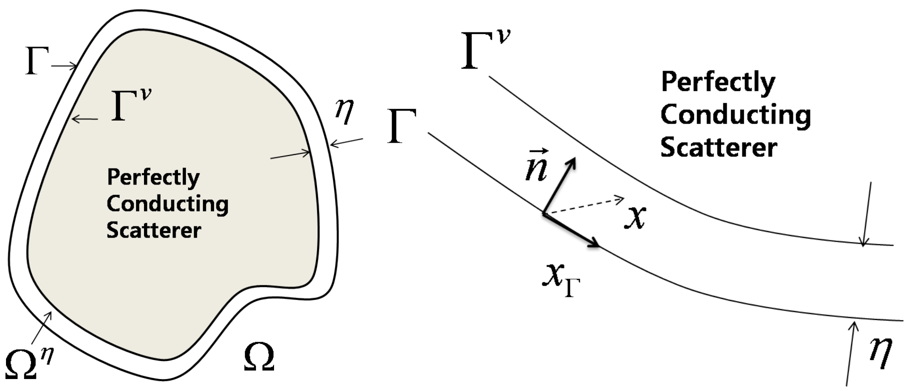

Figure 5.1: On the left we summarize the definitions of the domains and the boundaries and on the right we show the local coordinate system used along the smooth scatterer boundary.

cases with curvilinear metallic backings and we also consider range of validity for thick coatings and the extension to problems with non-smooth metal backing. In section 5.5, we summarize the results and discuss the extension to cases with multi-layer coatings and other generalizations.

5.1 Formulation of effective time-domain boundary conditions

Let us consider a general but smooth perfectly conducting scatterer in Ω and assume that it is coated with a thin homogeneous material layer of uniform thickness η as illustrated in Fig. 5.1. Let Ω^η represent the thin layer.

Assume that Γ^v is the interface between the thin layer and the scatterer and that Γ is the interface between the thin layer and free space. We shall assume that that all boundaries are smooth but no other restrictions are imposed.

We introduce E^η, H^η as the electric and magnetic fields, respectively, and let $\hat{\varepsilon}^\eta$, $\hat{\mu}^\eta$ be the permittivity and permeability tensor in the thin layer Ω^η. Furthermore, in $\Omega^v (\equiv \Omega \backslash \Omega^\eta)$ we have E, H as the electric and magnetic fields and we let $\hat{\varepsilon}$, $\hat{\mu}$ be the permittivity and permeability tensors. Outside the scatterer we typically assume vacuum, although this is not required.

Consider now the coupled system of Maxwell's equations

$$\hat{\varepsilon}\frac{\partial E}{\partial t} - \nabla \times H = 0, \quad \hat{\mu}\frac{\partial H}{\partial t} + \nabla \times E = 0 \qquad x \in \Omega \backslash \Omega^{\eta} \tag{5.1}$$

$$\hat{\varepsilon}^{\eta}\frac{\partial E^{\eta}}{\partial t} - \nabla \times H^{\eta} = 0, \quad \hat{\mu}^{\eta}\frac{\partial H^{\eta}}{\partial t} + \nabla \times E^{\eta} = 0 \qquad x \in \Omega^{\eta} \tag{5.2}$$

with the boundary conditions

$$E^{\eta} \times n = 0, \qquad x \in \Gamma^{\eta} \tag{5.3}$$

$$E \times n = E^{\eta} \times n, \quad H \times n = H^{\eta} \times n, \qquad x \in \Gamma, \tag{5.4}$$

where n represents the outward pointing normal vector. Under assumption of a constant layer thickness, n is taken to be the same on Γ and Γ^{v}. Assume now that the layer, Ω^{η}, is thin compared to a characteristic wavelength if the sources. In this case the two systems of equations, Eqs. (5.1)-(5.2), have very different scales introduced by the geometry which would cause computational difficulties.

Let us therefore seek to construct an effective boundary conditions on Γ of the form

$$E \times n = \mathfrak{B}^{k}(n \times (H \times n)), \qquad x \in \Gamma.$$

Here $\mathfrak{B}^{k}$ represents the effective conditions and connects the field components at the interface through a scheme which mimics the presence of the thin coating. The parameter k reflects a hierarchy of conditions of increasing order of accuracy. If we are successful in deriving such a model, we can apply these effective boundary conditions to the exterior system, Eq. (5.1), to model the impact of the thin coating through the effective boundary condition.

We express the point x inside Ω^{η} as

$$x = x_{\Gamma} + sn = x_{\Gamma} + \eta\nu n, \qquad x_{\Gamma} \in \Gamma, \ \nu \in [0,1]$$

where we assume that the layer has a constant thickness and is homogeneous. Note that n can vary along the curve. Under the thin layer assumption we then make the formal approximation through the expansion of E^{η} and H^{η} as

$$\begin{aligned} E^{\eta}(x,t) &= E_0(x_{\Gamma},\nu,t) + \eta E_1(x_{\Gamma},\nu,t) + \eta^2 E_2(x_{\Gamma},\nu,t) + \cdots \\ H^{\eta}(x,t) &= H_0(x_{\Gamma},\nu,t) + \eta H_1(x_{\Gamma},\nu,t) + \eta^2 H_2(x_{\Gamma},\nu,t) + \cdots \end{aligned} \tag{5.5}$$

Note in particular that E_k and H_k are both independent of η and depends only on the position x_Γ along the boundary and the normalized position ν in the layer.

Along the general layer surface x_Γ, the differential operator ∇ is

$$\nabla = \nabla_\Gamma + \frac{1}{\eta}\frac{\partial}{\partial \nu},$$

and the corresponding curl operator $\nabla\times$ takes the form (see [13] for a detailed proof)

$$\nabla \times V = \mathcal{T}_\Gamma^s V - \frac{1}{\eta}\frac{\partial}{\partial \nu}(V \times n),$$

for the generic vector field V. Here

$$\mathcal{T}_\Gamma^s V = [(\mathcal{R}_s \nabla_\Gamma)\cdot(V\times n)]n + [\mathcal{R}_s\nabla_\Gamma(V\cdot n)]\times n - (\mathcal{R}_s \mathcal{C} V)\times n$$

and we have the curvature tensor, $\mathcal{C} = \vec{\nabla} n$ and $\mathcal{R}_s(\Pi_{||} + s\mathcal{C}) = \Pi_{||}$ is the projection operator along the tangential direction of Γ. Inserting this into Eq. (5.2), we obtain

$$\begin{aligned}
&\hat{\varepsilon}^\eta \frac{\partial E^\eta}{\partial t} - \mathcal{T}_\Gamma^s H^\eta + \frac{1}{\eta}\frac{\partial}{\partial \nu}(H^\eta \times n) = 0, \qquad x \in \Omega^\eta \\
&\hat{\mu}^\eta \frac{\partial H^\eta}{\partial t} + \mathcal{T}_\Gamma^s E^\eta - \frac{1}{\eta}\frac{\partial}{\partial \nu}(E^\eta \times n) = 0.
\end{aligned} \tag{5.6}$$

We then assume the validity of the expansion

$$\mathcal{R}_s = \Pi_{||} + \sum_{i=1}^{\infty}(-\eta\nu\mathcal{C})^i,$$

to obtain the expansion of $\mathcal{T}_\Gamma^s$ as

$$\mathcal{T}_\Gamma^s = \sum_{i=0}^{\infty}(-s)^i \mathcal{T}_\Gamma^i \tag{5.7}$$

where

$$\mathcal{T}_\Gamma^i V = [(\mathcal{C}^i \nabla_\Gamma)\cdot(V\times n)]n + [\mathcal{C}^i\nabla_\Gamma(V\cdot n)]\times n - (\mathcal{C}^{i+1}V)\times n.$$

Substituting Eqs. (5.5) and (5.7) into Eq. (5.6), we obtain the following hierarchy of equations for $k = 0,\ 1,\ 2, \ldots$

$$\hat{\varepsilon}^{\eta}\frac{\partial E_k}{\partial t} - \sum_{i=1}^{k}(-\nu)^i \mathcal{T}_{\Gamma}^i H_{k-i} + \frac{\partial}{\partial \nu}(H_{k+1}\times n) = 0 \qquad x \in \Omega^{\eta} \tag{5.8}$$
$$\hat{\mu}^{\eta}\frac{\partial H_k}{\partial t} + \sum_{i=1}^{k}(-\nu)^i \mathcal{T}_{\Gamma}^i E_{k-i} - \frac{\partial}{\partial \nu}(E_{k+1}\times n) = 0.$$

subject to the boundary conditions

$$n \times E_{k+1}(x_{\Gamma}, 1, t) = 0, \tag{5.9}$$
$$n \times H_{k+1}(x_{\Gamma}, 0, t) = n \times H_{k+1}(\Gamma).$$

Solving Eqs. (5.8)-(5.9) up to k leads to an effective boundary condition of order $(k{+}1)$'th order of effective boundary conditions(EBC) which can then be used to supply boundary conditions to the exterior Maxwell's equations, Eq. (5.1).

The effective boundary condition of order 2 becomes

$$\frac{\partial E}{\partial t}\times n = -\eta\hat{\mu}^{\eta}\frac{\partial^2 \varphi}{\partial t^2} - \eta\left(\hat{\varepsilon}^{\eta}\right)^{-1}\vec{\nabla}_{\Gamma}\times(\nabla_{\Gamma}\times\varphi), \qquad x \in \Gamma \tag{5.10}$$

and the third order condition is

$$\frac{\partial E}{\partial t}\times n = -\eta\hat{\mu}^{\eta}[1-\eta(\mathcal{C}-\mathcal{H})]\frac{\partial^2 \varphi}{\partial t^2}$$
$$-\eta\left(\hat{\varepsilon}^{\eta}\right)^{-1}\vec{\nabla}_{\Gamma}\times[1-\eta\mathcal{H}](\nabla_{\Gamma}\times\varphi),\ x \in \Gamma \tag{5.11}$$

Here $\varphi = \Pi_{||}H = n \times (H \times n)$ and

$$\vec{\nabla}_{\Gamma}\times V = (\nabla_{\Gamma}V)\times n,\ \ \nabla_{\Gamma}V = \nabla_{\Gamma}\cdot(V\times n),$$

and $\mathcal{H} = \frac{1}{2}\mathrm{tr}\mathcal{C}$ is the mean Gaussian curvature.

The general approach can be continued although the expressions become increasingly complex. A fourth order effective boundary condition for planar boundaries is given as

$$\frac{\partial E}{\partial t}\times n = -\eta\hat{\mu}^{\eta}\frac{\partial^2 \Psi}{\partial t^2} - \eta\left(\hat{\varepsilon}^{\eta}\right)^{-1}\vec{\nabla}_{\Gamma}\times(\nabla_{\Gamma}\times\Phi) \qquad x \in \Gamma \tag{5.12}$$
$$\Phi + \frac{\eta^2}{3}\vec{\nabla}_{\Gamma}\times(\nabla_{\Gamma}\times\Phi) = \varphi$$
$$\Psi + \frac{\eta^2}{3}\left(\bar{\varepsilon}^{\eta}\hat{\mu}^{\eta}\frac{\partial^2\Psi}{\partial t^2} - \vec{\triangle}_{\Gamma}\Psi + \vec{\nabla}\times(\nabla\times\Psi)\right) = \varphi,$$

where $\bar{\varepsilon}^\eta = \mathrm{tr}\hat{\varepsilon}^\eta - \hat{\varepsilon}^\eta$ and

$$\triangle_\Gamma V = \nabla_\Gamma(\nabla_\Gamma \cdot V) - \vec{\nabla}_\Gamma \times (\nabla_\Gamma \times V).$$

5.2 Time-domain scheme using a discontinuous Galerkin method

The efficient boundary conditions discussed above have to be solved along with the free-space Maxwell's equations, given in Eq. (5.1). Since the main interest is in problems with geometrically complex coated scatterer illuminated by time-dependent sources, a body conforming time-domain formulation is most natural and classic finite-difference time-domain schemes are ruled out. Furthermore, since the goal here is to demonstrate the high-order accuracy of the efficient boundary conditions, it is essential that a high-order accurate scheme be considered.

Based on these observations, it is natural to consider a discontinuous Galerkin method [15] which has been developed during the last decade and has shown great promise as a flexible, accurate, and robust way of solving the time-domain Maxwell's equations [14].

Let us briefly sketch the derivation of the discontinuous Galerkin scheme for the time-domain Maxwell's problem. We begin by assuming that the computational vacuum domain, Ω^v, is approximated by K elements D^k as

$$\Omega^v \simeq \sum_{k=1}^{K} D^k$$

where we assume that D^k are d-dimensional simplices.

In each of these elements we assume that E and H can be approximation by Lagrange polynomials (ℓ_j) as

$$[E_h, H_h] = \sum_{j=1}^{N} [E(x_j,t), H(x_j,t)]\ell_j(x),$$

where x_j are the interpolation points on which the Lagrangian basis is based. The number of terms N in the expansion is given as

$$N = \begin{pmatrix} n+d \\ n \end{pmatrix}$$

for the n'th order polynomial in d-dimensions. For details of how this local interpolation is recovered we refer to [15].

To derive the scheme, we insert the approximate solutions into Maxwell's equations and require that local residual is orthogonal to all n'th order polynomials. Integration by parts twice this yields the scheme

$$\begin{aligned} \int (\hat{\varepsilon}\frac{\partial E_h}{\partial t} - \nabla \times H_h)\ell_i(x)\, dx &= -\int_{\partial \mathsf{D}^k} n^k \times (H_h - H^*)\ell_i(x) dx \\ \int (\hat{\mu}\frac{\partial H_h}{\partial t} + \nabla \times E_h)\ell_i(x)\, dx &= \int_{\partial \mathsf{D}^k} n^k \times (E_h - E^*)\ell_i(x) dx \end{aligned}$$

where $[E^*, H^*]$ indicates the numerical flux of the corresponding vector quantity and n^k reflects the outward pointing normal vector along ∂D^k. It is the numerical flux which is responsible for the coupling of the elements, for the stability of the scheme, and the imposition of boundary conditions.

Enforcing the effective boundary conditions is done though the numerical flux for those elements sharing a face with Γ as

$$\begin{aligned} \int (\hat{\varepsilon}\frac{\partial E_h}{\partial t} - \nabla \times H_h)\ell_i(x)\, dx = \quad & -\int_{\partial \mathsf{D}^k \backslash \Gamma} n^k \times (H_h - H^*)\ell_i(x) dx \\ & -\oint_{\Gamma} n^k \times (H_h - H^\eta_\varphi)\ell_i(x) dx \\ \int (\hat{\mu}\frac{\partial H_h}{\partial t} + \nabla \times E_h)\ell_i(x)\, dx = \quad & \int_{\partial \mathsf{D}^k \backslash \Gamma} n^k \times (E_h - E^*)\ell_i(x) dx. \end{aligned}$$

where H^η_φ is defined through $\varphi = n \times (H^\eta_\varphi \times n)$ and φ is obtained form the effective boundary conditions. Note also that $\int_\Gamma (n \times (E_h - E^*)\ell_i(x))\, dx = 0$, since we assume tangential continuity of E across the coating interface through $E_h = E^*$ along Γ.

To connect the elements away from the boundary we use a central flux as

$$E^* = \frac{1}{2}\left(E_h^- + E_h^+\right), \quad H^* = \frac{1}{2}\left(H_h^- + H_h^+\right),$$

where E_h^- refers to the interior solution and E_h^+ is the exterior solution. Other flux choices are possible and an extensive discussion can be found in [15].

5.3 One dimensional coatings

Let us first consider the one-dimensional case and assume that z is the direction of wave propagation. In this case the three-dimensional Maxwell's equations separate into two systems of tangential components with $E = [E_x, E_y]^T$ and $H = [H_x, H_y]^T$ on the form

$$\hat{\varepsilon}\frac{\partial E}{\partial t} = \hat{\sigma}\frac{\partial H}{\partial z}, \qquad \hat{\mu}\frac{\partial H}{\partial t} = -\hat{\sigma}\frac{\partial E}{\partial z}, \qquad \hat{\sigma} = \begin{bmatrix} 0 & -1 \\ 1 & 0 \end{bmatrix}.$$

In this simple case, the 2nd/3rd order effective boundary conditions are the same due to the planar boundary. They both reduce to

$$\frac{d\varphi}{dt} = \frac{1}{\eta}\hat{\sigma}E,$$

while the 4th/5th order effective boundary condition becomes

$$\frac{d\Phi}{dt} = \frac{1}{\eta}\hat{\sigma}E, \qquad \Phi + \frac{\eta}{3}\bar{\varepsilon}^{\eta}\frac{\partial^2\Phi}{\partial t^2} = \varphi$$

where, $\bar{\varepsilon}^{\eta} = \text{tr}\ \hat{\varepsilon}^{\eta} - \hat{\varepsilon}^{\eta}$.

For the 2nd and 3rd order scheme, any explicit or implicit scheme can be used for the time marching. However, an implicit scheme is needed for the 4th order scheme, since φ is not explicitly expressed as a function of the fields. However, only the element containing Γ need to be used for the implicit scheme, so the computational impact of this is minimal.

5.3.1 Internally coated cavity

We consider one-dimensional electromagnetic cavity with perfectly conducting walls located at $z^{(1)} = -1$ and $z^{(2)} = \eta$ as illustrated in Fig. 5.2. The interior of the cavity is filled with two dielectric media with the material interface at $z = 0$.

We consider the following general model

$$\begin{aligned}
\begin{bmatrix} \varepsilon_{xx} & \varepsilon_{xy} \\ \varepsilon_{yx} & \varepsilon_{yy} \end{bmatrix} \frac{\partial}{\partial t}\begin{bmatrix} E_x \\ E_y \end{bmatrix} &= \begin{bmatrix} 0 & -1 \\ 1 & 0 \end{bmatrix} \frac{\partial}{\partial z}\begin{bmatrix} H_x \\ H_y \end{bmatrix} \\
\frac{\partial}{\partial t}\begin{bmatrix} H_x \\ H_y \end{bmatrix} &= -\begin{bmatrix} 0 & -1 \\ 1 & 0 \end{bmatrix} \frac{\partial}{\partial z}\begin{bmatrix} E_x \\ E_y \end{bmatrix}
\end{aligned}$$

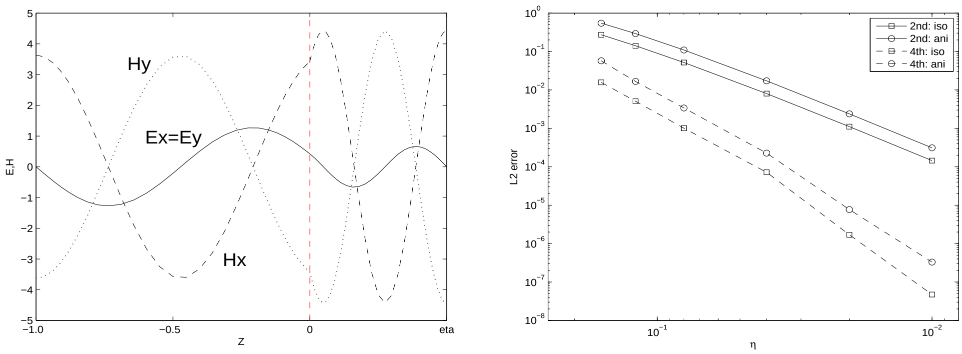

Figure 5.2: Initial condition for the cavity test case (left) and the convergence result (right) for the coated cavity problem. The solid line is the 2nd/3rd order effective boundary condition and the dashed line represents the 4th/5th order approximation. Squares are for an isotropic coating material with $\varepsilon^{\eta} = 2.25$ and circles represent an anisotropic coating material with $\varepsilon^{\eta}_{xx} = \varepsilon^{\eta}_{yy} = 4.0$, $\varepsilon^{\eta}_{xy} = \varepsilon^{\eta}_{yx} = 1.5$. The L_2-error is measured at $\mathrm{T} = \pi$.

reflecting a general anisotropic dielectric material but no magnetic effects. The boundary conditions are given as

$$\text{i)}\quad E = 0 \quad \text{or} \quad \frac{\partial H}{\partial z} = 0, \qquad \text{at} \quad z = -1, \eta$$

for the perfectly electrically conducting walls, and

$$\text{ii)}\quad E^{(1)} = E^{(2)}, \qquad H^{(1)} = H^{(2)}, \qquad \text{at} \quad z = 0,$$

to ensure tangential continuity across the material interface.

The solution of Maxwell's equations in this arrangement can be expressed as $(k = 1, 2)$

$$\begin{aligned}
E_x^{(k)} &= [A^{(k)} e^{in^{(k)}\omega z} - B^{(k)} e^{-in^{(k)}\omega z}] e^{i\omega t} \\
E_y^{(k)} &= [A^{(k)} e^{in^{(k)}\omega z} - B^{(k)} e^{-in^{(k)}\omega z}] e^{i\omega t} \\
H_x^{(k)} &= n^{(k)} [A^{(k)} e^{in^{(k)}\omega z} + B^{(k)} e^{-in^{(k)}\omega z}] e^{i\omega t} \\
H_y^{(k)} &= -n^{(k)} [A^{(k)} e^{in^{(k)}\omega z} + B^{(k)} e^{-in^{(k)}\omega z}] e^{i\omega t}
\end{aligned}$$

where

$$
\begin{aligned}
A^{(1)} &= \frac{n^{(2)}\cos\left(\eta n^{(2)}\omega\right)}{n^{(1)}\cos\left(n^{(1)}\omega\right)}, \qquad A^{(2)} = e^{-i\omega(n^{(1)}+\eta n^{(2)})} \\
B^{(1)} &= A^{(1)}e^{-i2n^{(1)}\omega}, \qquad B^{(2)} = A^{(2)}e^{i2\eta n^{(2)}\omega} \\
n^{(k)} &= \sqrt{\varepsilon_{xx}^{(k)}+\varepsilon_{xy}^{(k)}} = \sqrt{\varepsilon_{yy}^{(k)}+\varepsilon_{xy}^{(k)}},
\end{aligned}
$$

and we require $\varepsilon_{xx}^{(k)} = \varepsilon_{yy}^{(k)}$ for simplicity. Here ω is the solution to the equation

$$
-n^{(2)}\tan\left(n^{(1)}\omega\right) = n^{(1)}\tan\left(\eta n^{(2)}\omega\right)
$$

In Fig. 5.2 and Table 5.1 we illustrate the 2nd/3rd and 4th/5th order convergence of effective boundary conditions as a function of η, measured in terms of free-space wave lengths. Both for the isotropic and the more complex anisotropic case do we recover approximate design order convergence rates.

η		0.16	0.12	0.08	0.04	0.02	0.01
Isotropic material inside thin layer							
EBC 2nd/3rd		2.74e-01	1.42e-01	5.17e-02	8.03e-03	1.11e-03	1.45e-04
	order		2.29	2.48	2.69	2.85	2.94
EBC 4th/5th		1.57e-02	5.07e-03	1.01e-03	7.20e-05	1.70e-06	4.73e-08
	order		3.93	3.97	3.81	5.41	5.16
Anisotropic material inside thin layer							
EBC 2nd/3rd		5.47e-01	2.94e-01	1.10e-01	1.72e-02	2.39e-03	3.11e-04
	order		2.16	2.43	2.67	2.85	2.94
EBC 4th/5th		5.73e-02	1.67e-02	3.40e-03	2.27e-04	7.69e-06	3.30e-07
	order		4.29	3.92	3.91	4.88	4.54

Table 5.1: L_2-convergence rates for the effective boundary condition (EBC) of 2nd/3rd and 4th/5th order are shown for the test case shown in Fig. 5.2.

5.3.2 Comparison with brute-force computations

We consider the situation shown in Fig. 5.3 in which a general pulse impinges on a thinly coated metallic wall while on the left is a simple absorbing layer. A pulse is sent toward the coating and we compare the brute-force results – referred to

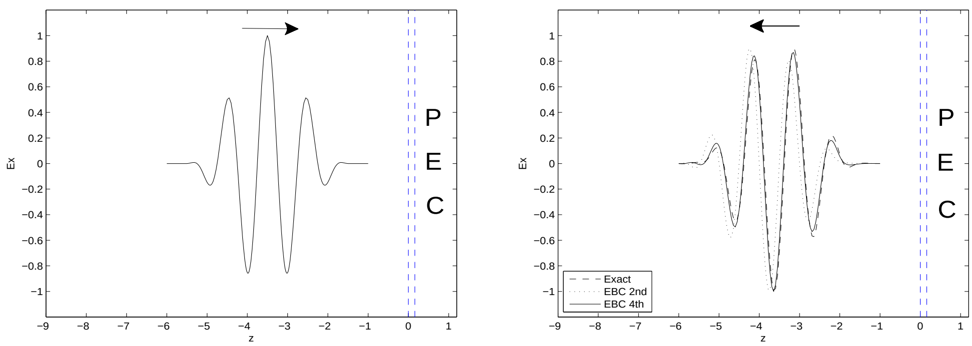

Figure 5.3: The initial condition of E_x (left) and reflected value of E_x (right) from the brute-force computation with a thin layer of isotropic material (dashed line), from using a 2nd/3rd order effective boundary conditions (dotted line), and from using a 4th/5th order effective boundary condition (solid line). The thickness of the thin layer is $\eta = 0.16$ and the isotropic material is assume to have $\hat{\varepsilon}^{\eta} = 1.5I$.

as the 'exact computation' – with the results obtained by using the thin coating effective boundary conditions. In Fig. 5.3, the results obtained by using the 2nd/3rd order and the 4th/5th order effective boundary conditions are displayed. It is particularly noteworthy how much improvement there is in the accuracy of the phase error when increasing the order of the approximation. The left of Fig. 5.4 and Table 5.2 also confirms the expected convergence order of the effective boundary condition.

The real benefit of the effective boundary condition is found in the potential for a dramatically reduced computational time as compared to the brute-force computation using an explicit time marching scheme such as Runge Kutta 4th order. For the brute-force approach, the stable timestep is proportional to η. In contrast to this, the stable timestep for the effective boundary condition shows no dependence of η as shown in Fig. 5.4. This yields a reduction in computational effort proportional to η^{-1} without compromising the accuracy.

5.4 Two-dimensional coatings

One of the unique features of the effective boundary conditions considered here is the ability to correctly account for curvature of the metallic backing. To explore

η	0.20	0.16	0.12	0.08	0.04
Isotropic material inside thin layer					
EBC	2.41e-01	1.68e-01	8.48e-02	2.67e-02	3.19e-03
2nd/3rd	order	2.37	2.85	3.06	3.06
EBC	4.93e-02	2.43e-02	7.02e-03	9.20e-04	2.51e-05
4th/5th	order	4.31	5.01	5.20	5.10
Anisotropic material inside thin layer					
EBC	2.32e-01	1.94e-01	1.07e-01	3.21e-02	3.63e-03
2nd/3rd	order	2.08	2.97	3.15	3.08
EBC	8.35e-02	4.01e-02	1.42e-02	1.75e-03	4.22e-05
4th/5th	order	3.60	5.17	5.37	5.17

Table 5.2: L_2-convergence rates for the effective boundary condition (EBC) of 2nd/3rd and 4th/5th order are shown for the test case shown in Fig. 5.3. The material properties of the isotropic material and the anisotropic materials are given as $\hat{\varepsilon}^\eta = 1.5I$ and $\varepsilon^\eta_{xx} = \varepsilon^\eta_{yy} = 1.5$, $\varepsilon^\eta_{xy} = \varepsilon^\eta_{yx} = 0.75$, respectively. The L_2-error is measured at T = 10.0.

this, let us consider the two-dimensional Maxwell's equations for TE polarization in the (x, y)-plane

$$\begin{aligned}\hat{\varepsilon}\frac{\partial E}{\partial t} &= -\hat{\sigma}\nabla H_z \\ \hat{\mu}\frac{\partial H_z}{\partial t} &= (\nabla \times E)\cdot z\end{aligned}$$

where $E = [E_x, E_y]^T$ and z reflects a unit vector along the z-axis. In this polarization, the effective 2nd order boundary condition becomes

$$\left(\frac{\partial E}{\partial t} \times n\right)\cdot z = -\eta\mu^\eta\frac{\partial^2\varphi_z}{\partial t^2} + \frac{\eta}{\varepsilon_r^\eta}\mu^\eta\frac{\partial^2\varphi_z}{\partial x_\Gamma^2}, \qquad x \in \Gamma,$$

where the general case reduces since $\varphi_z = H_z$. In the form of a system of equations,

$$\begin{aligned}(E\times n)\cdot z &= -\eta\mu^\eta\frac{\partial\varphi_z}{\partial t} - \eta\mu^\eta\frac{\partial\zeta_z}{\partial x_\Gamma} \\ \frac{\partial\zeta_z}{\partial t} &= -\frac{1}{\varepsilon_r^\eta}\frac{\partial\varphi_z}{\partial x_\Gamma}\end{aligned}$$

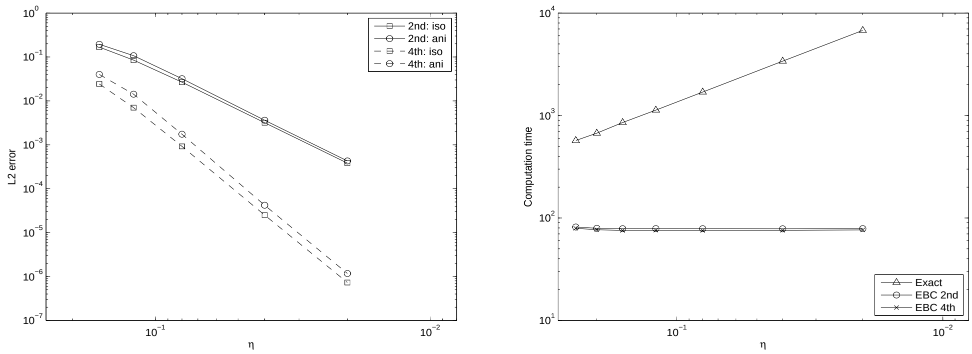

Figure 5.4: L_2 error convergence rate (left) of 2nd/3rd order effective boundary condition for isotropic (solid line with squares) and anisotropic (solid line with circles) materials, and the results for the 4th/5th order effective boundary condition for isotropic(dashed line with squares), anisotropic (dashed line with circle) materials. Permittivity constants are $\hat{\varepsilon}^\eta = 1.5$ for isotropic material and $\varepsilon^\eta_{xx} = \varepsilon^\eta_{yy} = 1.5$, $\varepsilon^\eta_{xy} = \varepsilon^\eta_{yx} = 0.75$ for anisotropic material. On the right we show the computational time for the brute-force/exact computation (triangles), for the 2nd/3rd order effective boundary condition (circle), and for the 4th/5th order effective boundary condition (cross), showing the independence of the work on thickness of the coating.

and $\frac{\partial}{\partial x_\Gamma}$ refers to differentiation along the surface of the coating Γ.

The 3rd order accurate effective boundary condition becomes

$$\left(\frac{\partial E}{\partial t} \times n\right) \cdot z = -\eta\mu^\eta[1 - \eta(\mathcal{C} - \mathcal{H})]\frac{\partial^2 \varphi_z}{\partial t^2} + \frac{\eta}{\varepsilon^\eta_r}\mu^\eta \frac{\partial}{\partial x_\Gamma}\left([1 - \eta\mathcal{H}]\frac{\partial \varphi_z}{\partial x_\Gamma}\right).$$

In the form of a system of equations,

$$\begin{aligned} (E \times n) \cdot z &= -\eta\mu^\eta[1 - \eta(\mathcal{C} - \mathcal{H})]\frac{\partial \varphi_z}{\partial t} - \eta\mu^\eta \frac{\partial \varphi_z}{\partial x_\Gamma} \\ \frac{\partial \zeta_z}{\partial t} &= -\frac{1}{\varepsilon^\eta_r}[1 - \eta\mathcal{H}]\frac{\partial \zeta_z}{\partial x_\Gamma}. \end{aligned}$$

Here, $\mathcal{C}$ is the curvature tensor and $\mathcal{H}$ is the mean curvature of the metallic backing for the coating. For an isotropic material ε^η is simply a constant such that $\hat{\varepsilon}^\eta = \varepsilon I$ and for an anisotropic material it is a constant such that $(\hat{\varepsilon}^\eta E) \cdot n = \varepsilon^\eta_r(E \cdot n)$, where $\hat{\varepsilon}$ indicates the permittivity tensor and I is the 2-identity matrix.

As a measure of accuracy, we shall use the radar cross section and generally compare the brute-force computation of this with the result obtained using the effective boundary condition. The radar cross section (RCS) is defined as [33]

$$F(\varphi) \equiv \frac{e^{i(\pi/4)}}{\sqrt{8\pi k}} \oint_{C_a} \left[\omega\mu_0 \hat{z}' \cdot \breve{J} - kz' \times \breve{M}(r') \cdot \hat{r}\right] e^{ik\hat{r}\cdot r'} dC$$
$$\mathrm{RCS}(\varphi) \equiv 2\pi \frac{|F(\varphi)|^2}{|E_{inc}|^2}$$

where $\breve{J} = n \times H$ and $\breve{M} = -n \times E$ are the equivalent magnetic and electric currents on the surface C_a which completely encloses the scatterer. k and ω is the wave number and the frequency, respectively, of the illuminating plane wave; $r = R\cos\varphi$ is the far-field observation point and r' is the near-field source point in C_a.

5.4.1 Scattering by smooth coated cylinders

Let us first consider the most straightforward case of scattering by a two-dimensional cylinder with a smooth cross section. In this case, the derivation and assumptions of the effective boundary conditions are fulfilled and we should expect design order convergence.

5.4.1.1 Circular cylinder

We first consider a thinly-coated circular cylinder which is infinitely long along the z axis. Let R be the radius of the metallic cylinder and η be the constant thickness of the thin coating. Then, the curvature tensor is $\mathcal{C} = -\frac{1}{R+\eta}\tau$ and the mean curvature is $\mathcal{H} = -\frac{1}{2(R+\eta)}$, where τ is the tangential direction along the coating surface Γ.

In the right of Fig. 5.5 we show the convergence of the RCS using the 2nd and 3rd order effective boundary condition. We note in particular the improved accuracy of the 3rd order condition for this case.

The actual convergence rates for the RCS is shown in Table 5.3 for both the 2nd and 3rd order effective boundary conditions for isotropic and anisotropic cases, showing close to design order accuracy when decreasing the thickness of the coating.

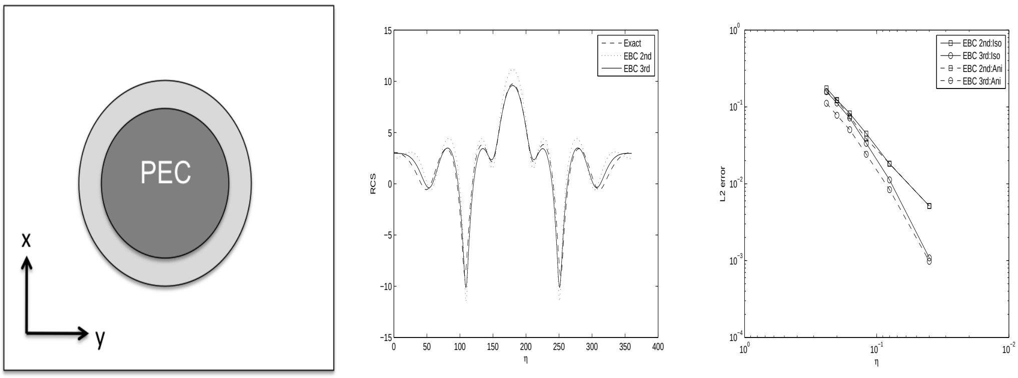

Figure 5.5: Radar cross section (RCS) of the brute force computation(dashed line), 2nd (dotted line) and 3rd (solid line) order effective boundary conditions for a circular cylinder with $\eta = 0.12\lambda$ are compared (left). λ is the wavelength of the incident wave. Also, L_2-errors of the 2nd (square-solid line) and the 3rd (circle-solid line) order approximation for isotropic material with $\varepsilon^\eta = 1.5$ for anisotropic materials with $\varepsilon^\eta_{xx} = \varepsilon^\eta_r n_x^2 + 1,\ \varepsilon^\eta_{xy} = \varepsilon^\eta_{yx} = \varepsilon^\eta_r n_x n_y,\ \varepsilon^\eta_{yy} = \varepsilon^\eta_r n_y^2 + 1, \varepsilon^\eta_r = 1.5$ are shown.

5.4.1.2 Elliptic cylinder

As a sligthly more complex case, we consider a coated elliptic cylinder. Let a and b be the major and minor axis of the ellipsoid of the contour of Γ^v with the the thickness of thin layer being η. Note that the contour of the interface $\partial\Omega$ at the distance of η from Γ^v in the normal direction is not an ellipsoid.

The curvature tensor is given as

$$\mathcal{C} = -\frac{ab}{(a^2\cos^2 t + b^2\sin^2 t)^{3/2}}\tau,$$

and the mean curvature is

$$\mathcal{H} = -\frac{ab}{2(a^2\cos^2 t + b^2\sin^2 t)^{3/2}},$$

where $t = \tan^{-1}\left(\frac{a}{b}\frac{y}{x}\right)$.

In the right of Fig. 5.6 we show the convergence of the RCS when using the 2nd and 3rd order effective boundary condition. We note in particular the improved accuracy of the 3rd order condition for this case.

η	0.20	0.16	0.12	0.08	0.04
Isotropic material inside thin layer					
EBC 2nd	1.23e-01	8.24e-02	4.50e-02	1.82e-02	5.14e-03
	order	1.27	1.78	2.21	2.37
EBC 3rd	1.12e-01	7.18e-02	3.36e-02	1.12e-02	1.08e-03
	order	2.01	2.64	2.71	3.37
Anisotropic material inside thin layer					
EBC 2nd	1.22e-01	7.53e-02	3.86e-02	1.83e-02	5.13e-03
	order	1.37	2.15	1.71	2.40
EBC 3rd	7.79e-02	5.05e-02	2.42e-02	8.38e-03	9.80e-04
	order	1.94	2.56	2.61	3.10

Table 5.3: Convergence rate for the L_2-error of the RCS for the 2nd and 3rd order effective boundary conditions (EBC) for the circular cylinder. Material constants are the same as given in Fig. 5.5

The actual convergence rates for the RCS is shown in Table 5.4 for both the 2nd and 3rd order effective boundary conditions for the isotropic and the anisotropic cases, confirming close to design order accuracy when decreasing the thickness of the coating.

5.4.2 Frequency dependence of the coating performance

While it is of primary interest to understand the performance of the thin coating approximation for very thin coatings, it is of practical importance to also understand when the approximation breaks down as the thickness of the layer increases.

We consider the same examples as in the above and fix the physical dimensions of the smooth scatterer while the frequency of the incident wave is changed. In Fig. 5.7 we show the accuracy of the approximation for both 2nd and 3rd order effective boundary conditions for the cylindrical and elliptic case. The generel trends are the same in both cases. For increasing frequency, the layer gets electrically thicker and the accuracy of the thin layer approximation deteriorates as one would expect. Extensive numerical tests show that when the coating

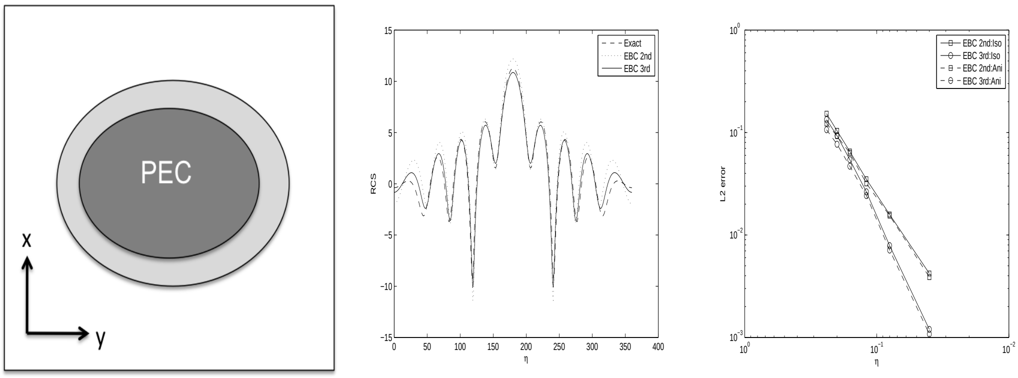

Figure 5.6: Radar cross section (RCS) of the brute force computation(dashed line), 2nd (dotted line) and 3rd (solid line) order effective boundary conditions for an elliptic cylinder with $\eta = 0.12\lambda$ are compared (left). λ is the wavelength of the incident wave. Major axis and minor axis of Γ is $(0.8 + \eta)\lambda$ and $(0.5 + \eta)\lambda$, respectively. Also, L_2-errors of the 2nd (square-solid line) and the 3rd (circle-solid line) order approximation for isotropic material with $\varepsilon^{\eta} = 1.5$ for anisotropic materials with $\varepsilon^{\eta}_{xx} = \varepsilon^{\eta}_{r} n_x^2 + 1,\ \varepsilon^{\eta}_{xy} = \varepsilon^{\eta}_{yx} = \varepsilon^{\eta}_{r} n_x n_y,\ \varepsilon_{yy} = \varepsilon^{\eta}_{r} n_y^2 + 1, \varepsilon^{\eta}_{r} = 1.5$ are shown.

gets close to one wavelength thick, the approximation slowly fails. However, in that limit, the layer is no longer electrically thin and poses much less of a computational bottleneck.

Figure 5.7 shows another interesting difference between the two formulations. Recall that the 3rd order conditions depend on the geometric parameters such as the curvature tensor ($\mathcal{C}$) and the mean curvature ($\mathcal{H}$), while the 2nd order condition neglects this information. As we have discussed previously, when the boundary is plane, the two conditions are equivalent. However, for the examples considered here, we see a dramatic difference when decreasing the frequency of the illuminating wave while in the high-frequency limit the two schemes behave in similar ways. In the latter case, the curvature over a wavelength is very small and the two schemes behave as if the boundary is approximately plane. In the other limit, however, the curvature of the boundary over a wavelength is much more pronounced and including it in the effective boundary condition improves the accuracy of the results significantly.

η		0.20	0.16	0.12	0.08	0.04
Isotropic material inside thin layer						
EBC 2nd	1.04e-01	6.54e-02	3.51e-02	1.59e-02	4.21e-03
	order	1.04	1.32	2.00	2.36
EBC 3rd	9.32e-02	5.43e-02	2.64e-02	7.87e-03	1.20e-03
	order	2.41	2.51	2.98	2.72
Anisotropic material inside thin layer						
EBC 2nd	9.27e-02	6.31e-02	3.19e-02	1.54e-02	3.88e-03
	order	2.46	3.06	0.58	1.99
EBC 3rd	7.70e-02	4.69e-02	2.43e-02	7.13e-03	1.08e-03
	order	2.22	2.30	3.02	2.72

Table 5.4: Convergence rate for the L_2-error of the RCS for the 2nd and 3rd order effective boundary conditions (EBC) for the elliptic cylinder. Conditions are the same as in Fig. 5.6

5.4.3 Extension to objects with a non-smooth boundary

The effective boundary conditions are derived under the assumption that the metallic backing is smooth, although, in contrast to most alternatives, the formulation does allow for high curvature. However, for most applications, corners and edges introduce points where the smoothness assumption breaks down and the rigor of the derivation of the models must be relaxed. Nevertheless, it is of considerable interest to explore the performance of the effective boundary conditions in this case also to gauge the impact of this violation of the smoothness assumption.

In Fig. 5.8, we show the difference in the RCS for an infinite cylinder with a square cross section and a thin coating of isotropic material of thickness. Since the cylinder has plane sides, the 2nd and 3rd order scheme are equivalent and the difference between the brute-force computation and the results using the effective boundary conditions can only be attributed to the difficulty of dealing with nonsmooth boundaries. Another violation results from the observation that when the boundary of the object contains singular points, the thickness of the thin layer has to vary at those points, i.e., the thickness can not be constant on all of Γ. This is further illustrated in Fig. 5.8 where the difference between the

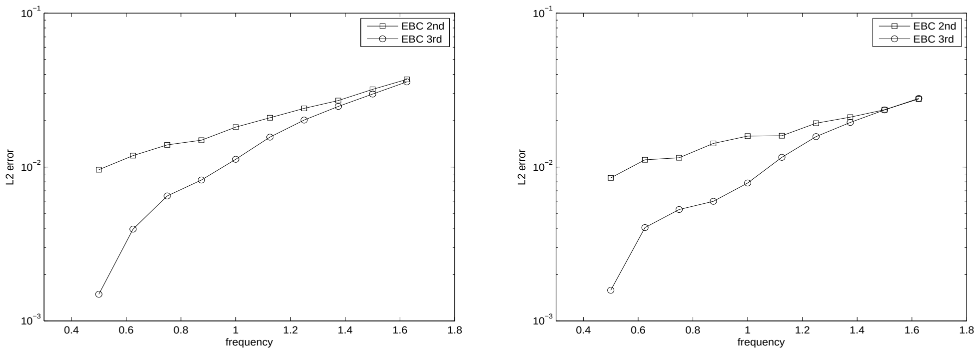

Figure 5.7: L_2-errors for the RCS versus normalized frequency of incident waves for the circular cylinder (left) and the elliptic cylinder (right) using 2nd and 3rd order effective boundary conditions. The material coefficents for the thin coating are $\varepsilon^\eta = 2.25$ and the thickness is 0.08

brute-force computation and the thin layer approximation clearly highlights the regions with the corners as the main regions of error.

One way to address this problem is to take advantage of the ability of the effective boundary conditions to handle smooth regions of high curvature and simply substitute the singular points by geometrically similar, but smooth surfaces. For example, for the vertex of rectangles, one can smoothen them out into small rounded corner. In Figs. 5.9 and 5.10, we illustrate the result of this approach for the problem consider in Fig. 5.8. As expected, the 3rd order condition is now clearly superior to the 2nd order condition due to the area of high curvature being introduced. However, the overall improvement in the agreement of the RCS is rather dramatic and key measures such as the back- and forward scattering is now in agreement with the brute-force results.

It should be noted that the test in Fig. 5.8 is a severe challenge to the effective boundary conditions due to the small electric size of the square. For electrically larger problems where the separation between the non-smooth points is larger, the impact of these on the performance of the thin layer models is dramatically reduced.

Also, Fig. 5.11 shows the RCS of thin layer approximation of smoothed rectangular cylinder converges to RCS of the exact computation of rectangular cylinder as the radius of small circles at the vertex decreases.

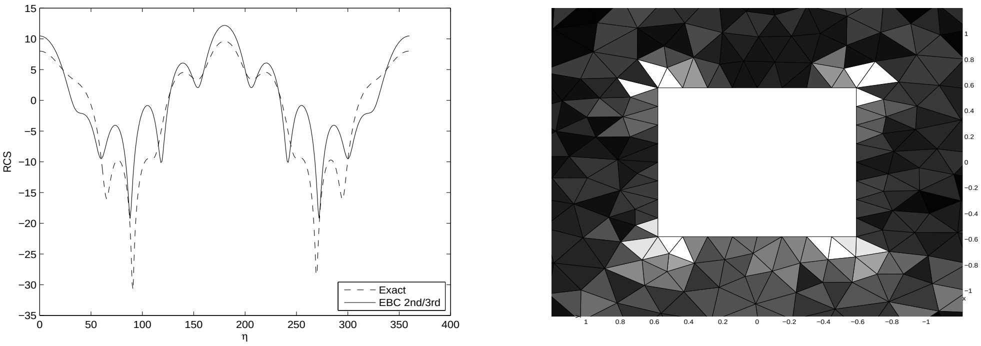

Figure 5.8: Radar cross section of the brute-force computation (dashed line) and 2nd order effective boundary condition(solid line) on a rectangular cylinder on the left. On the right, we show the distribution of error of E when the thin layer with thickness $\eta = 0.08\lambda$ consists of an isotropic material with $\varepsilon^{\eta} = 2.25$. The brighter the area is, the higher the local error is. The brightest color corresponds to the magnitude of 0.8 and the darkest is close to zero.

5.5 Remarks and extensions

We have continued the development of a new family of high-order order accurate thin layer models, first proposed in [13] for isotropic materials, for time-domain electromagnetics and discussed its implementation in a discontinuous Galerkin scheme. This allows us to validate the schemes for both one- and two-dimensional cases and to extend the‘ formulation to general anisotropic materials. The tests confirm design order accuracy and the significant advantages in terms of computational efficiency and overall accuracy of using a high-order effective boundary conditions. This is found to be particularly true for problem with high curvature.

While the analysis only covers the case of smooth metallic coated objects, we pursued the extension to non-smooth scatterers by computational means and showed that it is reasonable, with minor modifications, to expect a good accuracy also in this case.

In this chapter, we have discussed general anisotropic but homogeneous layers. However, the extension of the isotropic case to multi-layered coatings is outlined in [13] and the generalization of the methods discussed here for anisotropic coatings can be achieved following the same approach as for the isotropic case.

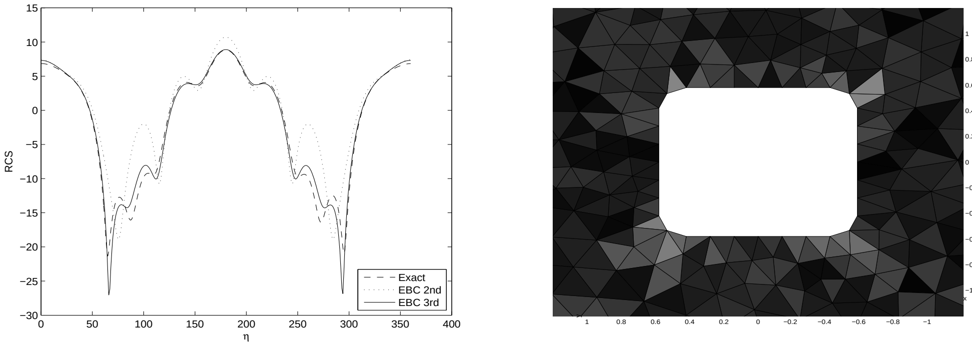

Figure 5.9: Radar cross section of the brute-force computation (dashed line) and 2nd order (dotted line) and the 3rd order (solid line) effective boundary condition on a rectangular cylinder with smoothed corners shown on the left. On the right we show the distribution of the error of E when the thin layer with thickness $\eta = 0.08\lambda$ consists of an isotropic material with $\varepsilon^{\eta} = 2.25$. The same scaling on color as in Fig. 5.8 is used for comparison

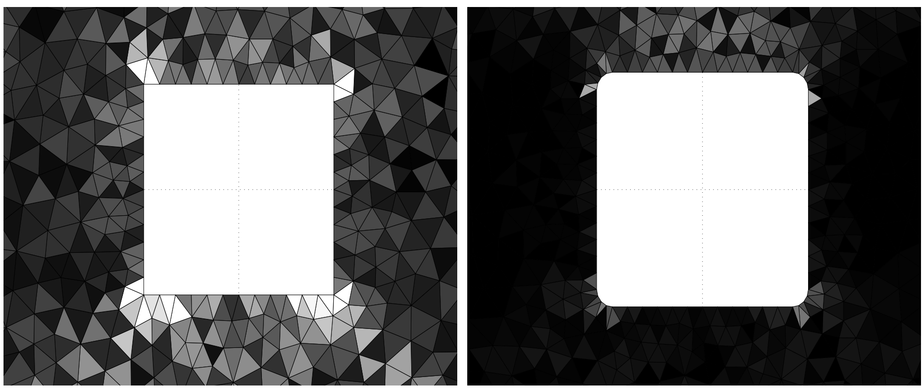

Figure 5.10: Distribution of error of E when the size of rectangular cylinder (left) and smoothed rectangular cylinder (right) are larger (width and height are 2λ long) are shown. Material properties and the thickness are the same as the previous case. The maximum error of rectangular cylinder is around 1.5 and smoothed cylinder is 0.3 when $T = 5\pi$

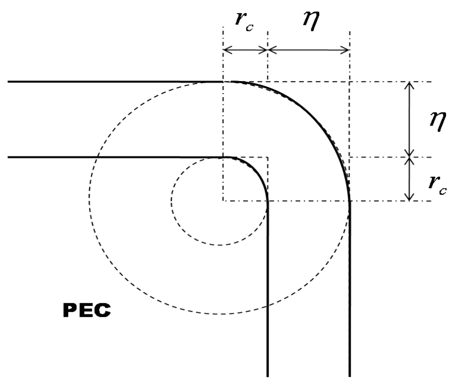

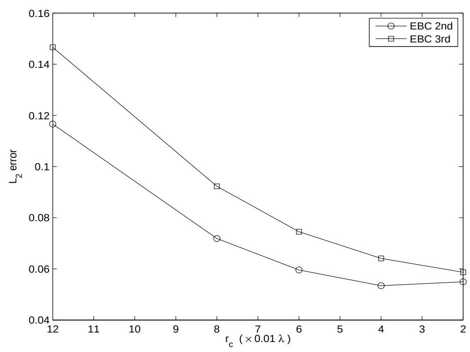

Figure 5.11: Construction of smoothed rectangular cylinder (left) and RCS errors between the exact computation of rectangular cylinder and the EBC 2nd (circle)/EBC 3rd (rectangle) approximation of smoothed rectangular cylinder (right) are shown. As the radius of circle r_c decreases, RCS of smoothed rectangular cylinder by thin layer approximation converges to RCS of original rectangular cylinder by the exact computation.

In the next chapter, we shall discuss a more extensive generalization to include transission layers and high-order effective boundary conditions for such cases where both reflection and transmission has to be dealt with accurately.

Chapter 6

Thin layer approximations for time-domain electromagnetics: Part II: Transmission layers

In this chapter, the thin layer formulation of 3rd order and 5th order for curvilinear transmission layers are derived by means of an asymptotic expansion. The implementation of these approximations in the context of discontinuous Galerkin method are studied for curvilinear transmission layers of isotropic and tangentially-aligned anisotropic materials. The range of validity, accuracy, and stability of the resulting schemes are demonstrated through one and two dimensional examples.

The remaining part of this chapter is organized as follows. In section 6.1, the general formulations of the thin layer approximation for transmission layers are derived. In section 6.2, we show how these formulations are implemented in discontinuous Galerkin method. The details of the one dimensional scheme and computational results are demonstrated in section 6.3 with a realistic application to the modeling periodic magnetic crystals. The two dimensional scheme and computational results along with an example of the dramatic improvements for the computation of curvilinear thin layer objects follows in section 6.4 while concluding remarks are given in section 6.5.

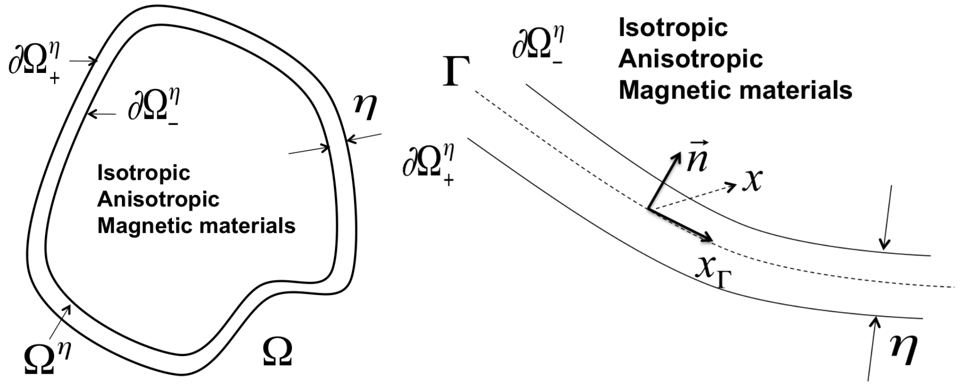

Figure 6.1: On the left we summarize the definitions of the domains and the boundaries and on the right we show the local coordinate system used along the smooth boundary.

6.1 Formulations of the interface conditions

Let's consider a thin layer (Ω^η) of thickness of η in the domain Ω. Let $\partial\Omega^\eta_+$, and $\partial\Omega^\eta_-$ be the outer and inner boundary of the thin layer, respectively and Γ be defined as $\Gamma = \frac{1}{2}(\partial\Omega^\eta_+ + \partial\Omega^\eta_-)$, i.e., the parallel interface located half way between the two boundaries (see Fig. 6.1). Note when normal vector $\vec{n}$ is given on Γ, the outer and inner boundaries of Ω^η can be expressed as $\Gamma \pm (\eta/2)\vec{n}$. Let E^η, H^η be the electric, magnetic fields, and $\hat{\varepsilon}^\eta$, $\hat{\mu}^\eta$ be the permittivity and permeability tensor respectively in the thin layer Ω^η. Also, let E, H be the electric, magnetic fields and $\hat{\varepsilon}$, $\hat{\mu}$ be the permittivity and permeability tensor in the domain $\Omega_v(\equiv \Omega\backslash\Omega^\eta)$. Then, the problem is described by Maxwell's equations,

$$\hat{\varepsilon}\frac{\partial E}{\partial t} - \nabla \times H = 0, \quad \hat{\mu}\frac{\partial H}{\partial t} + \nabla \times E = 0 \qquad \text{on} \;\; \Omega\backslash\Omega^\eta \tag{6.1}$$

$$\hat{\varepsilon}^\eta\frac{\partial E^\eta}{\partial t} - \nabla \times H^\eta = 0, \quad \hat{\mu}^\eta\frac{\partial H^\eta}{\partial t} + \nabla \times E^\eta = 0 \qquad \text{on} \;\; \Omega^\eta \tag{6.2}$$

with boundary conditions

$$E \times \vec{n} = E^\eta \times \vec{n}, \quad H \times \vec{n} = H^\eta \times \vec{n}, \qquad \text{on} \;\; \partial\Omega^\eta_+ \cup \partial\Omega^\eta_- \tag{6.3}$$

We aim to construct interface conditions connecting the tangential components of $(E,\ H)$ on $\partial\Omega_+$ with the tangential components of $(E,\ H)$ on $\partial\Omega_-$. In other words, we seek the following interface conditions of order k

$$E_+ \times \vec{n} = \mathcal{B}_E^k(\vec{n} \times (H_- \times \vec{n}))$$
$$H_+ \times \vec{n} = \mathcal{B}_H^k(\vec{n} \times (E_- \times \vec{n}))$$

where, $(E_-,\ H_-) = \{(E,\ H) \text{ on } \partial\Omega_-^\eta\}$ and $(E_+,\ H_+) = \{(E,\ H) \text{ on } \partial\Omega_+^\eta\}$. Similar to the thin coating approximation discussed in chapter 5, we express the grid points x in Ω^η such as

$$x = x_\Gamma + s \cdot \vec{n} = x_\Gamma + \eta\nu\vec{n}, \quad x_\Gamma \in \Gamma,\ \nu \in \left[-\frac{1}{2}, \frac{1}{2}\right]$$

and consider the expansion of $E^\eta,\ H^\eta$

$$\begin{matrix} E^\eta(x,t) = E_0^\eta(x_\Gamma,\nu,t) + \eta E_1^\eta(x_\Gamma,\nu,t) + \eta^2 E_2^\eta(x_\Gamma,\nu,t) + \cdots \\ H^\eta(x,t) = H_0^\eta(x_\Gamma,\nu,t) + \eta E_1^\eta(x_\Gamma,\nu,t) + \eta^2 H_2^\eta(x_\Gamma,\nu,t) + \cdots \end{matrix}, \quad x \in \Omega^\eta \quad (6.4)$$

Note $E_k^\eta,\ H_k^\eta$ is independent of η by its construction. Along x_Γ, the differential operator ∇ is

$$\nabla = \nabla_\Gamma + \frac{1}{\eta}\frac{\partial}{\partial\nu}$$

and the curl operator $\nabla\times$ as

$$\nabla \times V = \mathcal{T}_\Gamma^s V - \frac{1}{\eta}\frac{\partial}{\partial\nu}(V \times \vec{n})$$

where, $\mathcal{T}_\Gamma^s V = [(\mathcal{R}_s\nabla_\Gamma) \cdot (V \times \vec{n})]\vec{n} + [\mathcal{R}_s\nabla_\Gamma(V \cdot \vec{n})] \times \vec{n} - (\mathcal{R}_s\mathcal{C}V) \times \vec{n}$ and $\mathcal{C} = \vec{\nabla}\vec{n}$ is the curvature tensor, while $\mathcal{R}_s(\Pi_{||} + s\mathcal{C}) = \Pi_{||}$ is the projection operator along the tangential direction of Γ (see [13] for detailed proof). By inserting the above expansion into Eq. (6.2), we obtain

$$\hat{\varepsilon}^\eta\frac{\partial E^\eta}{\partial t} - \mathcal{T}_\Gamma^s H^\eta + \frac{1}{\eta}\frac{\partial}{\partial\nu}(H^\eta \times \vec{n}) = 0 \quad (6.5)$$

$$\hat{\mu}^\eta\frac{\partial H^\eta}{\partial t} + \mathcal{T}_\Gamma^s E^\eta - \frac{1}{\eta}\frac{\partial}{\partial\nu}(E^\eta \times \vec{n}) = 0 \quad (6.6)$$

With the Taylor expansion of $\mathcal{R}_s$, $\mathcal{R}_s = \Pi_{||} + \sum_{i=1}^\infty(-\eta\nu\mathcal{C})^i$, we have the following expansion of $\mathcal{T}_\Gamma^s$,

$$\mathcal{T}_\Gamma^{\eta\nu} = \sum_{i=0}^\infty(-\eta\nu)^i\mathcal{T}_\Gamma^i \quad (6.7)$$

where, $\mathcal{T}_\Gamma^i V = [(\mathcal{C}^i\nabla_\Gamma)\cdot(V\times\vec{n})]\vec{n} + [\mathcal{C}^i\nabla_\Gamma(V\cdot\vec{n})]\times\vec{n} - (\mathcal{C}^{i+1}V)\times\vec{n}$. Substituting Eqs. (6.4) and (6.7) into Eqs. (6.5) and (6.6), we obtain the following equations for $k=0$,

$$\frac{\partial}{\partial\nu}(E_0^\eta\times\vec{n}) = 0, \quad \frac{\partial}{\partial\nu}(H_0^\eta\times\vec{n}) = 0 \tag{6.8}$$

and for $k\geq 1$,

$$\begin{aligned}
\hat{\varepsilon}^\eta\frac{\partial E_{k-1}^\eta}{\partial t} - \sum_{i=1}^{k-1}(-\nu)^{k-i}\mathcal{T}_\Gamma^{k-i}H_i^\eta + \frac{\partial}{\partial\nu}(H_k^\eta\times\vec{n}) = 0\\
\hat{\mu}^\eta\frac{\partial H_{k-1}^\eta}{\partial t} + \sum_{i=0}^{k-1}(-\nu)^{k-1}\mathcal{T}_\Gamma^{k-i}E_i^\eta - \frac{\partial}{\partial\nu}(E_k^\eta\times\vec{n}) = 0
\end{aligned}$$

Separating the tangential components and the normal components with respect to Γ in the above equations, we have the tangential components for $k\geq 1$.

$$\begin{aligned}
\frac{\partial}{\partial\nu}(H_k^\eta\times\vec{n}) = -\hat{\varepsilon}^\eta\frac{\partial(E_T)_{k-1}^\eta}{\partial t} &+ \sum_{i=0}^{k-1}(-\nu)^{k-i}\vec{\nabla}_\Gamma^{k-i}\times(H_i^\eta\cdot\vec{n})\\
&- \sum_{i=0}^{k-1}(-\nu)^{k-i}(\mathcal{C}^{k-i}(H_T)_i^\eta)\times\vec{n}
\end{aligned} \tag{6.9}$$

$$\begin{aligned}
\frac{\partial}{\partial\nu}(E_k^\eta\times\vec{n}) = \hat{\mu}^\eta\frac{\partial(H_T)_{k-1}^\eta}{\partial t} &+ \sum_{i=0}^{k-1}(-\nu)^{k-i}\vec{\nabla}_\Gamma^{k-i}\times(E_i^\eta\cdot\vec{n})\\
&- \sum_{i=0}^{k-1}(-\nu)^{k-i}(\mathcal{C}^{k-i}(E_T)_i^\eta)\times\vec{n}
\end{aligned} \tag{6.10}$$

and the normal components for $k\geq 1$

$$\mu_f^\eta(H_{k-1}^\eta\cdot\vec{n}) = -\sum_{i=0}^{k-1}(-\nu)^{k-i}\nabla_\Gamma^{(k-i)}\times(E_i^\eta)_T \tag{6.11}$$

$$\varepsilon_f^\eta(E_{k-1}^\eta\cdot\vec{n}) = \sum_{i=0}^{k-1}(-\nu)^{k-i}\nabla_\Gamma^{(k-i)}\times(H_i^\eta)_T \tag{6.12}$$

where, $\varepsilon_f^\eta, \mu_f^\eta$ is a scalar constant satisfying $\left(\hat{\varepsilon}^\eta E_{k-1}^\eta\right)\cdot\vec{n} = \varepsilon_f^\eta(E_{k-1}^\eta\cdot\vec{n})$, $\left(\hat{\mu}^\eta H_{k-1}^\eta\right)\cdot\vec{n} = \mu_f^\eta(H_{k-1}^\eta\cdot\vec{n})$ and $\vec{\nabla}_\Gamma^i\times v = (\mathcal{C}^i\nabla_\Gamma v)\times\vec{n}$, $\nabla_\Gamma^i V = (\mathcal{C}^i\nabla_\Gamma)\cdot(V\times\vec{n})$, $\mathcal{C}=$ curvature tensor and $V_T\equiv\vec{n}\times(V\times\vec{n})$. Effective Interface conditions(EIC) of order $k+1$

are obtained by solving Eqs. (6.8)-(6.12) up to k. For example, the 2nd/3rd order EIC is given as

$$
\boxed{\begin{array}{l}
\left\{\begin{array}{l}
[E\times\vec{n}] = \eta\left(\hat{\mu}^{\eta}\frac{\partial\langle H_T\rangle}{\partial t} + \vec{\nabla}_\Gamma\times\varphi^\eta - (\mathcal{C}\langle E_T\rangle)\times\vec{n}\right)\\
\varepsilon_f^\eta\frac{\partial\varphi^\eta}{\partial t} = \nabla_\Gamma\times\langle H_T\rangle
\end{array}\right.\\
\\
\left\{\begin{array}{l}
[H\times\vec{n}] = -\eta\left(\hat{\varepsilon}^{\eta}\frac{\partial\langle E_T\rangle}{\partial t} - \vec{\nabla}_\Gamma\times\psi^\eta + (\mathcal{C}\langle H_T\rangle)\times\vec{n}\right)\\
\mu_f^\eta\frac{\partial\psi^\eta}{\partial t} = -\nabla_\Gamma\times\langle E_T\rangle
\end{array}\right.
\end{array}} \tag{6.13}
$$

where, $[V] = V_+ - V_-$, $\langle V\rangle = \frac{1}{2}(V_+ + V_-)$ and $V_\pm = V(x_\Gamma, \pm\frac{1}{2})$. Also, the 4th/5th order EIC is expressed as

$$
\boxed{\begin{array}{l}
[E\times\vec{n}] = \eta\mathcal{A}\varphi,\quad \varphi + \frac{\eta^2}{12}\tilde{\mathcal{B}}\mathcal{A}\varphi = \langle H_T\rangle\\
[H\times\vec{n}] = -\eta\mathcal{B}\psi,\quad \psi + \frac{\eta^2}{12}\tilde{\mathcal{A}}\mathcal{B}\psi = \langle E_T\rangle\\
\\
\mathcal{A}V = \hat{\mu}^\eta\frac{\partial V}{\partial t} + \vec{\nabla}_\Gamma\times\left(\frac{1}{\hat{\varepsilon}^\eta\frac{\partial}{\partial t}}\nabla_\Gamma\times V\right),\quad \mathcal{B}V = \hat{\varepsilon}\frac{\partial V}{\partial t} + \vec{\nabla}_\Gamma\times\left(\frac{1}{\hat{\mu}^\eta\frac{\partial}{\partial t}}\nabla_\Gamma\times V\right)\\
\tilde{\mathcal{A}}V = \tilde{\mu}^\eta\frac{\partial V}{\partial t} - \nabla_\Gamma\left(\frac{1}{\tilde{\varepsilon}^\eta\frac{\partial}{\partial t}}\nabla_\Gamma\cdot V\right),\quad \tilde{\mathcal{B}}V = \tilde{\varepsilon}^\eta\frac{\partial V}{\partial t} - \nabla_\Gamma\left(\frac{1}{\hat{\mu}^\eta\frac{\partial}{\partial t}}\nabla_\Gamma\cdot V\right)
\end{array}}
$$

where $\tilde{\varepsilon} = \mathrm{tr}\hat{\varepsilon} - \hat{\varepsilon}$, $\quad\tilde{\mu} = \mathrm{tr}\hat{\mu} - \hat{\mu}$

6.2 Time-domain scheme using a discontinuous Galerkin method

Let's express E and H as a series of Lagrange polynomials (ℓ_j) based on Legendre-Gauss-Lobatto points.

$$
[E_N, H_N] = \sum_{j=0}^{N}[\tilde{E}_j(t), \tilde{H}_j(t)]\ell_j(\vec{x}),\qquad \vec{x}_i = \text{Legendre-Gauss-Lobatto points}
$$

Substituting the above series into Eq. (6.1) and integrating by parts twice, we have [14] for $1\le i\le N$

$$
\int_{\Omega_{P,Q}}(\hat{\varepsilon}_0\frac{\partial E_N}{\partial t} - \nabla\times H_N)\ell_i(\vec{x})dx = -\int_{\partial\Omega_{P,Q}}\vec{n}\times(H-H^*)\ell_i dx
$$
$$
\int_{\Omega_{P,Q}}(\hat{\mu}_0\frac{\partial H_N}{\partial t} + \nabla\times E_N)\ell_i(\vec{x})dx = \int_{\partial\Omega_{P,Q}}\vec{n}\times(E-E^*)\ell_i dx
$$

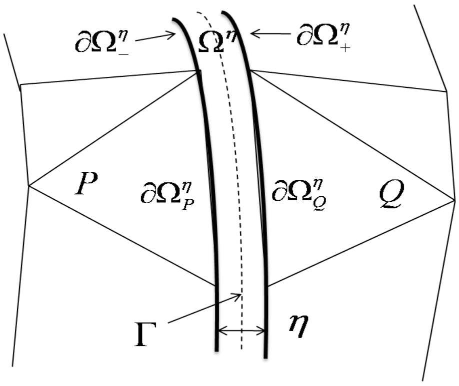

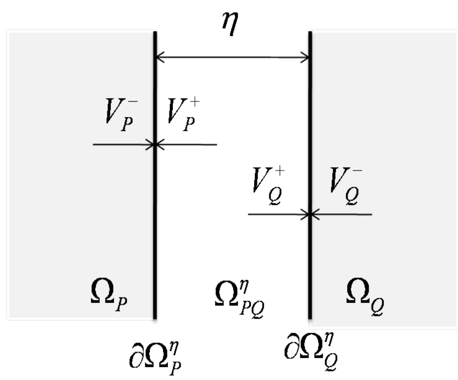

Figure 6.2: Definitions of domain/boundaries (left) and field values on the boundaries (right) in P and Q element are shown

where * indicates the numerical flux of the corresponding vector quantity. Let's choose central flux $V^* = \frac{1}{2}(V^+ + V^-)$ for simplicity. Then, we obtain

$$\int_{\Omega_{P,Q}} (\hat{\varepsilon}_0 \frac{\partial E_N}{\partial t} - \nabla \times H_N)\ell_i(\vec{x})dx = -\frac{1}{2}\int_{\partial\Omega_{P,Q}} \vec{n} \times (H^- - H^+)\ell_i dx$$
$$\int_{\Omega_{P,Q}} (\hat{\mu}_0 \frac{\partial H_N}{\partial t} + \nabla \times E_N)\ell_i(\vec{x})dx = \frac{1}{2}\int_{\partial\Omega_{P,Q}} \vec{n} \times (E^- - E^+)\ell_i dx$$

where, superscript (-) refers to local values and (+) refers to neighbor values of the element. Consider two elements P and Q adjacent to a thin layer in the opposite direction. One side of P and Q element face each other with two vertexes of them lying on $\partial\Omega^\eta_-$ and $\partial\Omega^\eta_+$, respectively. While the domain of P and Q are defined as Ω_P and Ω_Q, let's call this face of P and Q as $\partial\Omega^\eta_P$ and $\partial\Omega^\eta_Q$ (see Fig. 6.2). Suppose any points of $\partial\Omega^\eta_Q$ are normal projections of points in $\partial\Omega^\eta_Q$ and their distance are constant η, i.e., $\vec{x}_P = \eta(\vec{n}\cdot\vec{x}_Q)$, $\vec{x}_P \in \partial\Omega^\eta_P$, $\vec{x}_Q \in \partial\Omega^\eta_Q$. Since η is relatively small, the mesh can be easily adapted to this condition. Let's define the jump term $[V]^\eta_{QP}$ such as $[V]^\eta_{QP} = V_Q^+ - V_P^- = V_Q^- - V_P^+$, where $V_Q^-\{V_P^-\}$ is a field value on $\partial\Omega^\eta_Q\{\partial\Omega^\eta_P\}$ approached from the element $Q\{P\}$ and $V_Q^+\{V_P^+\}$ is a field value on $Q^\eta_f\{P^\eta_f\}$ approached from the thin layer. Note we assumed $V_Q^+ - V_P^-$ and $V_Q^- - V_P^+$ are the same or their difference is negligible. Then, for the Q element $(1 \le i \le N)$

$$\int_{\Omega_Q} (\hat{\varepsilon}_0 \frac{\partial E_N}{\partial t} - \nabla \times H_N)\ell_i(\vec{x})dx = -\frac{1}{2}\int_{\partial\Omega_Q/\partial\Omega_Q^\eta} \vec{n} \times (H^- - H^+)\ell_i dx$$
$$-\frac{1}{2}\int_{\partial\Omega_Q^\eta} \vec{n} \times (H_Q^- - H_P^- - [H]_{PQ}^\eta)\ell_i dx$$
$$\int_{\Omega_Q} (\hat{\mu}_0 \frac{\partial H_N}{\partial t} + \nabla \times E_N)\ell_i(\vec{x})dx = \frac{1}{2}\int_{\partial\Omega_Q/\partial\Omega_Q^\eta} \vec{n} \times (E^- - E^+)\ell_i dx$$
$$+\frac{1}{2}\int_{\partial\Omega_Q^\eta} \vec{n} \times (E_Q^- - E_P^- - [E]_{PQ}^\eta)\ell_i dx$$

The EIC conditions indicate that $[H]^\eta$ is a function of $\frac{\partial E_N}{\partial t}$ and $[E]^\eta$ is a function of $\frac{\partial H_N}{\partial t}$, i.e., $[H]^\eta = \mathcal{B}^k\left(\frac{\partial E_N}{\partial t}\right)$ and $[E]^\eta = \mathcal{B}^k\left(\frac{\partial H_N}{\partial t}\right)$, thus

$$\int_{\Omega_Q} (\hat{\varepsilon}_0 \frac{\partial E_N}{\partial t} - \nabla \times H_N)\ell_i(\vec{x})dx - \frac{1}{2}\int_{\partial\Omega_Q^\eta} \vec{n} \times \mathcal{B}^k\left(\frac{\partial E_N}{\partial t}\right)\ell_i dx$$
$$= -\frac{1}{2}\int_{\partial\Omega_Q/\partial\Omega_Q^\eta} \vec{n} \times (H^- - H^+)\ell_i dx - \frac{1}{2}\int_{\partial\Omega_Q^\eta} \vec{n} \times (H_Q^- - H_P^-)\ell_i dx \tag{6.14}$$

$$\int_{\Omega_Q} (\hat{\mu}_0 \frac{\partial H_N}{\partial t} + \nabla \times E_N)\ell_i(\vec{x})dx + \frac{1}{2}\int_{\partial\Omega_Q^\eta} \vec{n} \times \mathcal{B}^k\left(\frac{\partial H_N}{\partial t}\right)\ell_i dx$$
$$= \frac{1}{2}\int_{\partial\Omega_Q/\partial\Omega_Q^\eta} \vec{n} \times (E^- - E^+)\ell_i dx + \frac{1}{2}\int_{\partial\Omega_Q^\eta} \vec{n} \times (E_Q^- - E_P^-)\ell_i dx \tag{6.15}$$

Similarly for P element $(1 \le i \le N)$

$$\int_{\Omega_P} (\hat{\varepsilon}_0 \frac{\partial E_N}{\partial t} - \nabla \times H_N)\ell_i(\vec{x})dx - \frac{1}{2}\int_{\partial\Omega_P^\eta} \vec{n} \times \mathcal{B}^k\left(\frac{\partial E_N}{\partial t}\right)\ell_i dx$$
$$= -\frac{1}{2}\int_{\partial\Omega_P/\partial\Omega_P^\eta} \vec{n} \times (H^- - H^+)\ell_i dx - \frac{1}{2}\int_{\partial\Omega_P^\eta} \vec{n} \times (H_P^- - H_Q^-)\ell_i dx \tag{6.16}$$

$$\int_{\Omega_P} (\hat{\mu}_0 \frac{\partial H_N}{\partial t} + \nabla \times E_N)\ell_i(\vec{x})dx + \frac{1}{2}\int_{\partial\Omega_P^\eta} \vec{n} \times \mathcal{B}^k\left(\frac{\partial H_N}{\partial t}\right)\ell_i dx$$
$$= \frac{1}{2}\int_{\partial\Omega_P/\partial\Omega_Q^\eta} \vec{n} \times (E^- - E^+)\ell_i dx + \frac{1}{2}\int_{\partial\Omega_P^\eta} \vec{n} \times (E_P^- - E_Q^-)\ell_i dx \tag{6.17}$$

Note the right hand side of Eqs. (6.14)-(6.17) can be obtained without using grid points in the thin layer. The only unknown variables in Eqs. (6.14)-(6.17) are $\frac{\partial E_N}{\partial t}$ and $\frac{\partial H_N}{\partial t}$. Solving the system of linear Eqs. (6.14) and (6.16) yields $\frac{\partial E_N}{\partial t}$ while solving Eqs. (6.15) and (6.17) yields $\frac{\partial H_N}{\partial t}$. The size of the linear equations is the same as the number of grid points per point (1D), edge (2D) and face (3D) of a element, so the computational costs of solving the above equations are negligible.

6.3 One dimensional transmission layer

6.3.1 Implementation of 3rd order EIC in DG

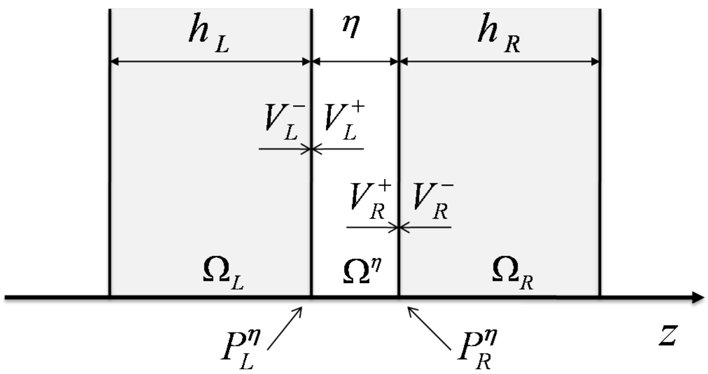

Figure 6.3: Definitions of domain and field values when an element has a thin layer at only one end of domain. Note $\langle V\rangle = \frac{1}{2}\left\{V_L(P_L^\eta) + V_R(P_R^\eta)\right\}$ and $[V] = V_R(P_R^\eta) - V_L(P_L^\eta)$.

Let $\vec{z}$ be the direction of wave propagation and E , H have two tangential component along x and y directions, i.e., $E = E_x\vec{x}+E_y\vec{y}$, $H = H_x\vec{x}+H_y\vec{y}$. Then, the corresponding 3rd order EIC is

$$[E \times \vec{n}] = \eta\hat{\mu}^\eta \frac{\partial\langle H\rangle}{\partial t}, \qquad [H \times \vec{n}] = -\eta\hat{\varepsilon}^\eta \frac{\partial\langle E\rangle}{\partial t} \tag{6.18}$$

Consider the following Maxwell's equations

$$\hat{\varepsilon}_0 \frac{\partial E}{\partial t} = \hat{\sigma}\frac{\partial H}{\partial z}, \qquad \hat{\mu}_0 \frac{\partial H}{\partial t} = -\hat{\sigma}\frac{\partial E}{\partial z} \qquad \text{where} \quad \hat{\sigma} = \begin{bmatrix} 0 & -1 \\ 1 & 0 \end{bmatrix} \tag{6.19}$$

Let Ω_L and Ω_R be the domain located at the left and right hand side of the thin layer, respectively (see Fig 6.3). Then, we get the following semi-discrete discontinuous Galerkin (DG) scheme. (subscript L, R indicates the element of Ω_L, Ω_R)

$$\hat{\varepsilon}_0 \frac{h^L}{2} \hat{\sigma} \mathcal{M}_{1d} \frac{\partial E_L}{\partial t} + \mathcal{S}^z_{1d} \cdot H_L = \frac{1}{2} \vec{e}_N (H_L^- - H_R^- + [H]^\eta_{LR}) \tag{6.20}$$

$$\hat{\varepsilon}_0 \frac{h^R}{2} \hat{\sigma} \mathcal{M}_{1d} \frac{\partial E_R}{\partial t} + \mathcal{S}^z_{1d} \cdot H_R = \frac{1}{2} \vec{e}_0 (H_R^- - H_L^- - [H]^\eta_{LR}) \tag{6.21}$$

where, $\mathcal{M}_{1d}$, $\mathcal{S}^z_{1d}$ is the one dimensional mass matrix, stiff matrix and h^L, h^R is the width of domain Ω_L, Ω_R, respectively and $\vec{e}_i$ is a unit vector with only nonzero element in i' th component. Substituting 3rd order EIC into the above equation, we obtain

$$\begin{aligned}
\hat{\varepsilon}_0 \frac{h^L}{2} \hat{\sigma} \mathcal{M}_{1d} \frac{\partial E_L}{\partial t} + \frac{\eta}{2} \vec{e}_N \hat{\sigma} \hat{\varepsilon}^\eta \frac{\partial \langle E \rangle}{\partial t} &= -\mathcal{S}^z_{1d} \cdot H_P + \frac{1}{2} \vec{e}_N (H_L^- - H_R^-) \\
\hat{\varepsilon}_0 \frac{h^R}{2} \hat{\sigma} \mathcal{M}_{1d} \frac{\partial E_R}{\partial t} + \frac{\eta}{2} \vec{e}_0 \hat{\sigma} \hat{\varepsilon}^\eta \frac{\partial \langle E \rangle}{\partial t} &= -\mathcal{S}^z_{1d} \cdot H_R + \frac{1}{2} \vec{e}_0 (H_R^- - H_L^-)
\end{aligned}$$

Multiply both sides of the first equation by $\frac{2}{h^L} \hat{\sigma}^{-1} \mathcal{M}^{-1}$ and the second equation by $\frac{2}{h^R} \hat{\sigma}^{-1} \mathcal{M}^{-1}$ to obtain

$$\begin{aligned}
&\hat{\varepsilon}_0 \frac{\partial E_L}{\partial t} + \frac{\eta}{h^L} (\mathcal{M}^{-1} \vec{e}_N) \hat{\varepsilon}^\eta \frac{\partial \langle E \rangle}{\partial t} \\
&\qquad = -\frac{2}{h^L} \hat{\sigma}^{-1} \mathcal{M}^{-1} \left\{ \mathcal{S} \cdot H_L - \frac{1}{2} \vec{e}_N (H_L^- - H_R^-) \right\} = \left. \frac{\partial E_L}{\partial t} \right|_0 \\
&\hat{\varepsilon}_0 \frac{\partial E_R}{\partial t} + \frac{\eta}{h^R} (\mathcal{M}^{-1} \vec{e}_0) \hat{\varepsilon}^\eta \frac{\partial \langle E \rangle}{\partial t} \\
&\qquad = -\frac{2}{h^R} \hat{\sigma}^{-1} \mathcal{M}^{-1} \left\{ \mathcal{S} \cdot H_R - \frac{1}{2} \vec{e}_0 (H_R^- - H_L^-) \right\} = \left. \frac{\partial E_R}{\partial t} \right|_0
\end{aligned}$$

Note that $V|_0$ indicates the field value when the thickness of the thin layer is zero ($\eta = 0$). Let's define a matrix $\mathcal{R}$ such as $\mathcal{R}(i, N-i+1) = 1,\ 1 \le i \le N$, i.e., $\mathcal{R}$ is a matrix which exchanges i'th component with $(N-i+1)$'th component of vector with length N. Multiply $\mathcal{R}$ to the above second equation and add it to the first equation, then we have after dividing by 2.

$$\frac{1}{2} \hat{\varepsilon}_0 \left(\frac{\partial E_L}{\partial t} + \mathcal{R} \frac{\partial E_R}{\partial t} \right) + \frac{\eta}{\tilde{h}} \left(\mathcal{M}^{-1} \vec{e}_N \right) \hat{\varepsilon}^\eta \frac{\partial \langle E \rangle}{\partial t} = \frac{1}{2} \left\{ \left. \frac{\partial E_L}{\partial t} \right|_0 + \mathcal{R} \left. \frac{\partial E_R}{\partial t} \right|_0 \right\}$$

where, $\tilde{h} = \frac{2h_L h_R}{h_L + h_R}$. Note we used $\vec{e}_0 = \mathcal{R}\cdot\vec{e}_N$. Also, if we let $\widehat{\frac{\partial\langle E\rangle}{\partial t}} = \frac{1}{2}\left(\frac{\partial E_L}{\partial t} + \mathcal{R}\frac{\partial E_R}{\partial t}\right)$, then the N' th element of $\widehat{\frac{\partial\langle E\rangle}{\partial t}}$ is $\frac{\partial\langle E\rangle}{\partial t}$, i.e., $\widehat{\frac{\partial\langle E\rangle}{\partial t}}(N) = \frac{\partial\langle E\rangle}{\partial t}$, thus

$$\left(\hat{\varepsilon}_0\mathbf{I} + \frac{\eta}{\tilde{h}}\left(\mathcal{M}^{-1}\vec{e}_N\right)\hat{\varepsilon}^\eta\right)\widehat{\frac{\partial\langle E\rangle}{\partial t}} = \frac{1}{2}\left\{\left.\frac{\partial E_L}{\partial t}\right|_0 + \mathcal{R}\left.\frac{\partial E_R}{\partial t}\right|_0\right\}$$

where, $\mathbf{I}$ is the identity matrix with length of N. However, since the last element of $\widehat{\frac{\partial\langle E\rangle}{\partial t}}$ is $\frac{\partial\langle E\rangle}{\partial t}$, we only need to solve

$$\frac{\partial\langle E\rangle}{\partial t} = \widehat{\frac{\partial\langle E\rangle}{\partial t}}(N) = \left(\hat{\varepsilon}_0 + \frac{\eta}{\tilde{h}}\mathcal{M}^{-1}(N)\hat{\varepsilon}^\eta\right)\frac{1}{2}\left\{\left.\frac{\partial E_L}{\partial t}(N)\right|_0 + \left.\frac{\partial E_R}{\partial t}(1)\right|_0\right\} \quad (6.22)$$

Similarly for $\frac{\partial\langle H\rangle}{\partial t}$, we have

$$\frac{\partial\langle H\rangle}{\partial t} = \widehat{\frac{\partial\langle H\rangle}{\partial t}}(N) = \left(\hat{\mu}_0 + \frac{\eta}{\tilde{h}}\mathcal{M}^{-1}(N)\hat{\mu}^\eta\right)\frac{1}{2}\left\{\left.\frac{\partial H_L}{\partial t}(N)\right|_0 + \left.\frac{\partial H_R}{\partial t}(1)\right|_0\right\} \quad (6.23)$$

Solving Eqs. (6.22)-(6.23), we get $\frac{\partial\langle E\rangle}{\partial t}$, $\frac{\partial\langle H\rangle}{\partial t}$ and consequently $[E]$, $[H]$ by 3rd order EIC (Eq. (6.13)), which are used in Eq. (6.20) - (6.21) to approximate thin layers without using grid points inside thin layers. Also, the case with thin layers at both ends of a domain can be solved in a similar way. Let's consider grid elements L, M, R of thickness h_L, h^M, h^R such that L and M are separated by a thin layer $\Omega^{\eta L}$ of thickness η^L, while M and R are separated by another thin layer $\Omega^{\eta R}$ of thickness η^R (see Fig. 6.4). Then, the discrete DG scheme for $\frac{dE}{dt}$ corresponding to this domain is given as follows

$$\hat{\varepsilon}_0\frac{h^L}{2}\hat{\sigma}\mathcal{M}_{1d}\frac{\partial E_L}{\partial t} + \mathcal{S}^z_{1d}\cdot H_L = \frac{1}{2}\vec{e}_N\left(H^-_L - H^-_M + [H]^{\eta L}\right)$$
$$\hat{\varepsilon}_0\frac{h^M}{2}\hat{\sigma}\mathcal{M}_{1d}\frac{\partial E_M}{\partial t} + \mathcal{S}^z_{1d}\cdot H_M = -\frac{1}{2}\vec{e}_0\left(H^-_M - H^-_L + [H]^{\eta L}\right) + \frac{1}{2}\vec{e}_N\left(H^-_M - H^-_R + [H]^{\eta R}\right)$$
$$\hat{\varepsilon}_0\frac{h^R}{2}\hat{\sigma}\mathcal{M}_{1d}\frac{\partial E_R}{\partial t} + \mathcal{S}^z_{1d}\cdot H_R = -\frac{1}{2}\vec{e}_0\left(H^-_R - H^-_M - [H]^{\eta R}\right)$$

Note superscript ηL, ηL indicates field value for the left and the right thin layer, respectively. After the similar algebra as one thin layer case, we have the following system of equations for $\widehat{\frac{\partial\langle E\rangle}{\partial t}}^{\eta L}$, $\widehat{\frac{\partial\langle E\rangle}{\partial t}}^{\eta R}$

$$\left(\hat{\varepsilon}_0\mathbf{I} + \frac{\eta}{\tilde{h}^L}\left(\mathcal{M}^{-1}_{1d}\vec{e}_N\right)\hat{\varepsilon}^\eta\right)\widehat{\frac{\partial\langle E\rangle}{\partial t}}^{\eta L} + \left(\hat{\varepsilon}_0\mathbf{I} + \frac{\eta}{\tilde{h}^R}\left(\mathcal{M}^{-1}_{1d}\vec{e}_0\right)\hat{\varepsilon}^\eta\right)\widehat{\frac{\partial\langle E\rangle}{\partial t}}^{\eta R}$$
$$= \frac{1}{2}\left(\left.\frac{\partial E_L}{\partial t}\right|_0 + 2\mathcal{R}\left.\frac{\partial E_M}{\partial t}\right|_0 + \left.\frac{\partial E_R}{\partial t}\right|_0\right) \quad (6.24)$$

$$\left(\hat{\varepsilon}_0\mathbf{I}+\frac{\eta}{2h^L}\left(\mathcal{M}_{1d}^{-1}\vec{e}_N\right)\hat{\varepsilon}^{\eta}\right)\widehat{\frac{\partial\langle E\rangle}{\partial t}}^{\eta L}-\left(\hat{\varepsilon}_0\mathbf{I}+\frac{\eta}{2h^R}\left(\mathcal{M}_{1d}^{-1}\vec{e}_0\right)\hat{\varepsilon}^{\eta}\right)\widehat{\frac{\partial\langle E\rangle}{\partial t}}^{\eta R}$$
$$=\frac{1}{2}\left(\left.\frac{\partial E_L}{\partial t}\right|_0-\left.\frac{\partial E_R}{\partial t}\right|_0\right) \tag{6.25}$$

where, $\tilde{h}^L=\frac{h^Lh^M}{h^M+2h^L}$, $\tilde{h}^R=\frac{h^Rh^M}{h^M+2h^R}$. Since we are only interested in evaluating $\widehat{\frac{\partial\langle E\rangle}{\partial t}}^{\eta L}(N)$ and $\widehat{\frac{\partial\langle E\rangle}{\partial t}}^{\eta R}(1)$, the computational cost of solving Eqs. (6.24)-(6.25) is equivalent to solving 4×4 linear system of equations.

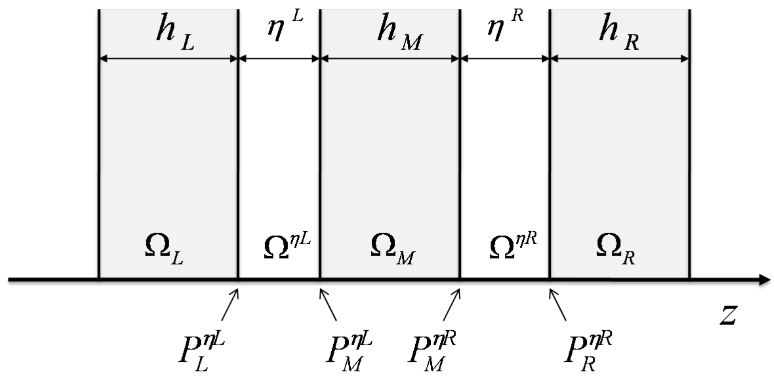

Figure 6.4: Definitions of domain and field values when an element has a thin layer at the both ends of domain. Note $\langle V\rangle^{\eta L}=\frac{1}{2}\left\{V_L(P_L^{\eta L})+V_M(P_M^{\eta L})\right\}$ and $[V]^{\eta L}=V_M(P_M^{\eta L})-V_L(P_L^{\eta L})$ while $\langle V\rangle^{\eta R}=\frac{1}{2}\left\{V_M(P_M^{\eta R})+V_R(P_M^{\eta R})\right\}$ and $[V]^{\eta R}=V_R(P_R^{\eta R})-V_M(P_M^{\eta R})$

6.3.2 Implementation of 5th order EIC in DG

The one dimensional 5th order EIC condition can be shown to be

$$\left\{\begin{array}{l}[E\times\vec{n}]=\eta\hat{\mu}^{\eta}\frac{\partial\varphi}{\partial t}\\ \varphi+\frac{\eta^2}{12}\bar{\varepsilon}^{\eta}\hat{\mu}^{\eta}\frac{\partial^2\varphi}{\partial t^2}=\langle H\rangle\end{array}\right.,\quad\left\{\begin{array}{l}[H\times\vec{n}]=-\eta\hat{\varepsilon}^{\eta}\frac{\partial\psi}{\partial t}\\ \psi+\frac{\eta^2}{12}\bar{\mu}^{\eta}\hat{\varepsilon}^{\eta}\frac{\partial^2\psi}{\partial t^2}=\langle E\rangle\end{array}\right. \tag{6.26}$$

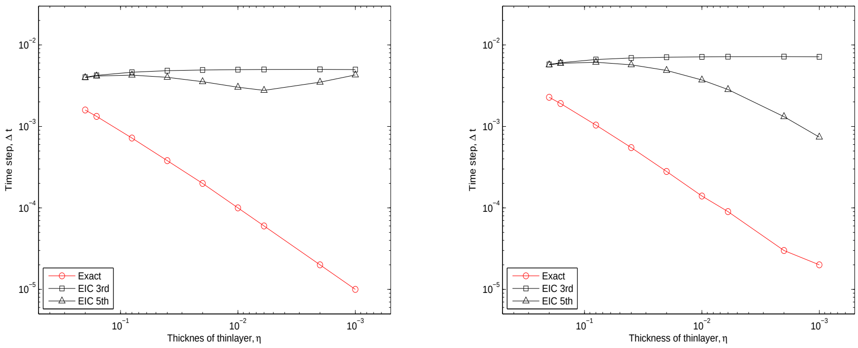

Figure 6.5: Stable time step Δt vs. thickness of thin layer η of the exact computation (circle), 3rd order EIC (square) and 5th order EIC (triangle) in leap frog (left) and explicit Runge-Kutta 4th order (right) are shown.

Substituting this into the Eqs. (6.20) - (6.21), we have

$$\begin{aligned}
\hat{\varepsilon}_0 \frac{\partial E_L}{\partial t} &= \left.\frac{\partial E_L}{\partial t}\right|_0 - \frac{\eta}{h^L}\left(\mathcal{M}^{-1}\vec{e}_N\right)\hat{\varepsilon}^\eta \zeta \\
\hat{\varepsilon}_0 \frac{\partial E_R}{\partial t} &= \left.\frac{\partial E_R}{\partial t}\right|_0 - \frac{\eta}{h^R}\left(\mathcal{M}^{-1}\vec{e}_0\right)\hat{\varepsilon}^\eta \zeta \\
\frac{\partial \zeta}{\partial t} &= \frac{12}{\eta^2}(\bar{\mu}^\eta \hat{\varepsilon}^\eta)^{-1}\left(\langle E\rangle - \Psi\right) \\
\frac{\partial \Psi}{\partial t} &= \zeta
\end{aligned}$$

Similarly for the two thin layer case, we have

$$\begin{aligned}
\hat{\varepsilon}_0 \frac{\partial E_L}{\partial t} &= \left.\frac{\partial E_L}{\partial t}\right|_0 - \frac{\eta}{h^L}\left(\mathcal{M}^{-1}\vec{e}_N\right)\hat{\varepsilon}^\eta \zeta^L \\
\hat{\varepsilon}_0 \frac{\partial E_M}{\partial t} &= \left.\frac{\partial E_M}{\partial t}\right|_0 - \frac{\eta}{h^M}\left(\mathcal{M}^{-1}\vec{e}_0\right)\hat{\varepsilon}^\eta \zeta^L - \frac{\eta}{h^M}\left(\mathcal{M}^{-1}\vec{e}_N\right)\hat{\varepsilon}^\eta \zeta^R \\
\hat{\varepsilon}_0 \frac{\partial E_R}{\partial t} &= \left.\frac{\partial E_R}{\partial t}\right|_0 - \frac{\eta}{h^R}\left(\mathcal{M}^{-1}\vec{e}_0\right)\hat{\varepsilon}^\eta \zeta^R \\
\frac{\partial \zeta^{L,R}}{\partial t} &= \frac{12}{\eta^2}(\bar{\mu}^\eta \hat{\varepsilon}^\eta)^{-1}\left(\langle E\rangle^{L,R} - \Psi^{L,R}\right) \\
\frac{\partial \Psi^{L,R}}{\partial t} &= \zeta^{L,R}
\end{aligned}$$

where, ζ, Ψ is a vector of length 2. Note that the above scheme can be time-marched with any explicit time stepping scheme such as an explicit 4th order

Runge-Kutta. However, the time step Δt doesn't depend on η since the 3rd order EIC is implemented in an implicit way. The 5th order EIC cannot be implemented in the same way as the 3rd order EIC, since $[E]$ and $[H]$ are not an explicit function of $\frac{\partial \langle H \rangle}{\partial t}$ and $\frac{\partial \langle E \rangle}{\partial t}$. Thus, the scheme with the 5th order EIC shows better performance in accuracy compared to that with the 3rd order EIC, but the stable time step Δt of 5th order EIC needs to be approximately proportional to η, which is still much larger than Δt of the exact computation that is proportional to η^2, though (see Fig. 6.5)

6.3.3 Numerical convergence test

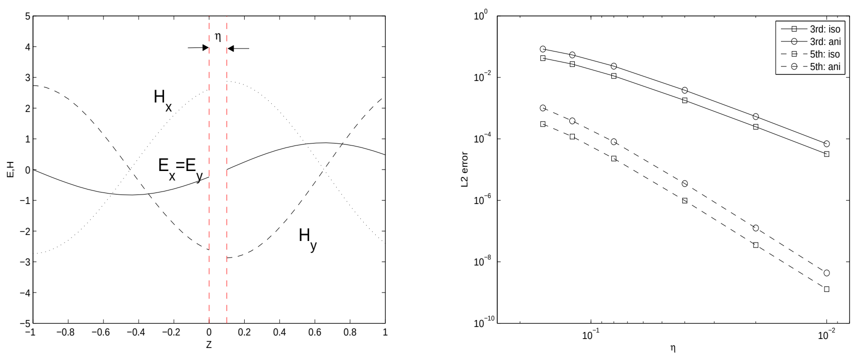

Figure 6.6: Initial conditions in a domain containing one thin layer (dashed lines) (left) and its convergence graph (right) where solid line, dashed line indicates 3rd order EIC, 5th order EIC while square, circle indicates isotropic material with $\varepsilon = 2.25$, anisotropic material with $\varepsilon_{xx} = \varepsilon_{yy} = 2.25,\ \varepsilon_{xy} = \varepsilon_{yx} = 1.5$, respectively

Consider Maxwell's equations in one dimension

$$\hat{\varepsilon}\frac{\partial \mathbf{E}}{\partial t} = \hat{\sigma}\frac{\partial \mathbf{H}}{\partial t}, \qquad \hat{\mu}\frac{\partial \mathbf{H}}{\partial t} = -\hat{\sigma}\frac{\partial \mathbf{E}}{\partial t} \tag{6.27}$$

For the one thin layer case, let a thin layer be located in the middle of the domain with thickness η with perfectly conducting wall located at $z^{(1)} = -1$ and a wall with boundary value $\mathbf{E} = E_R(t)$ at $z = 1$, i.e.,

$$\text{i)}\ \ \mathbf{E} = 0 \quad \text{or} \quad \frac{\partial \mathbf{H}}{\partial z} = 0 \qquad \text{at} \quad z = -1, \qquad \text{ii)}\ \ \mathbf{E} = E_R(t) \qquad \text{at} \quad z = 1$$

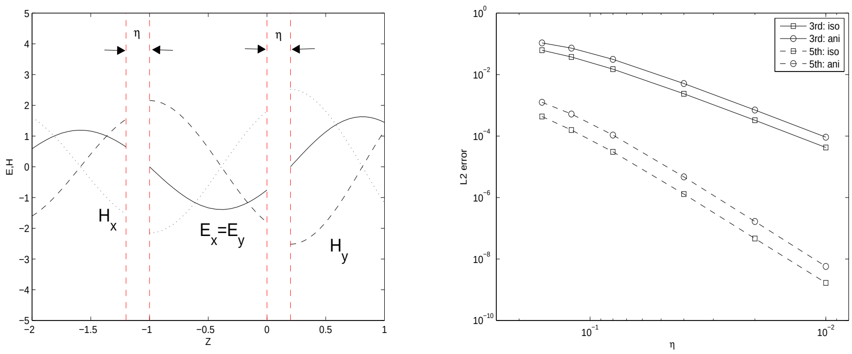

Figure 6.7: Initial conditions in a domain containing two thin layers (dashed lines) (left) and its convergence graph (right) where solid line, dashed line indicates 3rd order EIC, 5th order EIC while square, circle indicates isotropic material with $\varepsilon = 2.25$, anisotropic material with $\varepsilon_{xx} = \varepsilon_{yy} = 2.25,\ \varepsilon_{xy} = \varepsilon_{yx} = 1.5$, respectively

and

$$\text{iii)}\ \ \mathbf{E}^{(1)} = \mathbf{E}^{(2)}, \qquad \mathbf{H}^{(1)} = \mathbf{H}^{(2)} \qquad \text{at} \quad z = 0,\ \eta$$

Similarly for the two thin layers case, let two thin layers be located in the middle of the domain with thickness η with boundary value $\mathbf{E} = E_L(t)$ at $z^{(1)} = -2$ and a wall with boundary value $\mathbf{E} = E_R(t)$ at $z = 1$, i.e.,

$$\text{i)}\ \ \mathbf{E} = E_L(t) \qquad \text{at} \quad z = -2, \qquad \text{ii)}\ \ \mathbf{E} = E_R(t) \qquad \text{at} \quad z = 1$$

and

$$\text{iii)}\ \ \mathbf{E}^{(1)} = \mathbf{E}^{(2)}, \qquad \mathbf{H}^{(1)} = \mathbf{H}^{(2)} \qquad \text{at} \quad z = -1-\eta,\ -1,\ 0,\ \eta$$

Then, the solution of Eq. (6.27) satisfying the above boundary conditions can be expressed as

$$\begin{aligned} \mathbf{E} &= [A^{(k)} e^{in^{(k)}\omega z} - B^{(k)} e^{-in^{(k)}\omega z}] e^{i\omega t} \\ \mathbf{H} &= -n^{(k)} \hat{\sigma} [A^{(k)} e^{in^{(k)}\omega z} + B^{(k)} e^{-in^{(k)}\omega z}] e^{i\omega t} \end{aligned}$$

where, for the one thin layer case with $1 \le k \le 3$

$$\begin{aligned} A^{(1)} &= \frac{n^{(2)} \cos(\eta n^{(2)} \omega)}{n^{(1)} \cos(n^{(1)} \omega)}, \qquad A^{(2)} = e^{-i\omega(n^{(1)} + \eta n^{(2)})}, A^{(3)} = n^{(2)} e^{-2i\eta\omega} \\ B^{(1)} &= A^{(1)} e^{-i2n^{(1)}\omega}, \qquad B^{(2)} = A^{(2)} e^{i2\eta n^{(2)}\omega}, \qquad B^{(3)} = A^{(3)} e^{2i\eta\omega} \\ E_R(t) &= A^{(3)} e^{-i\omega} (e^{2i\omega} - e^{2i\eta\omega}) e^{i\omega t} \end{aligned}$$

or for the two thin layers case with $1 \le k \le 5$

$$
\begin{aligned}
A^{(3)} &= \frac{n^{(2)}\cos(\eta n^{(2)}\omega)}{n^{(1)}\cos(n^{(1)}\omega)}, \qquad A^{(4)} = e^{-i\omega(n^{(1)}+\eta n^{(2)})}, A^{(2)} = \frac{1}{n^{(2)}}A^{(3)}e^{-i\omega(1-n^{(2)})} \\
A^{(5)} &= n^{(2)}A^{(4)}e^{i\eta\omega(n^{(2)}-1)}, \quad A^{(1)} = A^{(2)}(n^{(2)}\cos(n^{(2)}\eta\omega) - i\sin(n^{(2)}\eta\omega))e^{-in^{(2)}\omega}e^{i\omega(1+\eta)} \\
B^{(2)} &= A^{(2)}e^{-i2n^{(2)}\omega}, \qquad B^{(3)} = A^{(3)}e^{-2i\omega}, \qquad B^{(3)} = A^{(4)}e^{2in^{(2)}\eta\omega} \\
B^{(5)} &= A^{(5)}e^{2i\eta\omega}, \quad B^{(1)} = (A^{(1)}e^{-i\omega(1+\eta)} + 2iA^{(2)}\sin(n^{(2)}\eta\omega)e^{-in^{(2)}\omega})e^{-i\omega(1+\eta)} \\
E_L(t) &= e^{i\omega t}(A^{(1)}e^{-2i\omega} - B^{(1)}e^{2i\omega}), \quad E_R(t) = e^{i\omega t}(A^{(5)}e^{i\omega} - B^{(5)}e^{-i\omega})
\end{aligned}
$$

where, $n^{(k)} = \sqrt{\varepsilon_{xx}^{(k)} + \varepsilon_{xy}^{(k)}} = \sqrt{\varepsilon_{yy}^{(k)} + \varepsilon_{xy}^{(k)}}$ with $\varepsilon_{xx}^{(k)} = \varepsilon_{yy}^{(k)}$ and ω is the solution of the following equation

$$-n^{(2)}\tan(n^{(1)}\omega) = n^{(1)}\tan(\eta n^{(2)}\omega)$$

Table 6.1 and Figs. (6.6) - (6.7) display their convergence of corresponding order for both of one thin layer case and two thin layers case.

• **One thin layer case**							
	η	0.16	0.12	0.08	0.04	0.02	0.01
Isotropic	EIC 3rd	-	1.5563	2.1810	2.6391	2.8593	2.9445
	EIC 5th	-	3.2463	4.0677	4.5394	4.8029	4.7664
Anisotropic	EIC 3rd	-	1.5289	2.0704	2.6039	2.8519	2.9425
	EIC 5th	-	3.3801	3.8475	4.5255	4.7949	4.8650
• **Two thin layers case**							
	η	0.16	0.12	0.08	0.04	0.02	0.01
Isotropic	EIC 3rd	-	1.7627	2.2466	2.6566	2.8609	2.9443
	EIC 5th	-	3.5433	4.0145	4.5667	4.8009	4.8009
Anisotropic	EIC 3rd	-	1.3512	2.0816	2.6152	2.8567	2.9402
	EIC 5th	-	3.0590	3.8914	4.5152	4.8209	4.8577

Table 6.1: Orders of L_2 error for EIC 3rd vs. EIC 5th for one thin layer and two thin layers are shown. Conditions are the same as given in Figs. (6.6) - (6.7)

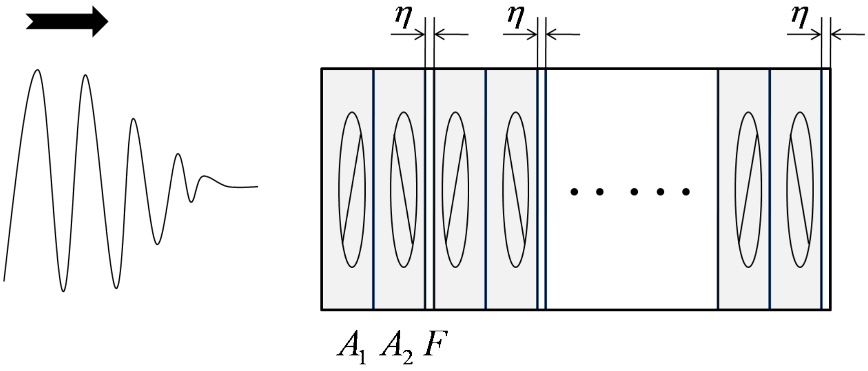

Figure 6.8: Magnetic photonic crystals (MPC) with 32 unit cells. One unit cell consists of two anisotropic layers with different misalignment angles (A_1, A_2) and one magnetic layer (F) with thickness η. 3rd order EIC is implemented for thin strong magnetic layer in DG scheme to model frozen mode phenomena

6.3.4 Application to a realistic problem: Modeling periodic magnetic crystals (MPC) without thin magnetic layers

In chapter 3, a periodic Magnetic photonic crystal (MPC) designed by Figotin and Vitebsky [9] is modeled in the time domain to display a strong unprecedented phenomena called the frozen mode. This MPC is a periodic array of unit cells which consist of two anisotropic layers with a different misalignment angle and one magnetic layer (Fig. 6.8). Accurate modeling of the frozen mode in the time domain enables us to identify every features of the phenomena, but suffered excessively long computational time due to extremely thin strong magnetic layer especially when an explicit time marching scheme is used. The thickness of magnetic layer is less than 5.0e-4 in the unit of wavelength (λ) while the width of two anisotropic layers are close to 0.5 λ. However, the computation without magnetic layers leads to totally different phenomena without showing any signs of the frozen mode. In this section, we model the MPC using 3rd order EIC with an explicit 4th order Runge Kutta method. Let's consider one dimensional Maxwell's equations again,

$$\hat{\varepsilon}_0 \frac{\partial E}{\partial t} = \hat{\sigma}\frac{\partial H}{\partial z}, \qquad \hat{\mu}_0 \frac{\partial H}{\partial t} = -\hat{\sigma}\frac{\partial E}{\partial z} \qquad \text{where } \hat{\sigma} = \begin{bmatrix} 0 & -1 \\ 1 & 0 \end{bmatrix}$$

However, since the permeability $\hat{\mu}^\eta$ of the magnetic material in the thin layer has imaginary part such as $\hat{\mu}^\eta = \hat{\mu}_r^\eta + i\hat{\mu}_i^\eta$, the 3rd order EIC is changed such as

$$[E \times \vec{n}] = \eta \hat{\mu}_r^\eta \frac{\partial \langle H \rangle}{\partial t} + 2\pi\hat{\sigma}\hat{\mu}_i \langle H \rangle, \qquad [H \times \vec{n}] = -\eta \hat{\varepsilon}^\eta \frac{\partial \langle E \rangle}{\partial t} \tag{6.28}$$

Substituting Eq. (6.28) into the above one dimensional Maxwell's equation and after similar algebra as before, we have (Note $\hat{\mu}_0 = \mathbf{I}$ for the anisotropic dielectric materials)

$$\begin{aligned}\left(\mathbf{I} + \frac{\eta}{\tilde{h}}\left(\mathcal{M}^{-1}\vec{e}_N\right)\hat{\mu}_r^\eta\right)\frac{\partial \widehat{\langle H \rangle}}{\partial t} = \frac{1}{2}\left\{\left.\frac{\partial H_L}{\partial t}\right|_0 + \mathcal{R}\left.\frac{\partial H_R}{\partial t}\right|_0\right\} \\ -\frac{2\pi\eta}{\tilde{h}}\left(\mathcal{M}^{-1}\vec{e}_N\right)\hat{\mu}_i^\eta \langle H \rangle\end{aligned} \tag{6.29}$$

Before we use scattered field formulation, let's define incident wave as a predefined wave when every layers are filled with vacuum, i.e., $\hat{\varepsilon}_0 = \hat{\varepsilon}^\eta = \mathbf{I}$, $\hat{\mu}_0 = \hat{\mu}^\eta = \mathbf{I}$. Then, Eq. (6.30) for the incident wave is

$$\left(\mathbf{I} + \frac{\eta}{\tilde{h}}\left(\mathcal{M}^{-1}\vec{e}_N\right)\right)\frac{\partial \widehat{\langle H^{inc} \rangle}}{\partial t} = \frac{1}{2}\left\{\left.\frac{\partial H_L^{inc}}{\partial t}\right|_0 + \mathcal{R}\left.\frac{\partial H_R^{inc}}{\partial t}\right|_0\right\} \tag{6.30}$$

With Eq. (6.30), the scattered formulation of Eq. (6.30) becomes

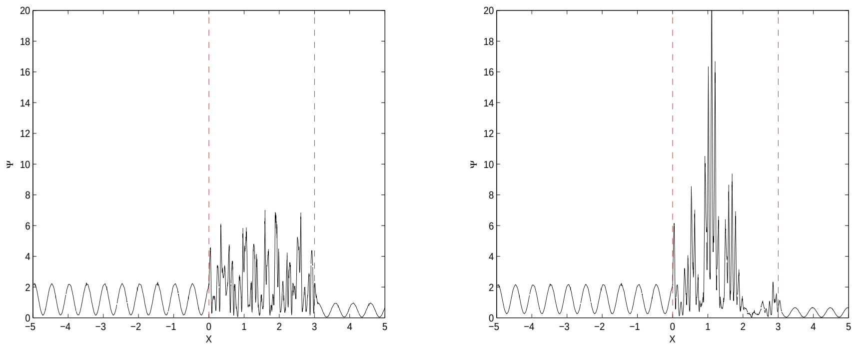

Figure 6.9: Field amplitude when the left boundary of thin layer is directly connected to the right boundary of thin layer (left) and field amplitude when 3rd order EIC is used (right). $T = 200$. The number of unit cell = 200. Dashed line indicates the boundaries of whole MPC. In fact, the L_2 error between the exact computation and 3rd order EIC is 1.5e-3 at $T = 200$

$$\left(\mathbf{I}+\frac{\eta}{\tilde{h}}\left(\mathcal{M}^{-1}\vec{e}_N\right)\hat{\mu}_r^\eta\right)\frac{\widehat{\partial\langle H^s\rangle}}{\partial t}=\frac{1}{2}\left\{\left.\frac{\partial H_L^s}{\partial t}\right|_0+\mathcal{R}\left.\frac{\partial H_R^s}{\partial t}\right|_0\right\}$$
$$+\frac{\eta}{\tilde{h}}\left(\mathcal{M}^{-1}\vec{e}_N\right)(\mathbf{I}-\hat{\mu}_r^\eta)\frac{\partial\langle H^{inc}\rangle}{\partial t}-\frac{2\pi\eta}{\tilde{h}}\left(\mathcal{M}^{-1}\vec{e}_N\right)\hat{\mu}_i^\eta\left(\langle H^s\rangle+\langle H^{inc}\rangle\right)$$

where, superscript 's' and 'inc' indicate the scattered and incident term respectively. Also, similarly,

$$\left(\mathbf{I}+\frac{\eta}{\tilde{h}}\left(\mathcal{M}^{-1}\vec{e}_N\right)\hat{\varepsilon}^M\hat{\varepsilon}^\eta\right)\frac{\widehat{\partial\langle E^s\rangle}}{\partial t}=\frac{1}{2}\left\{\left.\frac{\partial E_L^s}{\partial t}\right|_0+\mathcal{R}\left.\frac{\partial E_R^s}{\partial t}\right|_0\right\}$$
$$+\frac{\eta}{2}\left(\mathcal{M}^{-1}\vec{e}_N\right)\hat{\varepsilon}_M(\mathbf{I}-\hat{\varepsilon}^\eta)\frac{\partial\langle E^{inc}\rangle}{\partial t}+\frac{1}{2}\left\{((\hat{\varepsilon}_0^L)^{-1}-\mathbf{I})\frac{\partial E_L^{inc}}{\partial t}+((\hat{\varepsilon}_0^R)^{-1}-\mathbf{I})\frac{\partial E_R^{inc}}{\partial t}\right\}$$

where, $\hat{\varepsilon}_M=(\hat{\varepsilon}_0^L)^{-1}/h^L+(\hat{\varepsilon}_0^R)^{-1}/h^R$ and $\tilde{h}=\frac{2h_Lh_R}{h_L+h_R}$ when $\varepsilon_0^L,\ \varepsilon_0^R$ indicates permittivity tensor of $L,\ R$ element and $h_L\ h_R$ indicate the width of $L,\ R$ element, respectively. In each 32 unit cells, the magnetic layer of thickness 4.5895e-4 with $\varepsilon^\eta=5,\ \mu^\eta=60-i37\hat{\sigma}$ is approximated with 3rd order EIC. The left figure of Fig. (6.9) shows the magnitude of $\|E^2+H^2\|$, when no EIC is used. Field amplitude is not increasing inside the layer, which indicates no frozen mode occurs inside the layer. However, the right figure of Fig. (6.9) which was computed with the 3rd order EIC shows the strikingly increased field amplitude as that of the exact computation. In fact, the L_2 error between the exact computation and 3rd order EIC is 1.5e-3 at $T=200$, but time step Δt of the code with 3rd order EIC is set more than 100 times larger than that of exact computation.

6.4 Two dimensional transmission layer

6.4.1 Implementation of 3rd order EIC in DG

Consider the following two dimensional Maxwell's equations for the TE polarization

$$\begin{aligned}\varepsilon_0\frac{\partial E_x}{\partial t} &= \frac{\partial H_z}{\partial y}\\ \varepsilon_0\frac{\partial E_y}{\partial t} &= -\frac{\partial H_z}{\partial x}\\ \mu_0\frac{\partial H_z}{\partial t} &= \frac{\partial E_x}{\partial y}-\frac{\partial E_y}{\partial x}\end{aligned}$$

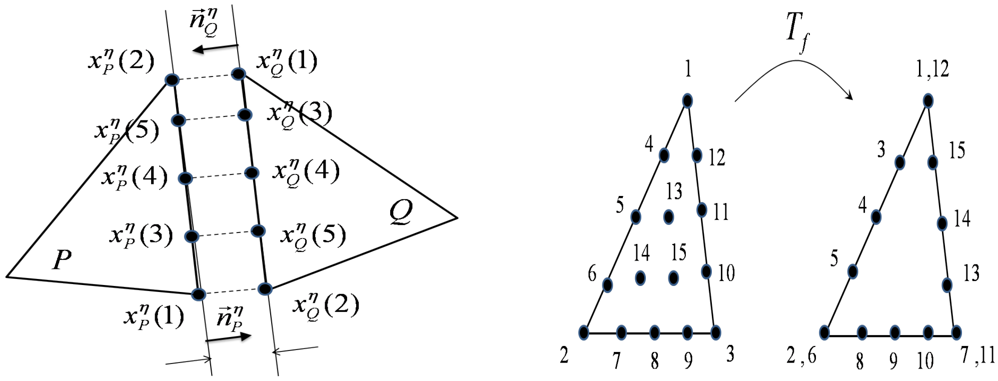

Figure 6.10: Grid points of P, Q element on edges contingent on a thin layer Ω_η (left), which requires an ordering matrix $\mathcal{R}$ for rearranging facial grid points for connecting P and Q element, Also, definition of map T_f (right) which maps all the grip points of an element into all the facial grid points. Number of order per element = 5

Let P and Q element be separated by a thin layer Ω^η. Let each edge of P, Q element touching a thin layer be denoted as $\partial\Omega_P^\eta$, $\partial\Omega_Q^\eta$ and x_P^η, x_Q^η as grid points on those edges, respectively (see the left of Fig. 6.10). Also, if we let $\vec{n}_P^\eta$, $\vec{n}_Q^\eta$ be the normal vector for $\partial\Omega_P^\eta$, $\partial\Omega_Q^\eta$, note that by assumption, $x_Q^\eta = \eta(\vec{n}_Q^\eta \cdot x_P^\eta) = -\eta(\vec{n}_P^\eta \cdot x_P^\eta)$. Then, the semi-discrete scheme with central flux is given as.

$$\hat{\sigma}\hat{\mathcal{M}}_{2d}\frac{\partial E_P}{\partial t} + \hat{\mathcal{S}}_{2d} \cdot H_P = \mathcal{F}_P^{-1}\vec{n}_P^\eta \cdot \left(H_P^- - H_Q^- + \mathcal{R}_P[H]^\eta\right) \tag{6.31}$$

$$\hat{\sigma}\hat{\mathcal{M}}_{2d}\frac{\partial E_Q}{\partial t} + \hat{\mathcal{S}}_{2d} \cdot H_Q = \mathcal{F}_Q^{-1}\vec{n}_Q^\eta \cdot \left(H_Q^- - H_P^- - \mathcal{R}_Q[H]^\eta\right) \tag{6.32}$$

where $\hat{\mathcal{M}}_{2d}$, $\hat{\mathcal{S}}_{2d}$ is two dimensional mass matrix, stiffness matrix, respectively, $\mathcal{F}_P$, $\mathcal{F}_Q$ is a Jacobian matrix for P, Q element and $\mathcal{R}_P$, $\mathcal{R}_Q$ is a reordering matrix such as $[V] = \mathcal{R}_Q H_Q - \mathcal{R}_P H_P$ or $\langle H\rangle = \frac{1}{2}(\mathcal{R}_Q H_Q + \mathcal{R}_P H_P)$ and $\mathcal{R}_{P,Q} = \mathcal{R}_{P,Q}^{-1}$. the 3rd order EIC corresponding to the TE polarization is written down as

$$[E_t] = \eta\left(\frac{\partial\langle H_z\rangle}{\partial t} - \frac{\partial\Phi}{\partial\tau} - \mathcal{C}\langle E_t\rangle\right), \quad \frac{\partial\Phi}{\partial t} = \frac{1}{\varepsilon_f^\eta}\frac{\partial\langle H_z\rangle}{\partial\tau} \tag{6.33}$$

$$[H_z] = \eta\hat{\varepsilon}^\eta\frac{\partial\langle E_t\rangle}{\partial t} \tag{6.34}$$

where, $E_t = \vec{n} \times E$, $\mathcal{C}$=curvature tensor, and ε_f^η is a constant such as $(\hat{\varepsilon}^\eta E)\cdot\vec{n} = \varepsilon_f^\eta(E\cdot\vec{n})$. Substituting the above 3rd order EIC into Eqs. (6.31) and (6.32) and multiplying both sides by $\hat{\mathcal{M}}^{-1}$ with $\vec{n} = \vec{n}_Q^\eta = -\vec{n}_P^\eta$

$$
\begin{aligned}
\frac{\partial E_P}{\partial t} + \eta\hat{\varepsilon}^\eta\hat{\sigma}\mathcal{F}_P^{-1}\hat{\mathcal{M}}^{-1}\mathcal{R}_P\left(\vec{n}\cdot\left(\frac{\partial\langle E\rangle}{\partial t}\times\vec{n}\right)\right) &= \left.\frac{\partial E_P}{\partial t}\right|_0 \\
\frac{\partial E_Q}{\partial t} + \eta\hat{\varepsilon}^\eta\hat{\sigma}\mathcal{F}_Q^{-1}\hat{\mathcal{M}}^{-1}\mathcal{R}_Q\left(\vec{n}\cdot\left(\frac{\partial\langle E\rangle}{\partial t}\times\vec{n}\right)\right) &= \left.\frac{\partial E_Q}{\partial t}\right|_0
\end{aligned}
$$

where, subscript 0 indicates the value when η is zero. Let's multiply both equations by T_f which maps all the grid points of an element into all the facial points (see the right of Fig. 6.10) and by $\mathcal{R}_P$, $\mathcal{R}_Q$, respectively.

$$
\begin{aligned}
\mathcal{R}_P\left(\frac{\partial E_P}{\partial t}\right)^f + \eta\hat{\varepsilon}^\eta\hat{\sigma}\mathcal{F}_P^{-1}\mathcal{R}_P T_f\hat{\mathcal{M}}^{-1}\mathcal{R}_P\left(\vec{n}\cdot\left(\frac{\partial\langle E\rangle}{\partial t}\times\vec{n}\right)\right) &= \mathcal{R}_P\left.\left(\frac{\partial E_P}{\partial t}\right)^f\right|_0 \\
\mathcal{R}_Q\left(\frac{\partial E_Q}{\partial t}\right)^f + \eta\hat{\varepsilon}^\eta\hat{\sigma}\mathcal{F}_Q^{-1}\mathcal{R}_Q T_f\hat{\mathcal{M}}^{-1}\mathcal{R}_Q\left(\vec{n}\cdot\left(\frac{\partial\langle E\rangle}{\partial t}\times\vec{n}\right)\right) &= \mathcal{R}_Q\left.\left(\frac{\partial E_Q}{\partial t}\right)^f\right|_0
\end{aligned}
$$

where, superscript f indicates the values at the facial nodes. Let's define $\widehat{\frac{\partial\langle E\rangle}{\partial t}} = \frac{1}{2}\left(\mathcal{R}_P\left(\frac{\partial E_P}{\partial t}\right)^f + \mathcal{R}_Q\left(\frac{\partial E_Q}{\partial t}\right)^f\right)$. Similar to the 1D case, we have $\widehat{\frac{\partial\langle E\rangle}{\partial t}}(1:N_f) = \frac{\partial\langle E\rangle}{\partial t}$, when N_f is the number of nodes along an edge, so if we take only nodal points on a $\partial\Omega_P^\eta$, $\partial\Omega_Q^\eta$, we have

$$
\begin{aligned}
&\frac{\partial\langle E\rangle}{\partial t} + \frac{1}{2}\eta\hat{\varepsilon}^\eta\hat{\sigma}\mathcal{U}^\eta\left(\vec{n}\cdot\left(\frac{\partial\langle E\rangle}{\partial t}\times\vec{n}\right)\right) \\
&\qquad = \frac{1}{2}\left\{\mathcal{R}_P^\eta\left.\left(\frac{\partial E_P}{\partial t}\right)^\eta\right|_0 + \mathcal{R}_Q^\eta\left.\left(\frac{\partial E_Q}{\partial t}\right)^\eta\right|_0\right\} \qquad (6.35)
\end{aligned}
$$

where, $\mathcal{U}^\eta = \left(\mathcal{F}_P^{-1}\mathcal{R}_P T_f\hat{\mathcal{M}}_{2d}^{-1}\mathcal{R}_P + \mathcal{F}_Q^{-1}\mathcal{R}_Q T_f\hat{\mathcal{M}}^{-1}\mathcal{R}_Q\right)^\eta$. Similarly, we obtain

$$
\begin{aligned}
\left(\mathbf{I} + \frac{1}{2}\eta\mathcal{U}^\eta\right)\frac{\partial\langle H_z\rangle}{\partial t} &= \frac{1}{2}\left\{\mathcal{R}_P^\eta\left.\left(\frac{\partial H_z}{\partial t}\right)_P^\eta\right|_0 + \mathcal{R}_Q^\eta\left.\left(\frac{\partial H_z}{\partial t}\right)_Q^\eta\right|_0\right\} \\
&\quad + \frac{1}{2}\eta\hat{\varepsilon}^\eta\mathcal{U}^\eta\left(\frac{\partial\Phi}{\partial\tau} + \mathcal{C}\langle E_t\rangle\right) \qquad (6.36)
\end{aligned}
$$

Solving Eqs. (6.35) and (6.36), we get $\frac{\partial\langle E\rangle}{\partial t}$, $\frac{\partial\langle E\rangle}{\partial t}$, and consequently $[E]$, $[H]$ by 3rd order EIC (Eqs. (6.33) and (6.34)). These $[E]$, $[H]$ can be inserted in Eqs. (6.31)-(6.32) to approximation E and H without using grid points within

thin layers. For the study of the convergence of EIC, the following Radar Cross Section (RCS) [33] is defined as

$$\mathrm{RCS}(\varphi) \equiv 2\pi \frac{|F(\varphi)|^2}{|E_{inc}|^2}, \qquad F(\varphi) \equiv \frac{e^{i(\pi/4)}}{\sqrt{8\pi k}} \oint_{C_a} \left[\omega\mu_0 \hat{z}' \cdot \breve{J} - kz' \times \breve{M}(r') \cdot \hat{r}\right] e^{ik\hat{r}\cdot r'} dC$$

where, $\breve{J} = \vec{n} \times H$, $\breve{M} = -\vec{n} \times E$, k and ω is the wave number and the frequency of the wave, r is the far-field observation point and r' is the near-field source point in C_a, which is a virtual surface and sufficiently far from scattering objects. Also, note the L_2 error of RCS is computed by comparing the quantity, $10^{(\mathrm{RCS}/10)}$.

6.4.2 Scattering by smooth cylindrical transmission layer

6.4.2.1 Circular cylindrical layer

Let's consider a circular thin layer whose cross section lies on the xy plane and which is infinitely long along z axis. Suppose it consists of two kinds of materials, which can be isotropic or anisotropic. Since when the radius of inner circle is r, the radius of the outer circle and the interface Γ is respectively $r+\eta$ and $r+0.5\eta$, the curvature tensor of the interface Γ is $\mathcal{C} = -\frac{1}{r+0.5\eta}\vec{\tau}$, where $\vec{\tau}$ is the tangential vector on the interface of Γ. The left figure of Fig. 6.11 compares the RCS [33] of the exact computation and that of the scheme with 3rd order EIC, which confirms the accuracy of the scheme. The right figures of Fig. 6.11 and Table 6.2 shows the corresponding order of convergence.

η	0.20	0.16	0.12	0.08	0.04
Isotropic material inside thin layer					
3rd EIC	8.4499e-02	4.6409e-02	2.0431e-02	7.0702e-03	1.0691e-03
	order	2.6854	2.8520	2.6171	2.7254
Anisotropic material inside thin layer					
3rd EIC	6.1789e-02	4.7078e-02	2.2496e-02	2.0578e-03	1.1676e-03
	order	1.2186	2.5670	5.8986	-

Table 6.2: Order of L_2 error of field components for 3rd order EIC are shown. Conditions are the same as given in Fig. 6.11

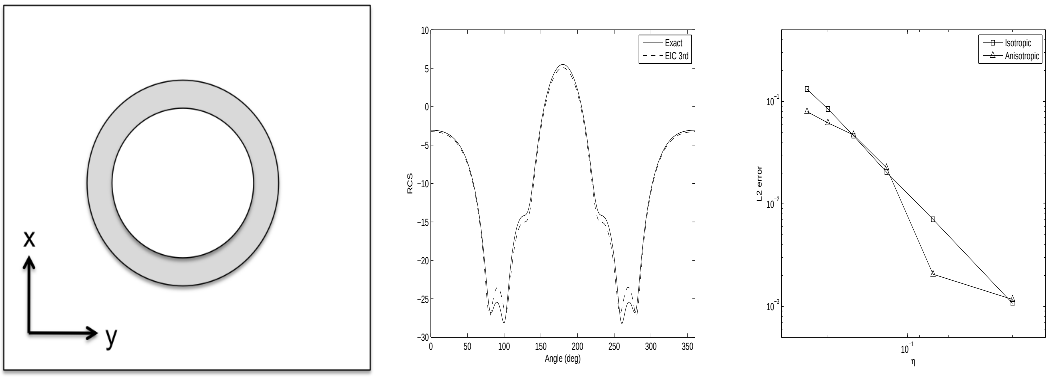

Figure 6.11: Radar cross sections(RCS) of the exact computation(dashed line) and 3rd order EIC (dotted line) for a circular cylinder are compared (left). L_2 errors of field components (right) for isotropic material (square) with $\varepsilon_f = 2.25$ as well as for anisotropic materials (triangle) with $\varepsilon_{xx} = \varepsilon_f n_x^2 + 1,\ \varepsilon_{xy} = \varepsilon_f n_x n_y,\ \varepsilon_{yy} = \varepsilon_f n_y^2 + 1, \varepsilon_f = 2.25$ are shown. For right figure, x axis is reversed, i.e., η is deceasing along x axis

6.4.2.2 Elliptical cylindrical layer

Similarly, consider a elliptical thin layer which is infinitely long along the z axis. Let a and b be the major and minor axis of the ellipsoid of the interface Γ. Inner boundary and outer boundary of the thin layer is generated by projecting each grids points of Γ in the inward and outward normal direction by $\eta/2$, respectively. Note that inner and outer boundaries are no longer ellipsoid. The curvature of Γ

η	0.20	0.16	0.12	0.08	0.04
Isotropic material inside thin layer					
3rd EIC	8.1448e-02	4.6137e-02	1.9662e-02	5.5579e-03	1.1701e-03
	order	2.5470	2.9648	3.1161	2.2480
Anisotropic material inside thin layer					
3rd EIC	4.2831e-02	2.2876e-02	5.6602e-03	1.7850e-03	6.3051e-04
	order	2.8107	4.8547	2.8463	-

Table 6.3: Order of L_2 error of field components for 3rd order EIC are shown. Conditions are the same as given in Fig. 6.12

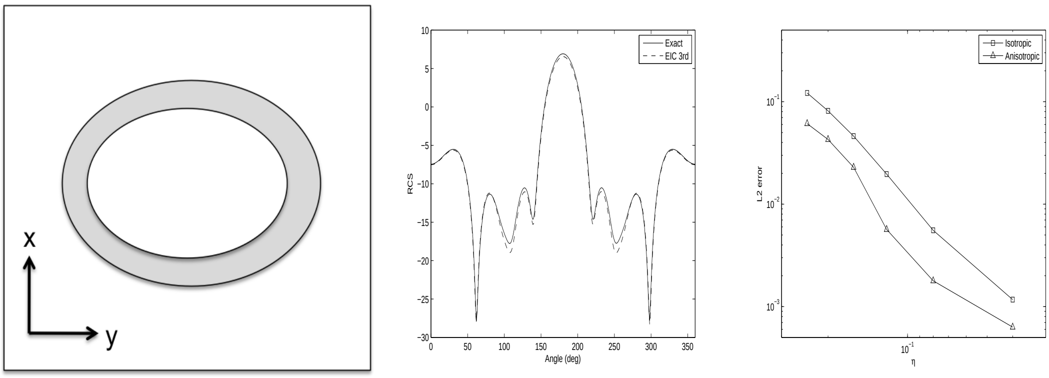

Figure 6.12: Radar Cross sections (RCS) of the exact computation(dashed line) and 3rd order EIC (dotted line) for a elliptical cylinder are compared (left). Also, L_2 errors of field components (right) for isotropic material (square) with $\varepsilon_f = 2.25$ as well as for anisotropic materials (triangle) with $\varepsilon_{xx} = \varepsilon_f n_x^2 + 1$, $\varepsilon_{xy} = \varepsilon_f n_x n_y$, $\varepsilon_{yy} = \varepsilon_f n_y^2 + 1, \varepsilon_f = 2.25$ are shown

is derived as $\mathcal{C} = -\frac{ab}{(a^2\cos^2 t + b^2 \sin^2 t)^{3/2}}\vec{\tau}$, where $t = \tan^{-1}\left(\frac{a}{b}\frac{y}{x}\right)$. The left figure of Fig. 6.12 displays the accuracy of 3rd order EIC. The center/right figures of Fig. 6.12 and Table 6.3 shows the corresponding order of convergence.

6.4.3 Frequency dependence of 3rd order EIC

Similar to effective boundary conditions (EBC) [7], the formulation of EIC also depends on the taylor series of a projection operator $\mathcal{R}_s$, $\mathcal{R}_s(\Pi_{||} + s\mathcal{C}) = \Pi_{||}$, which is used for the expansion of the operator $\mathcal{T}_\Gamma^{\eta\nu}$

$$\mathcal{R}_s = \Pi_{||} + \sum_{i=1}^{\infty}(-\eta\nu\mathcal{C})^i$$

The curvature tensor $\mathcal{C}$, which plays a crucial role for the accuracy of the expansion, is correlated to the frequency of the wave, so the accuracy of EIC depends on the magnitude of the curvature tensor and the frequency of the incident wave. As shown in Fig. 6.16, when the frequency of the incident wave decreases, EIC works more accurately for objects with a smooth boundary such as a circular cylinder and an elliptical cylinder, but a little perturbation is observed for the rectangular cylinder and smoothed rectangular cylinder.

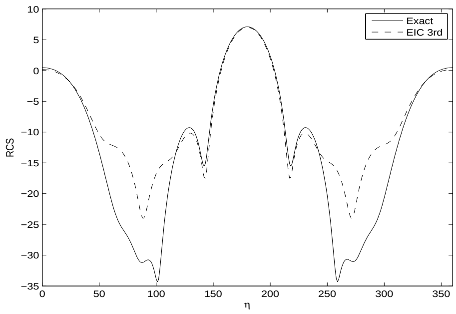

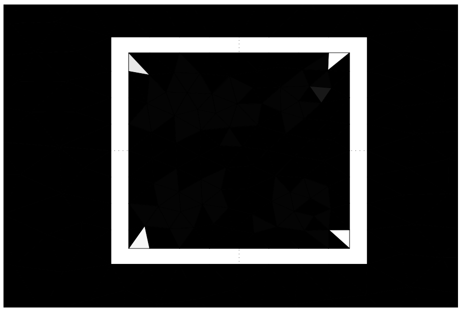

Figure 6.13: Radar cross section (RCS)s of the exact computation(dashed line) and 3rd order EIC (solid line) of rectangular cylinder are compared (left). Distribution of $\|E\|_\infty$ on the cross section of the original rectangular cylinder are shown (right). The brighter the area is, the higher L_∞ error is. For example, the brightest color corresponds to the magnitude of 0.53 and the darkest close to zero in L_∞ error

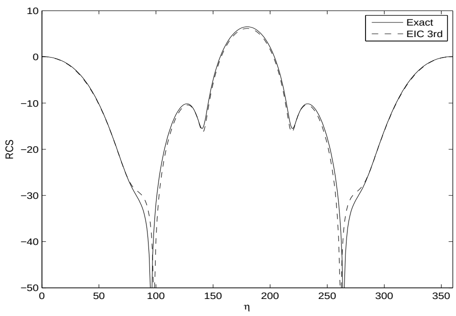

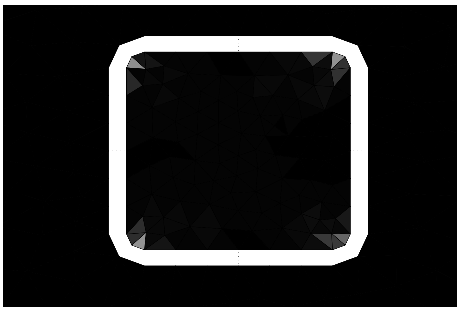

Figure 6.14: Radar cross section(RCS)s of the exact computation(dashed line) and 3rd order EIC (dotted line) of smoothed rectangular cylinder are compared (left). Distribution of $\|E\|_\infty$ on the cross section of rectangular cylinder are shown (right). The brighter an area is, the higher L_∞ error is. The same scaling on color as Fig. 6.13 is used for comparison

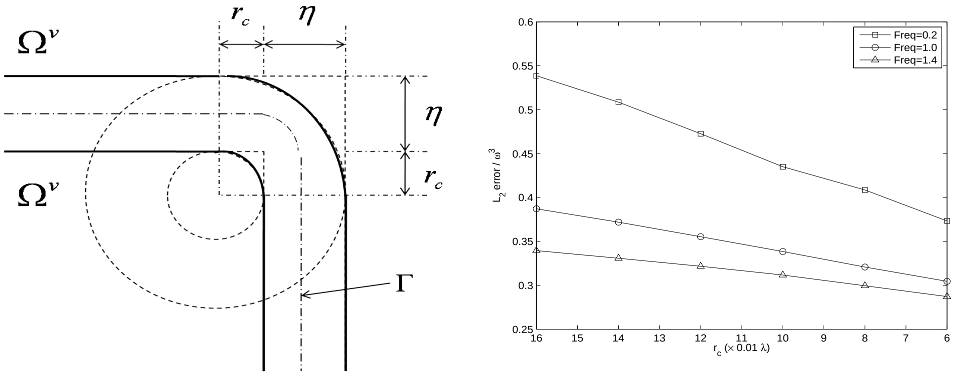

Figure 6.15: Construction of the smoothed rectangular cylinder (left) and RCS errors between the exact computation of rectangular cylinder and 3rd order EIC approximation of smoothed rectangular cylinder (right) for incident waves of different frequencies are shown. As the radius of circle r_c decreases, the RCS of the smoothed rectangular cylinder by thin layer approximation converges to the RCS of original rectangular cylinder by the exact computation, which is independent of frequency

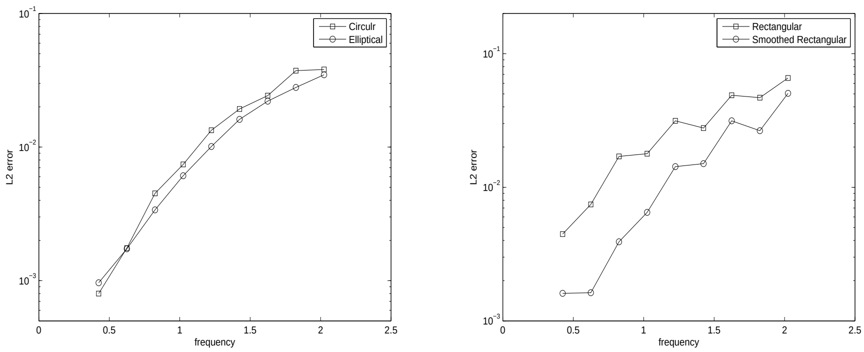

Figure 6.16: L_2 errors versus frequency of incident waves for circular cylinder/elliptical cylinder (left) and rectangular/smoothed rectangular (right). 3rd order EIC works better in lower frequency or smaller magnitude of curvature tensor

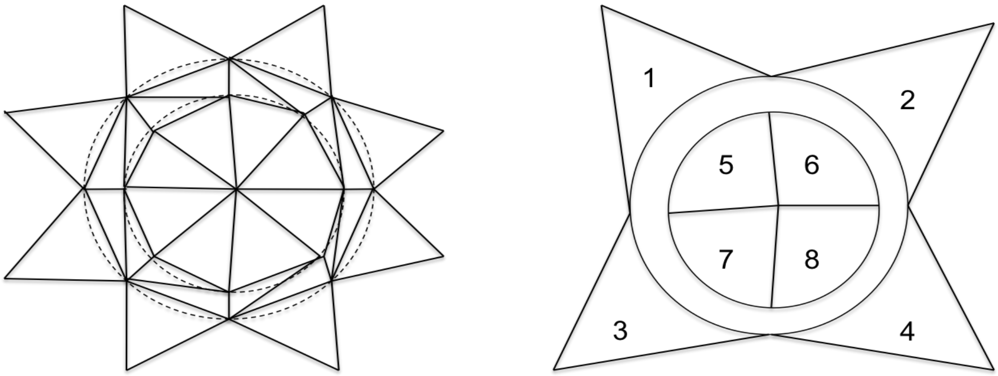

Figure 6.17: Mesh generation of curved objects with thin layer: Original mesh (left) and mesh for thin layer approximation (right)

6.4.4 Extension to objects with non-smooth boundary

When objects have non-smooth boundaries such as vertices of rectangular cylinder, the analysis fails and large errors are observed around those singularity points where the thickness of the thin layer is varied as shown in Fig. 6.13 (brighter ares means the larger errors). This phenomena is inevitable as there are no projection of grid points of outer boundary in inward normal direction around vertices, which leads to large RCS errors especially for 90 and 270 degrees. However, by the process of smoothing out these singular points as shown in Fig. 6.15 (left), those errors can be reduced significantly without loosing stability. Fig. 6.14 shows that the accuracy and convergence of 3rd order EIC on a smoothed rectangular cylinder has improved significantly and is quite similar to the result of objects with smooth boundary. Furthermore, as the radius of the small circle r_c of smoothed rectangle decreases, the thin layer approximation of the smoothed rectangular cylinder converges to the exact computation of original rectangular cylinder independent of the frequency of the incident waves (Fig. 6.15).

6.4.5 Exemplary Application: Combined with curvilinear element

For curved objects with a thin layer, there exist two reasons why we face small elements: The first reason is to resolve the curvature of curved objects and the

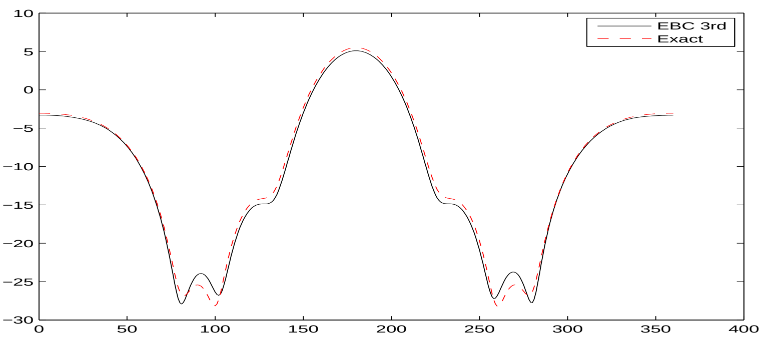

Figure 6.18: Radar cross section for the exact computing and for thin layer approximation. Solid line indicates the RCS of the exact computaion and dashed line indicates that of thin layer approximation

second reason is to avoid small elements inside a thin layer. However, curvilinear elements combined with thin layer approximation can eliminate those small elements without compromising accuracy and stability. A computational experiment with only 4 grid points on the surface of curves (Fig. 6.17) shows that the thin layer approximation combined with curvilinear elements is accurate up to 5.0*e*-3 in RCS (Fig. 6.18), but the total computational time is, at least, 10 times smaller than that of the computation on the original mesh.

6.5 Remarks

In this work, the high-order accurate thin layer approximations have been developed for transmission layers where both reflection and transmission are dealt with accurately. This is an extension of the thin layer approximation for effective boundary conditions in chapter 5 where only reflection is dealt with. The general formulations for 3rd order and 5th order effective curvilinear interface conditions are derived and implemented in the context of a discontinuous Galerkin method (DG), which is well suited for this purpose since the discontinuity of the field elements is inevitable at the interface of thin layers.

In each of one and two dimensional test cases, the expected order of convergence and stability of the scheme are displayed. Using thin magnetic layer approximation in one dimensional periodic photonic crystal layers and computation of two dimensional curved object with thin layer using curvilinear elements, we demonstrated the extraordinary efficiency without compromising the overall accuracy. Since the thin layer approximation is implemented in discontinuous Galerkin method (DG) in an implicit way, the time step Δt of the thin layer approximation is independent of the thickness (η) of the thin layer for 3rd order or proportional to $1/\eta$ for 5th order, which is quite a gain compared to $1/\eta^2$ for the original DG scheme.

Also, similar to the effective boundary condition in chapter 5, we pursued the extension to non-smooth scatterers by replacing an object with geometrical singularities by smooth curves.The result shows that eliminating geometrical singularities of an object confirms the given-order accuracy and stability of thin layer approximation. As the smoothed geometry converges to the original geometry, the field values of the former converge to the those of the latter, which inspires the future works related to this issue.

Future development of a family of thin layer approximation includes the extension of the isotropic/tangentially-oriented anisotropic materials to general anisotropic, frequency dependent dispersive materials. Also, contrary to the current approximation based on asymptotic expansion of distance, specific material-oriented thin layer approximations based on asymptotic expansion of materials constants and distance shall be considered.

Chapter 7

Conclusions

In the first part of this dissertation, the behavior and sensitivity of the frozen mode phenomenon are studied with the discontinuous Galerkin method. Two different kinds of periodic array were studied. One is a gyrotropic photonic crystal consisting of two anisotropic materials with different in-plane misalignments and one magnetic material. The other is a nonmagnetic periodic stack with oblique anisotropic dielectric materials with an air-filled gap between them. The discontinuous Galerkin method is validated and highly unusual phenomena with a very low propagating velocity, highly localized field intensity, and perfectly transmission into crystals comprising of high-index materials are demonstrated. This confirmed the predicted behavior and furthered the understanding of the nature and the limits of the predictions.

Also, the impact of the finiteness of the crystals as well as the sensitivity of the phenomenon to variations in parameters such as material properties and degree of anisotropy was studied to gain an improved understanding of the practicality of utilizing the frozen mode phenomena. By investigating the sensitivity of the frozen mode, the study enabled us to establish the parameters without having any impact on the essential behavior of crystals.

However, determining the appropriate dispersion relation of the frozen mode relied on the analysis of crystal configurations by a trial-and-error technique, which limits the number of parameters and complicates the practicality of modifying the geometric and/or material properties of the crystals. To address this problem in a more systematic way, a PDE constrained nonlinear optimization approach were developed. Here, we used the dispersion relation, given by the transfer matrix method or by solving the Maxwell's eigenproblem, in combination with the algorithm of the Method of Moving Asymptote (MMA).

Using this optimization technique, we demonstrated the ability to recover known solutions and computed several new design by optimizing the geometry and/or the material of the crystals. Especially for the case with the frozen mode requiring an oblique illumination, we found a stationary inflection point in three dimension using parameter sets derived by nonlinear optimization. Also, the frozen mode phenomena was observed by inserting this newly optimized set of parameters in a time-domain wave propagation model with periodic boundary condition in the (x, y) plane when z is the direction of propagation.

The second part of this dissertation discussed the development of thin layer approximation and their use in the context of discontinuous Galerkin method. The superior performance of the thin layer approximation was displayed by one-dimensional scattering problems for various materials. Several kinds of geometries in two-dimensions, such as circular, elliptical and a rectangular cylinder were also considered and their corresponding convergence was displayed. When the geometry has singular points such as vertices of a rectangular cylinder, it was demonstrated that the inaccuracy caused by these geometric singular points can be remedied by smoothing without impacting the global accuracy of the scheme.

Also, we developed a transition condition of thin layers located in arbitrary positions of a domain, to deal with the reflection and transmission of the electromagnetic waves. The work shows how this transition condition can be successfully implemented in any type of time marching scheme while achieving a remarkably low computational cost, but without compromising the stability and maintaining its high order accuracy. The excellent performance for one-dimensional and two-dimensional geometries was demonstrated with various materials such as isotropic, anisotropic and magnetic materials.

The prospective research is inside a butterfly called the Blue Morpho (see Fig. 7.1). Blue Morpho's wings can send its specific color miles away and its color varies with different angles and views, but at the same time, the color is astonishingly uniform. This unique feature of the color is attained by its photonic crystal structure on the dorsal side of its wings. They are composed of simple keratin materials; the wing are sophisticated and have a complicated thin two-dimensional structure. Thus, a highly accurate and efficient computational scheme is required to simulate and analyze a structure such as the Blue Morpho's wing.

Specifically, asymptotic expansion containing certain material constants will be studied thoroughly, which will improve the maximum allowance of the thickness of the thin layer and the accuracy of the transition condition to be determined. Also, maintaining stability and accuracy for various kinds of geometric singularities, transition conditions of a thin layer constituting dispersive materials and initial bounds of moving asymptotes of MMA are open problems.

Figure 7.1: Menelaus Blue Morpho, *Morpho menelaus*. Iridescent tropical butterfly of Central and South America. By courtesy from the Wikimedia Commons

References

[1] K. Dridi A. Ditkowski and J.S. Hesthaven. **Convergence Cartesian Grid Methods for Maxwell's Equations in Complex Geometries**. *Journal of Computational Physics*, **170**:87–101, September 2001. 22

[2] Vijaya Shankar Alireza H. Mohammadian and William F. Hall. **Computation of electromagnetic scattering and radiation using a time-domain finite-volume discretization procedure**. *Computer Physics Communications*, **68**:175–196, 1991. 18

[3] U.M. Ascher and L.R. Petzold. *Computer Methods for Ordinary Differential Equations and Differential-Algebraic Equations.* SIAM, Philadelphia, 1998. 20

[4] Uri M. Ascher, Steven J. Ruuth, and Raymond J. Spiteri. **Implicit-explicit Runge-Kutta methods for time-dependent partial differential equations**. *Applied Numerical Mathematics*, **25**:151–167, 1997. 60

[5] L. Brilouin. *Wave propagation and Group velocity.* Academic press, New York, 1960. 25, 26

[6] Sehun Chun and Jan S. Hesthaven. **Modeling of the frozen mode phenomenon and its Sensitivity using Discontinuous Galerkin methods**. *Communications in Computational Physics*, **2**:611–639, 2007. 42, 52, 57, 61

[7] Sehun Chun and Jan S. Hesthaven. **High-order Accurate Thin Layer Approximations for Time-Domain Electromagnetics and Their Implementation**. *to appear*, 2008. 109

[8] A. Figotin and I. Vitebsky. **Nonreciprocal magnetic photonic crystals**. *Physical Review E*, **63**(0666609), May 2001. 9, 10, 12, 25, 26, 39

[9] A. Figotin and I. Vitebsky. **Electromanetic unidirectionality in magnetic photonic crystals**. *Physical Review B*, **67**(165210), April 2003. 9, 11, 12, 15, 25, 26, 33, 39, 48, 50, 102

[10] A. Figotin and I. Vitebsky. **Oblique frozen modes in periodic layered media**. *Physical Review E*, **68**(036609), September 2003. 9, 25, 26, 39, 56

[11] Alex Figotin and Ilya Vitebskiy. **Gigantic transmission and band-edge resonance in periodic stacks of anisotropic layers**. *Physical review E*, **72**(036619), 2005. 52, 56

[12] A.G. Gurevich and G.A.Melkov. *Magnetization Oscillations and Waves.* CRC Press, New York, 1996. 12

[13] H. Haddar and P. Joly. **Stability of thin layer approximation of electromagnetic waves scattering by linear and nonlinear coatings**. *J. Compt. Appl. Math*, **143**:201–236, 2002. 68, 84, 89

[14] J. S. Hesthaven and T. Warburton. **Nodal High-Order Methods on Unstructured Grids**. *J. Compt. Phys.*, **181**:186–221, 2002. 70, 91

[15] J. S. Hesthaven and T. Warburton. *Nodal Discontinuous Galerkin Methods. Algorithms, Analysis, and Applications.* Springer Verlag, New York, 2007. 70, 71

[16] J.S. Hesthaven. **High-Order Accurate Methods in Time-Domain Computational Electromagnetics: A Review**. *Advances in imaging and electron physics*, **127**, 2003. 19

[17] J.S. Hesthaven and R.M. Kirby. **Filtering in Legendre Spectral Methods**. *Math. Comp*, **submitted**, 2004. 21

[18] J.S. Hesthaven and T. Warburton. **Nodal High-Order Methods on Unstructured Grids**. *Journal of Computational Physics*, **181**:186–221, 2002. 12, 60

[19] J.S. Hesthaven and T. Warburton. **Discontinuous Galerkin Methods for the Time-Domain Maxwell's Equations: An Introduction**. *ACES Newsletter*, **1**(19):10–29, 2004. 12, 18, 60

[20] L. Van Hove. **Van Hove singularities**. *Phys. Rev.*, **1189**(89), 1953. 42, 45

[21] M. Ibanescu, S.G. Johnson, D. Roundy, C. Luo, Y.Fink, and J.D. Joannopoulos. **Anomalous Disperion Relations by Symmetry Breaking in Axially Uniform Waveguides**. *Physical review letters*, **6**(92), 2004. 42

[22] A. Figotin J. Ballato, A. Ballato and I. Vitebsky. **Frozen light in periodic stacks of anisotropic layers**. *Physical Review E*, **1**(71), 2005. xiii, 12, 16, 56, 57

[23] Steven G. Johnson and J. D Joannopoulos. **Block-iterative frequency-domain methods for Maxwell's equations in a planewave basis,**. *Opt. Express,*, **3**(8):173–190, 2001. 57

[24] Christopher A. Kennedy and Mark H. Carpenter. **Additive Runge-Kutta schemes for convection-diffusion-reaction equations**. *Applied Numerical Mathematics*, **44**:139–181, 2003. 60

[25] E.M. Lifshitz L.D. Landau and L.P. Pitaevskii. *Electrodynamics of Continuous Media*. Pergamon, New York, 1984. 12

[26] S.M. Rytov. **Calcul du skin-effet par la methode des perturbations**. *J. Phys. USSR*, **2**:233–242, 1940. 2

[27] A. Stroud. **Remarks on the disposition of points in numerical integration formulas**. *Math. Comput*, **11**:257–261, 1953. 37

[28] K. Svanberg. **The method of moving asymptotes: a new method for structural optimization**. *Int. J. Nuner. Meth. Engng*, **24**:359–373, 1987. 42

[29] K. Svanberg. **Two primal-dual interior-point methods for the MMA subproblems**. *Technical Report TRITA-MAT-1998-OS12, Dept. of Mathematics, KTH, Stockholm*, 1998. 42, 47

[30] K. Svandberg. **A new globally convergent version of MMA**. *Technical Report TRITA-MAT-1999-OS2, Dept. of Mathematics, KTH*, 1999. 42

[31] G. Szego. *Orthogonal Polynomials, 23*. American Mathematical Society, Providence, 1995. 17

[32] A. Taflove and S.C. Hagness. *Computational Electrodynamics*. Artech House, Boston, 2000. 21, 58

[33] A. Taflove and Susan C. Hagness. *Computational Electrodynamics, The finite-difference time-domain method, Third Edition*. Artech House, Boston, 2005. 78, 107

[34] Dongbin Xiu and Jan S. Hesthaven. **High order collocation methods for differential equations with random inputs**. *SIAM J. Sci. Comput*, **3**(27), 2005. 37

[35] A. Yariv and P. Yeh. *Optical Waves in Crystals*. Wiley Interscience, New York, 1984. 12

[36] W.H. Zhang, C. Fleury, P. Duysinx, V.H. Nguyen, and I. Laschet. **A generalized method of moving asymptotes(GMMA) including equality constraints**. *Structural Optimization*, **12**:143–146, 1996. 42

[37] C. Zillober. **A globally convergent version of the method of moving asymptotes**. *Structural Optimization*, **6**:166–174, 1993. 42